ScuDo
Scuola di Dottorato ~ Doctoral School
WHAT YOU ARE, TAKES YOU FAR

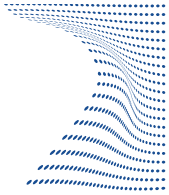

Doctoral Dissertation
Doctoral Program in Energy Engineering (33^{th} cycle)

Modelling Innovative High Temperature Superconductors for Fusion Applications

Andrea Zappatore
* * * * * *

Supervisor
Prof. R. Zanino

Doctoral Examination Committee:
Dr. G. De Marzi, Referee, ENEA, Italy
Dr. J. Li, Referee, Chinese Academy of Sciences, China
Dr. R. Bonifetto, Politecnico di Torino, Italy
Dr. G. M. Polli, ENEA, Italy
Dr. A. Portone, Fusion for Energy, Spain

Politecnico di Torino
2021

I hereby declare that, the contents and organisation of this dissertation constitute my own original work and does not compromise in any way the rights of third parties, including those relating to the security of personal data.

. . . . . .

Andrea Zappatore
Turin, 2021

Summary

Most of the nuclear fusion reactors currently under design include conductors made of High Temperature Superconducting (HTS) materials in their magnet systems, at least as an option to be investigated, and the advantages of this technology are pushing the R&D of conductors suitable for tokamak operation. However, there are still several challenges in the conductor development and, a fortiori, in the magnet design. As for the "classical" Low Temperature Superconducting (LTS) magnets, also for those to be built with HTS numerical tools are used to predict the magnet performance. Nevertheless, the numerical tools for the estimation of the, e.g., thermal-hydraulic (TH) and electric performance currently available are those developed for LTS magnets, such as the 4C code.

In this work, a qualitative assessment of the modelling assumptions of these numerical codes is carried out first, showing the inadequacy of LTS modelling approaches if applied to fast transients, such as the quench, in conductors based on HTS materials. After this qualitative analysis, a quantitative assessment based on detailed models developed on purpose is described, focusing on the HTS Cable-In-Conduit Conductor (CICC) designs proposed by ENEA and by the Karlsruhe Institute of Technology.

The quantitative assessment hints at a new modelling strategy, i.e., the conductor cross-section needs be lumped in several thermal, electric and fluid regions, rather than just two as in the LTS CICC. Therefore, since the 1D discretization *along* the conductor axis is still needed, a tool capable of handling an arbitrary number of 1D thermal, electric and fluid regions along the conductor axis is required. This calls for the development of a new numerical model which is described here and implemented in the new computer code H4C. Furthermore, an electric model able to handle transverse resistance between current carrying elements is required, while the (simpler) electric model adopted for LTS, e.g., that implemented in 4C, assumes no transverse electric resistance.

H4C is then subjected to the standard verification procedure, as well as to a preliminary validation based on recent quench experiments performed in SULTAN, showing that the new code can properly describe the quench propagation in HTS CICC.

An extensive set of applications of H4C is finally presented. The first one is the analysis of quench propagation in CICC, showing that indeed the LTS modelling approach fails in some situations where localized heating is present. The new model can also give a deep insight on how the current redistributes during a quench among the

different tapes of each stack. The code, however, relies on free parameters, such as the heat transfer coefficients between the different cable sub-elements related to the thermal contact resistance, as well as the electric contact resistance between the current-carrying elements. In order to feed the model with the needed parameters for the TH and electric model, dedicated experiments in liquid nitrogen were carried out to directly measure such parameters, such as the electric contact resistance between the tapes and the stacks. Whenever measurements are not available, values from the literature are assumed. The quench analysis of the ENEA CICC also has a feedback on the Divertor Tokamak Test (DTT) Central Solenoid HTS insert design, allowing to suitably tune the quench protection strategy.

H4C was then upgraded to simulate an entire magnet, equipped with HTS layers, such as one of the options of the EU DEMO CS. The simulation of the normal operation (plasma burn) of the EU DEMO CS is carried out, assessing the impact on the magnet performance of different level of localized defects, i.e., local decrease of the critical current density, in the HTS tapes. This analysis shows that damaged stacks lead to a strong decrease of the temperature margin in the neighboring strands. Finally, the simulation of quench propagation in the magnet is presented. The quench is initiated as a consequence of the defects in the stacks, which, beyond a certain threshold, can lead to quench of the conductor even during the normal operation of the magnet. The maximum temperature reached during the quench in the HTS CICCs stays below 160 K, however large temperature differences are observed in the cross-section during the quench initiation, requiring attention to limit secondary stresses.

Acknowledgements

This work has been carried out within the framework of the EUROfusion Consortium and has received funding from the Euratom research and training programme 2014-2018 and 2019–2020 under grant agreement No 633053. The views and opinions expressed herein do not necessarily reflect those of the European Commission.

Contents

List of Tables

List of Figures

Chapter 1

Introduction

1.1 High Temperature Superconductors for nuclear fusion

The opportunity to employ High Temperature Superconductors to build large magnets for fusion applications is under investigation in the EUROfusion consortium [1]. However, EU DEMO magnets will be mostly based on the well-known Low Temperature Superconductors technology, i.e., that employed in ITER. The EUROfusion approach is to adopt HTS only towards cost reduction of the magnet system and/or better performance of the machine. Indeed, the main involvement of HTS in DEMO magnets could be as a sub-portion of the Central Solenoid to decrease its size, thus the size of the entire tokamak [2], or to increase the magnetic flux, thus extending the plasma burn length. On the other hand, more recently, few projects have been proposed relying mostly or entirely on HTS [3]. This has driven the development of conductors for fusion magnets in the recent past. Several conductor layout and/or cabling methods have been proposed, investigated and, just few, tested. The main ideas are the following, see figure 1.1:

- Roebel Assembled Coated Conductor cable (RACC): the Roebel layout is adopted [4] and the feasibility up to few kA has been investigated [5].
- Twisted Stacked Tape Cable (TSTC): the tapes are simply stacked and twisted in order to increase the current capabilities minimizing the AC losses [6].
- Round Soldered and twisted stacked strand: this concept features a stack of soldered tapes enclosed in copper profiles, forming a strand. Several of these strands can be twisted together to reach high current capability, see [7].
- Slotted core: an aluminum core featuring several twisted empty slots is employed in this proposal. The tapes are then stacked and put in the slots [8], without the use of solder, which should improve the bending capabilities of the conductor.

- Cross-Conductor (CroCo): in this case, tapes of different widths are employed in order to optimize, i.e., maximize, the current that can be transported in the same space [9].
- Stacked Tapes Assembled in Rigid Structure (STARS): this conductor features straight, i.e., untwisted, stacked tapes to be employed in helical fusion reactors [10]. It has the advantage of being simple to be assembled and manufactured. The AC losses and the cooling of such bulky conductor still need to be assessed in tokamak operating conditions.
- Quasi Isotropic strand (QI): the idea in this case is to compose a strand stacking the HTS tapes horizontally and vertically [11].
- Conductor On Round Core (CORC): the HTS tapes are wrapped on top of a round metallic core [12]. This concept aims at reaching tens of kA in >10 T magnetic field, which is a typical requirement in fusion magnets.

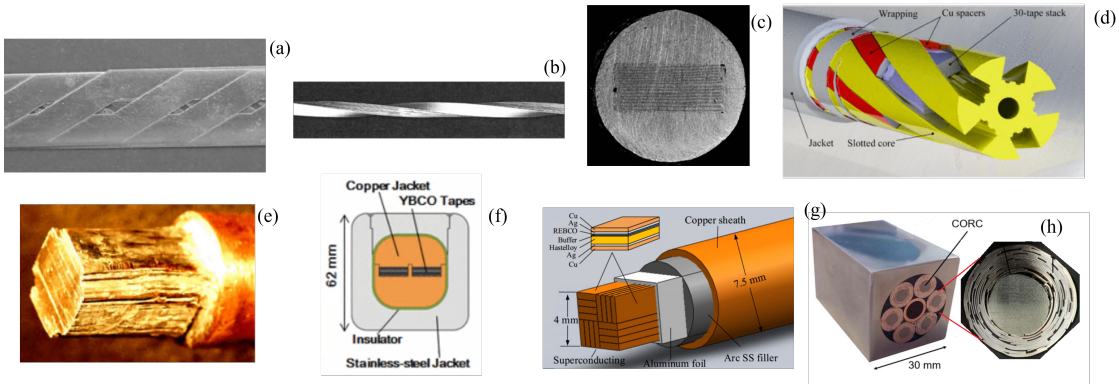

Figure 1.1: Concepts of HTS CICCs and strands: (a) assembled cable based on Roebel idea (RACC), reproduced from [4], (b) Twisted and Stacked Tape Cable (TSTC), reproduced from [6], (c) Round Soldered and Twisted Stacked (RSTS), reproduced from [7], (d) Aluminum Slotted-Core Cable-In-Conduit Conductor, reproduced from [8], (e) Cross-Conductor (CroCo), reproduced from [13], (f) Stacked-Tapes Assembled in Rigid Structure (STARS), reproduced from [10], (g) Quasi Isotropic (QI) strand, [11] and (h) Conductor On Round Core (CORC), reproduced from [12]

.

The most promising candidate seems to be a conductor based on the TSTC idea: few tens of tapes are stacked together and enclosed in a copper round profile, to emulate a round strand, or putting them on a core, obtaining a cable. Few strands are then twisted around a round or flat profile, forming a cable. The cable is then inserted in a conduit, made of steel or aluminum to withstand EM loads and/or to work as confinement for the coolant. Thus, the winning option is oriented towards a Cable-In-Conduit Conductor (CICC).

1.2 Need for modelling tools

The need for modelling tools comes from the obvious inefficiency in terms of time and cost of building prototypes from the small, i.e. short conductor samples, to the large scale, i.e., model coils. Indeed, as already shown for LTS magnets, numerical codes are necessary to support, analyze and optimize the conductor or magnet design [14], taking advantage of their validation on a reduced number of dedicated experiments.

One of the key aspects of the magnet design is the cooling capabilities during the different operation modes. This requires to assess the thermal-hydraulic (TH) performance of the magnet in different conditions, e.g., temperature margin during normal (pulsed) operation or maximum temperature reached during a quench.

However, there are no tools that have been proved to be reliable to assess those quantities in an HTS magnet. Several very detailed (e.g., 3D multiphysics) models have been developed for the analysis of single HTS tapes, short stacks or small coils, e.g., single tape pancake coils with a diameter of few cm. On the other hand, few reliable models for the TH analyses of LTS magnets are currently available. Thus, the strategy to develop a reliable TH model of an HTS magnet could be to upscale the detailed models developed for small-scale applications or to adopt the tools developed for LTS magnets also for the HTS ones.

Concerning the first option, a short review of the available models developed for electro-thermal, electro-magnetic and thermal-hydraulic simulations is provided here. The detailed modelling of HTS tapes, small pancake coils or cable has been focused on electro-thermal aspects, starting from analytical [15], [16], 2D [17], [18], [19] and 3D [20] models, mainly devoted to the analysis of quench in tapes or stacks. From the electro-magnetic modelling point of view, devoted to the modelling of AC losses, Finite Element models have been developed for HTS stacks or small pancake coils [21], [22], [23], [24], [25], [26], [27], [28], [29], [30] or for peculiar cable layouts, such as power cables [31], TSTC [32], [33], [34], CORC [35] and Roebel [36], [37], [38]. The up-scaling of such detailed models is, however, not trivial, even to the conductor scale. Indeed, to keep the problem tractable, either homogenization techniques has already been used in 2D models of small diameter pancake coils [39], or some piece of physics was neglected, such as the fluid-dynamics [34]. Nevertheless, for the simulation of TH transients in a magnet, from the experience gained with LTS magnets, the entire (hydraulic) length of the conductor needs to be taken into account in case of quench (to capture the front propagation) or to account for the thermal coupling between adjacent turns or layers/pancakes during normal and off-normal operation [14] [40]. Therefore, since the up-scaling by a couple of orders of magnitude (from the stack to the magnet scale) of the space scale to be simulated is needed, the use of the currently available detailed models does not appear as a viable option.

On the other hand, there are few well established tools adopted for the TH analysis of LTS magnets, such as VENECIA [41], THEA [42] and 4C [43]. The models developed with such tools are all based on the assumption that the cable cross-section can

be lumped from the thermal point of view in a single region, thus assigning a single temperature value to all the solids of the cross-section as well as assuming that the current is uniformly distributed on the cross-section. This, together with the assumption of lumping the coolant in one or two regions, leads to a 1D approximation of the conductor, in the direction of the coolant itself, lumping in few components the conductor cross-section: jacket, cable and helium.

However, HTS cables are different with respect to LTS ones under several points of views:

- the geometry, because the dimensions of the HTS "strand" is much bigger with respect to the typical dimensions of LTS strands, e.g., ∼0.8 mm in the case of the ITER conductors. This implies also that the number of strands in an HTS cable is much smaller (typically less than 10) with respect to LTS conductors (typically more than 500).

- the materials: the electric and thermal properties of the HTS tapes are strongly anisotropic [44], while those of LTS strands and thus of the entire bundle are isotropic. Therefore, the critical current density of HTS tapes depends also on the relative orientation of the magnetic field with respect to the tape itself, while such dependence is not present in LTS cables.

- the electric and thermal contacts between the cable sub-element: the HTS tapes are typically in poor electrical and thermal contact with each other, since they are either soldered or just put one on top of the other. Moreover, different superconducting regions in HTS cables are far from each other from the thermal and electrical point of view with respect to the LTS strands. Also, the superconducting portion of the tapes is far from the largest portion of the stabilizer, which in several concepts is made of copper around the HTS stack, while in the LTS strands, the superconducting filaments are embedded directly in a copper matrix, leading to a perfect contact between superconductor and stabilizer.

1.3 Aim of the thesis

These observations make the straightforward application of tools and modelling approaches developed for LTS conductor and magnets to HTS coils less obvious.

The first point under investigation in this work is the soundness of the modelling assumptions typically employed when dealing with LTS in the case of TH transients in HTS.

After the qualitative assessment has shown that a new modelling strategy is needed for HTS CICCs, especially when dealing with fast transients, the second aim of this work is to provide a quantitative assessment, through detailed models, of what could be a suitable modelling approach.

Consequently, a new 1D numerical tool to suitably model HTS is developed and qualified, aiming at the simulation of fast transients (e.g., quench) in the most promising conductor designs within EUROfusion.

In order to answer to the needs of thermal-hydraulic analysis of entire magnets, e.g, the EU DEMO CS option, featuring HTS together with LTS, the conductor model is upgraded to simulate fast transients in HTS magnets.

1.4 Structure of the work

This work is organized as follows:

- in chapter 2 the qualitative and quantitative assessment of the issues related to the TH modelling of HTS CICC is carried out. This chapter is based on the work published in [45].
- in chapter 3 the development of the new 1D model and its verification is presented. This chapter is based on part of the work published in [46].
- in chapter 4, the preliminary validation of the conductor model is presented; it is based on the work reported in [47].
- in chapter 5 the results of the quench simulations of the conductor developed by KIT (based on part of the work published in [46]), of the ENEA conductor (based on the work published in [48] and [49]) and of the EU DEMO CS (based on the work presented in [50] are reported. The normal operation of the EU DEMO CS, studying the effect of defects in the HTS stacks is also investigated.

Chapter 2

Critical assessment on HTS TH modelling

In this chapter, the qualitative and quantitative assessment of the time and space scale characteristic of the typical TSTC-type conductor is presented and discussed.

2.1 Qualitative Assessment

First, a qualitative assessment of the time and space scales is carried out. In this way, the quantitative assessment can be focused only on the relevant issues. Here, the focus is on the HTS CroCo, which is one of the representative CICC design for fusion applications. In case of drastically different designs, the qualitative and quantitative assessment need to be carried out again, as it is done in the following for the slotted-core type conductor, see section 5.1.1.2. However, the procedure is general and can be applied also to other CICC design.

The assessment of the time scales characteristic of the conductor is useful to compare them with the time scale of the relevant phenomena/transient. In case the conductor time scales are comparable with that of the phenomenon under study, then they need to be taken into account. Otherwise, if the conductor time scales are very different, i.e., much faster or slower, than the phenomenon of interest, then they can be neglected. The assessment of the conductor space scales gives information on the most suitable strategy of lumping the different regions of the conductor.

The CICC under analysis here is the KIT proposal and it is based on their HTS CroCo concept. The current design is based on six strands, twisted on a pure central copper rod. Each strand is made of a stack of 3 mm and 4 mm wide tapes. The stack is then soldered and inserted in a seamless copper tube, see figure 2.1 and [51]. The tapes are typically 40: 10 with width equal to 3 mm and 30 with width equal to 4 mm. They are arranged with a cross shape, in order to optimize the filling factor of the round cross-section. The cable obtained twisting the strands on the copper rod is then pulled inside

a stainless steel jacket to provide mechanical support and confinement for the coolant. The latter is typically supercritical helium at 6 bar and 4.5 K. The expected total mass flow rate in the conductor is $\sim 2-3$ g/s [1].

The expected peak magnetic field on the conductor is 12 T [1] and this is the value considered in the following of this section, if not otherwise stated.

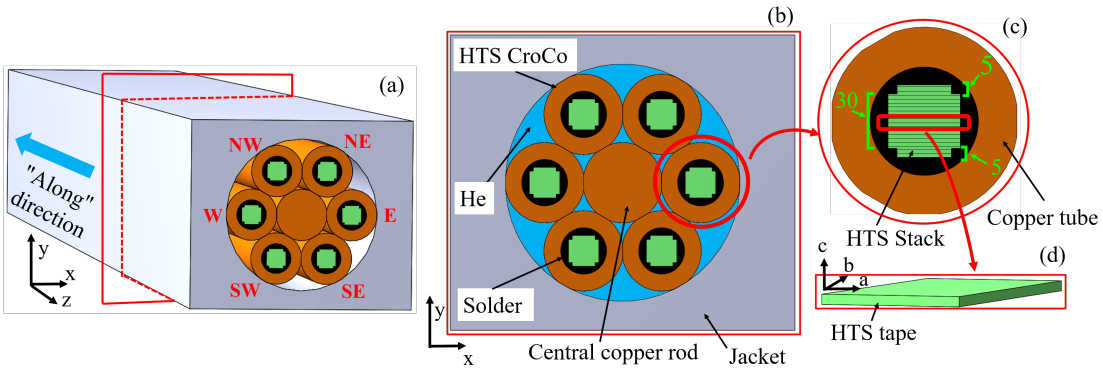

Figure 2.1: (a) 3D view of the HTS CroCo CICC, showing the geographical notation used in the text. (b) Cross-section of the HTS CroCo CICC, showing the jacket, the HTS strands (the solder around the stack is indicated) and the voids in which He is expected to flow. (c) Cross-section of the single HTS CroCo strand, showing the stack and the number of the 4 mm (30) and 3 mm (5+5) wide tapes, the copper tube around the stack. (d) 3D view (not to scale) of the HTS tape, showing also the local reference system used in the text (ab plane and c axis)

Since the time and space scales as well as heat transfer mechanisms are very different depending on the direction under analysis, here two main directions are considered: one along the conductor and the other across it.

As shown in the following subsection, conduction and convection act on a space scale of <10 cm and on a time scale of 1 s and 0.1 s, respectively, on the conductor cross-section. Similarly, conduction and convection are the heat transfer mechanisms along the conductor. However, the hydraulic length of the conductor is of the order of 10^3 m, thus the transit time of the He is of the order of 10^3 s, which is representative of the advective time scale (considering a mass flow rate of 2-3 g/s, an He cross-section of 146 mm^2, thus an He speed of $\sim$ 0.1 m/s and an hydraulic length of 700 m, typical of the hydraulic length foreseen in the DEMO TF coils [1]). On the other hand, the diffusion acts on a much longer time scale, if the direction along the conductor is considered, thus the main heat transfer mechanism along the conductor is the advection, i.e., the heat is preferentially transported by the He. The same conclusion can be reached considering the Peclet number, Pe, defined as the ratio of advection to conduction. Indeed, recalling that $Pe = V D_h/\alpha$, and considering the values typical of the CroCo CICC (V = 0.1 m/s, D_h = 1 mm, $\alpha = 10^{-7}$ m^2/s, a $Pe \gg 1$ is obtained (along the conductor).

This is already a key hint for the TH modelling of such CICCs: the dimensions, materials and operating conditions are such that the relevant heat transfer mechanism along the conductor is the He advection, as it happens already in the LTS CICC, thus the modelling approach of the He already adopted for such technology [42], [43] is valid also for the HTS CICC. This means also that the analysis needs to be focused on the direction across the conductor, i.e., on the conductor cross-section, to check whether time and/or space scales in HTS CICCs are different with respect to those in LTS CICCs.

2.1.1 Conductor time scales

The transients under investigation here are the normal (pulsed) operation of the magnet system, i.e., the plasma burn, and the off-normal operation (propagation of a quench).

The normal operation for a TF conductor is typically characterized, from the thermal-hydraulic point of view, by the nuclear heat load coming from the neutrons produced from the plasma and the AC losses induced by the varying magnetic field of the CS and PF coils. However, the dominant contribution to the total heat deposition in a TF magnet is the nuclear heat load, which is a constant heat deposition lasting for the entire plasma burn phase. In the case of the EU DEMO, the plasma burn is expected to last about 2 hours, thus $10^3 - 10^4$ s [52]. In the case of CS and PF, the characteristic heat loads are mostly due to AC losses, while the nuclear heat load is basically negligible. Indeed, in those coils, the operation is pulsed and, being their magnetic field mostly due to self-field, the heat deposition takes place in times of the order of 1 s for the CS, e.g., during the breakdown phase [1], and 10 s for the PF, e.g. during the coil charge [53]. An analysis of the normal operation of the CS is presented in section 5.2.1. In this chapter, the focus is on the TF conductor and its operation.

The off-normal operation is, on the other hand, characterized by a much shorter time scale with respect to the TF normal operation. Indeed, taking as reference the time during which the temperature grows in a quench, it is of the order of 1 s [54].

Concerning the conductor characteristic time scales, the heat transfer is characterized by two mechanisms, thus two time scales: the diffusion and convection time scales. The two are defined as:

$$\tau_d = \frac{\delta^2}{\alpha} \tag{2.1}$$

$$\tau_c = \frac{\rho \cdot c_p \cdot A_{cross}}{h \cdot P_w} \tag{2.2}$$

where τ_d is the diffusion time scale, δ is the characteristic size of the region considered, α is the heat diffusivity of the material under investigation, τ_c is the characteristic convective time scale, ρ is the density of the material, c_p is the specific heat, A_{cross} is the cross-section of the region considered, h is the heat transfer coefficient and P_w is the wetted perimeter.

HTS tapes and thus HTS stacks are characterized by anisotropic electric and thermal properties. Identifying with *ab* the plane that contains the tape and with *c* the direction normal to the tape (or the stack), then two different values of thermal conductivity, thus of thermal diffusivity, can be identified [44], see table 2.1. All the thermo-physical properties have been computed at 4.5 K.

Starting from the definition of τ_c and τ_d, it can be possible to compute the characteristic time scales of each sub-portion of the conductor. Concerning the diffusion time scales, it has been computed for the stacks, copper profile around the stack and solder. In order to compute also a "global" characteristic time scale of the entire bundle, also the presence of a non-ideal thermal contact between the strands has been considered. It has been assumed a contact thermal resistance at the copper-copper interface equal to $R_t = 5 \cdot 10^{-3}$ m^{2}K/W and a contact length P equal to 2 mm. The equivalent thermal conductivity from one strand to another is equal to $k = 1/R_t \cdot P = 0.4$ W/m/K. The resulting diffusive time scales are summarized in table 2.1.

Table 2.1: Characteristic size, material properties and characteristic time scale of diffusion.

Region	δ (mm)	k (W/m/K)	ρ (kg/m^3)	c_p (J/kg/K)	τ_d (s)
Solder	0.5	21.0	8670	0.94	10^{-4}
HTS,c	4	0.22	8873	0.82	10^{0}
HTS,ab	4	244.0	8873	0.82	10^{-3}
Cu	2	710	8940	0.12	10^{-5}
Bundle	15	1.0	8879	0.32	10^{0}
LTS	40	354	8900	0.18	10^{-3}

The convective time scale has been computed only for the entire bundle, using 2.2, with $\rho = 8900\,\mathrm{kg/m^3}$, $c_p = 0.32\,J/kg/K$, $A_{cross} = 600\,\mathrm{mm^2}$, h = 100 W/m^2/K, P$_w$ = 0.2 m, obtaining $\tau_c = 10^{-1}$ s.

The anisotropy of the HTS tapes and stack leads to a very different diffusion time scales along and across the HTS stack. On the other hand, the diffusion time scales of the copper profiles and of the solder are very small, due to the very large thermal conductivity and characteristic size, respectively. This means that the heat can easily diffuse through the solder and copper, however, its path through the HTS stack (where heat is deposited during quench and by AC losses) takes longer, presumably leading to temperature gradients build up.

This analysis showed that in some regions of an HTS cable, the diffusion time scale is of the same order of typical fast transients, such as the quench propagation. In other words, the implication for the TH modelling is that it is not possible *a priori* to lump in a single region the entire bundle cross-section, describing it with a single value of temperature. On the other hand, the diffusion time scales are all smaller than the normal

operation time scale in a TF magnet, thus the common assumptions to simulate a plasma burn in an HTS TF magnet can be used.

As discussed before, the convective time scale, assuming a heat transfer coefficient h = 100 W/m^2/K [55], is of the order of 10^{-1} s. For comparison, the same time scale computed for an ITER TF conductor is of the order of 10^{-4} s. This large difference is mainly driven by the much smaller wetted perimeter present in HTS cables, which in turn is due to the much larger number of strands in an LTS bundle. Nevertheless, this time scale is lower than both normal and off-normal operation, thus a single value of temperature to describe the He cross-section seems appropriate, provided a good mixing is guaranteed between the different He sub-regions which can be identified in an HTS cable cross-section, see figure 2.1.

2.1.2 Conductor space scales

The characteristic space scales of thermal gradients can be quantified looking at the Biot number, *Bi*, which is defined as the ratio of the conductive and convective resistance $Bi = h \cdot \delta/k$. The physical meaning of this dimensionless parameter is that, in case it is smaller < 0.1, then the thermal gradients in the solid (driven by the conductive thermal resistance) are much smaller than those between the solid and the fluid (driven by the convective thermal resistance). The implication on the modelling is that, in case Bi < 0.1, then the temperature profile in the solid is almost flat and a single value of temperature is a good approximation of the entire profile, i.e., the solid cross-section can be lumped in a single 0D region.

Concerning the HTS CroCo case, looking at it as a multi-layer cylinder constituted by the HTS stack, the solder and the copper, it can be possible to compute an overall conductive thermal resistance to then quantify the *Bi* for the CroCo. The thermal resistance of a cylindrical layer can be computed as $R_t = \pi D_{out} \cdot ln(D_{out}/D_{in})/(2\pi k)$.

Considering the two different values of thermal conductivity of the HTS stack (in the two directions, along and across the stack), two values of *Bi* are obtained, see table 2.2. In the direction perpendicular to the stack, *Bi*>1, then it is not straightforward to decide a reliable strategy to lump the stack cross-section. For this reason, further more detailed and quantitative analyses have been carried out: they are presented in the following section.

Table 2.2: Heat transfer coefficients, characteristic size, thermal conductivity and Biot number in the HTS CroCo stack and in the bundle of the ITER TF conductor.

Region	h (W/m^2/K)	L (mm)	k (W/m/K)	Bi
Stack (ab plane)	100	4	244	0.001
Stack (c-axis)	100	4	0.22	2
LTS bundle	100	40	350	0.01

2.2 Quantitative assessment

In the previous section, it was shown that the conductive time scales are comparable with those of some transients of interest. Equivalently, the analysis on the space scales showed that a finer cross-section discretization is needed. However, the qualitative assessment did not allow to answer to the question of *what* could be a reliable simplification, i.e., lumping, of the conductor cross-section in a 1D model along the conductor axis. Therefore, a more detailed model is needed in order to *quantify* the temperature gradients arising on the conductor cross section, computing the evolution of the temperature distribution during the transient.

In order to build such a model, some preliminary considerations are needed. Concerning the current, during the propagation of the quench it will redistribute among the different (and available) current carrying elements according to the relative weight of the respective resistance, therefore an electric model able to account for such redistribution is needed. This is because, once the current starts to be shared among resistive elements, it produces heat due to Joule effect, affecting (and driving) the temperature distribution. In turn, the temperature distribution and evolution needs to be captured as it is the aim of this investigation and because it is strictly coupled to the current redistribution.

The interest here is focused on the first few seconds of the quench initiation and propagation, when the most severe temperature gradients are present. On these short time scales, the impact of the convection with the He and the conduction within the solids in the *longitudinal* direction is weak, therefore the electro-thermal model can be developed for the conductor cross-section only.

Further simplifying assumptions are described hereafter:

1. the presence of the He is taken into account as boundary condition of the thermal model, thus assuming a constant He temperature and heat transfer coefficient. This is justified by the fact that the focus of the analysis is on the first few seconds of the transient, when the heat propagates mainly through diffusion in the conductor cross-section, before being dissipated in the He stream.

2. the relevant conductor sub-regions modelled in the thermal model are the strands. They are, in turn, modelled as two regions in contact with each other, i.e., the HTS stack and the surrounding copper tube. The HTS tapes are not modelled in detail: they are homogenized in a single region. The impact of this approximation has been further investigated through an additional detailed model of the stack only, see paragraph 2.2.2.

3. the jacket is neglected, since it is not expected to play a fundamental role as current carrying region and, as far as the heat diffusion is concerned, it is in weak contact with the strands, thus it will not strongly impact on the temperature field evolution within the strands.

4. the current-carrying elements are assumed to be the HTS stacks and the surrounding copper as well as the central copper rod. The current is assumed to be uniformly distributed in each current-carrying element cross-section. This, for the copper, is justified by the very high electrical conductivity, which allows a very fast redistribution of the current in the copper. The impact of this assumption on the HTS stacks is less trivial to be quantified, due to their layered structure, thus it is investigated in the stack detailed model described in section 2.2.2.

5. concerning the magnetic field, this conductor will operate in high (background) field environment, i.e., > 10 T, therefore the contribution of the self-field is neglected.

2.2.1 Electro-thermal model of the conductor cross-section

The assumptions mentioned above lead to a 2D thermal model coupled with a 0D electric model; the two models are described here.

Thermal model The thermal model solves the (transient) heat conduction equation in the central copper rod and in all the superconducting strand. These strands include as separate regions the HTS stack, the surrounding copper tube and the solder layer around the stack. As mentioned before, the stack is not modelled taking into account each tape constituting the stack. However, it is important to account for the presence of that layered structure. Indeed, the thermal conductivity of the stack region, in the thermal model, is temperature dependent and anisotropic, based on the experimental data of [44]. All the other thermo-physical properties of the different materials are also temperature dependent and they have been taken from [56]. Concerning the other properties of the stack, i.e., density and specific heat, they have been obtained with a volume-weighted average of the properties of the pure material constituting each layer of each tape.

Another fundamental capability of this thermal model is to compare the thermal field evolution as a function of the thermal resistance among the different regions of the conductor. For this reason, the possibility to account for a contact thermal resistance between the strands has been considered in the model, see figure 2.3.

This thermal model, together with the electric model described below, is implemented in STAR-CCM+ [57], which solves the 2D heat equation using the finite volume method.

Electric model The 0D electric model has been implemented according to the circuit reported in figure 2.2. The aim is to model the current redistribution due to the (strong) variation of the resistivity of each region during the quench, i.e., in the superconducting

stack due to the transition to the normal state and in the copper regions due to large temperature changes. The simplifications that led to this model are:

- no transverse resistance at the interface between two electric elements, thus the current can redistribute without voltage differences from one element to another.
- no inductive effects are considered, thus the resulting model is steady state and the variation of the current does not induce current changes in other regions. At the same time, this implies that the variation of the current is immediate when the applied voltage changes.

The resistance of the superconducting regions is modelled with a power law and that of the copper regions with the Ohm's law, see also [27]. The resulting system of non-linear algebraic equations of the model is the following:

$$V = R_{Cu,i} I_{Cu,i} \tag{2.3a}$$

$$V = V_C \left(\frac{I_{HTS,i}}{I_{C,i}(B,T)} \right)^n \tag{2.3b}$$

$$I_{tot} = \sum_{i=1}^{N_{Cu}} I_{Cu,i} + \sum_{i=1}^{N_{SC}} I_{SC,i} \tag{2.3c}$$

where V is the voltage at the ends of the circuit, that is common to all the regions, $R_{Cu,i}$ is the resistance of the i-th copper tube or central copper rod, $I_{Cu,i}$ is the current in the i-th copper tube or central copper rod, V_C is the critical voltage, i.e., the critical electric field over 1 m, assumed equal to 10^{-4} V, $I_{HTS,i}$ is the current transported in the i-th stack, $I_{C,i}(B,T)$ is the critical current evaluated at magnetic field B and temperature T, n is the conductor n-value, here assumed equal to 15 [58], which rules the steepness of the transition from superconducting to normal state (and, mathematically, the "severity" of the non-linearity of the problem), I_{tot} is the total current imposed constant and equal to 50 kA, N_{Cu} and N_{SC} are the number of copper sub-regions and HTS stacks, respectively.

The system of equations 2.3 is solved through a root-finding algorithm (implemented in MATLAB®) which computes V and then the power generate by Joule effect based on the current flowing in the i-th (copper or superconducting) region and its resistance. This value of power density, that is supposed to be uniform in each electric region, is then sent to the thermal model which performs a time step with this input. Once the time step of the thermal model is finished, the *average* temperature of the copper or superconducting region is passed to the electric model, which uses this value to computed the updated resistance of each region.

The superconductor scaling law as well as its parameters used for the computation of the critical current are taken from [58].

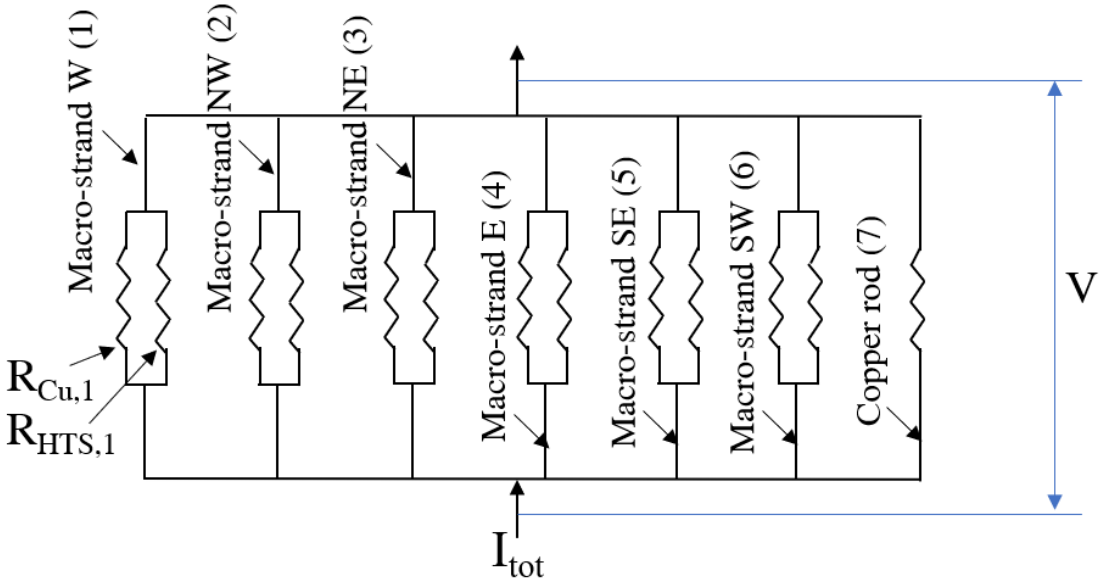

Figure 2.2: Scheme of the 0D electric circuit model adopted in the model. The geographical notation and the numbering is also shown. For clarity, the electrical resistance of the copper profile and HTS stack of strand #1 are shown.

Simulation setup and driver The heat pulse inducing the quench is characterized by a power density of $1 \cdot 10^{-3}$ W/m^3, deposited uniformly in the HTS stack of the west (W) strand. The pulse duration is 0.1 s (starting at t = 0.5 s) as agreed in [59] for LTS quench analysis. The amplitude of the heat pulse was chosen as the smallest pulse able to induce a quench.

Note, however, that this analysis does not aim to perform a stability analysis, for which the dynamics of the He flow is important. Here, in fact, the He is taken into account as boundary conditions, i.e., with fixed temperature, because the aim is to investigate the thermal response of the conductor cross-section. Nevertheless, the heat transfer to the He acts on similar time scales as the heat diffusion, thus the increase of temperature of the He should be taken into account in more accurate models. For the time being, the temperature of the He is set at 4.5 K and the heat transfer coefficient, deduced from experimental correlations proposed in [60], is taken (constant) equal to 100 W/m^2/K.

The symmetry of the geometry, the thermal driver and the boundary conditions are exploited simulating half of the conductor cross-section, imposing a symmetry boundary condition on that side of the domain, see figure 2.3.

Different values of the inter-strand thermal contact resistance have been investigated. Two representative cases are reported here:

- Case A, assuming inter-strand contact resistance equal to 0, thus the strands are in perfect thermal contact.

- Case B, the resistance between the strand is assumed equal to $5 \cdot 10^{-3}$ m^2K/W, which is a typical value of contact resistance at copper-copper interface [60].

The contact length is assumed equal to 2 mm, constant for all strands and uniform along the conductor length. Also this value is strongly dependent on the manufacturing process and it can hardly be the same value for the entire conductor length. However, only experimental investigations can try to quantify this parameter, which of course can influence also the easiness of the current distribution.

Concerning the magnetic field, the presence of the strong (background) magnetic field gradient is taken into account assuming a linear distribution of the field over the conductor cross-section from 12 T to 11 T. A uniform value of the magnetic field is assumed in each sub-region, e.g., 12 T on the W strand and 11.5 T in the central copper rod and 11 T in the E strand. Note that the magnetic field affects the critical current of the superconductor, thus its resistance, but also the thermal conductivity and electrical resistivity of the copper.

The simulation is stopped when the maximum temperature in the computational domain reaches 150 K, because above that threshold it is reasonable to assume that the quench protection could intervene dumping the current.

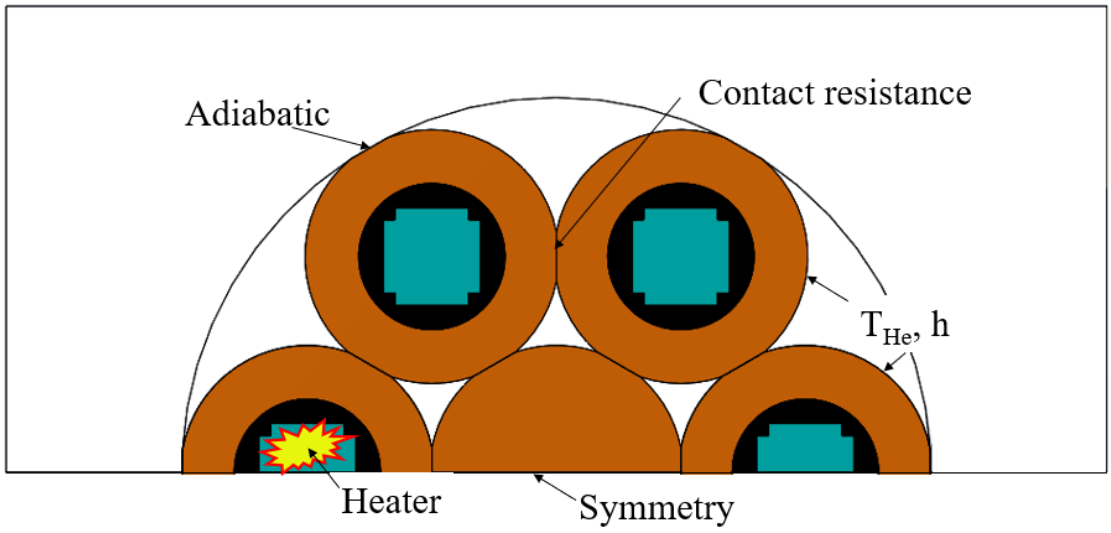

Figure 2.3: 2D thermal model adopted in the electro-thermal model described in the text. The computational domain, the thermal driver and the boundary conditions are shown.

Results Starting from case A, where the contact resistance is zero, the strands are in perfect thermal contact with each other. This ensures a fast diffusion of the heat within the cross-section. Indeed, the temperature of strand W differs clearly from that of the others just for the duration of the heat pulse, which is localized only in the W strand.

As soon as the heat pulse is switched off, the temperature of the W strand becomes quickly equal to those of the others, which have started to be heated up already by diffusion during the heat pulse, see figure 2.4(a). Concerning the current in the stacks, it reacts according to the temperature field first. Indeed, the current in the HTS stack of the W strand, where heat is deposited and the temperature overcomes T_C, drops from more than 8 kA to 2 kA. The current in excess in the W stack is shared among all the others - still superconducting - strands. The current in NW, NE and E, in fact, increases to up to 9 kA for few ms, see figure 2.4(b). When the heat pulse is switched off and, consequently, the temperature decreases in strand W, also the current there increases again and it is equally distributed among the different strands, since they have again the same temperature. However, the temperature of all the strands is increasing thus the current starts to be shared with the copper tubes and the central copper rod, see figure 2.4(c). Of course, being the copper regions resistive, heat is generated due to Joule effect, which becomes the driver for the increase of the temperature. Note that the resistance of the central copper rod is lower than the copper tubes due to the larger cross section, therefore more current flows there. In ∼6 s the temperature has reached 150 K and the current is flowing entirely outside the stacks.

In case B, whose only difference with respect to case A is the presence of a thermal contact resistance at all the interfaces among the strands, the evolution of the temperature and of the current changes. First, the temperature of strand W reaches slightly larger values than in case A because one of the heat sinks, i.e., the adjacent colder strands, is less effective. More importantly, the cooldown of strand W is much slower than in the perfect thermal contact case, see figure 2.4(d). This implies the presence of larger temperature differences for several seconds between the different sub-elements. Concerning the current evolution in the HTS stacks, the drop of the current in stack W is even more evident than in case A, due to the higher temperature reached during the external heating phase. Being less effective the cooldown of strand W after the end of the heat pulse, also the current that flowed away from stack W just partially comes back into the stack of the strand W, see figure 2.4(e). Also, since the temperature of strand W is higher than the others, the current that starts flowing in the respective copper tubes is not uniformly distributed, see figure 2.4(f). Indeed, a higher temperature causes a larger resistivity of the copper, thus less current flows in the copper tube of the strand W. The central copper rod, as explained above, carries more current. However, since also the thermal contact of the copper rod with the other strands is worse than in case A and more heat is generated there with respect to that produced in the copper tubes, a higher temperature can be observed in the central copper rod for these reasons, see again figure 2.4(d). Therefore, at least two electric regions are needed to follow the current evolution in each strand, i.e., HTS stack + copper tube around.

The temperature map shown in figure 2.5 can be used, together with the previous discussion, to hint possible lumping strategies for the conductor cross-section. First, the temperature gradients in case A are less evident, i.e., of the order of few K, than those of case B. In the latter case, the temperature differences are as high as $\sim 20\ K$ due

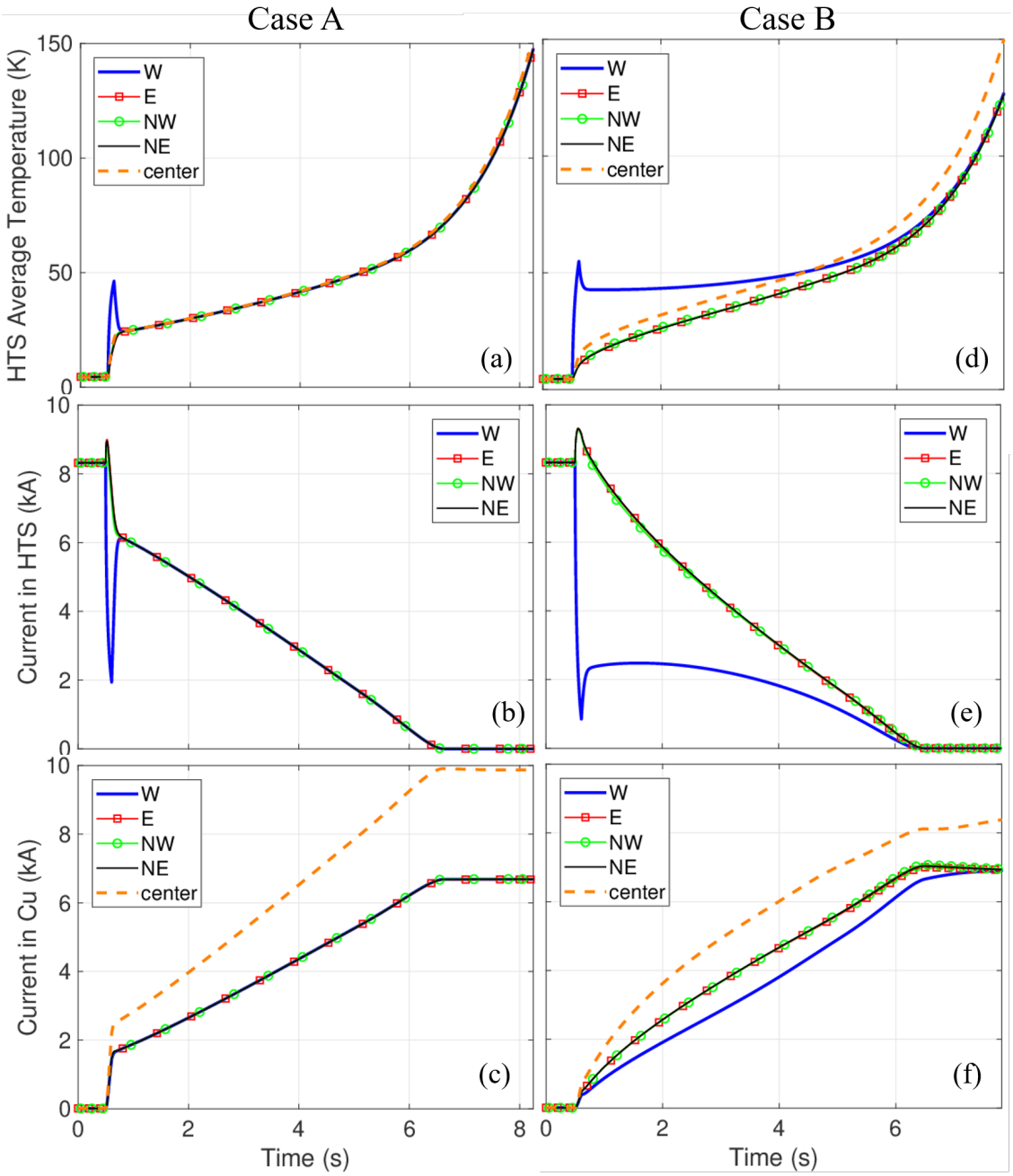

Figure 2.4: Evolution of the HTS stack average temperature in case A (a) and case B (d). Evolution of the current in the HTS stacks in case A (b) and case B (e). Evolution of the current in the copper tubes and central copper rod in case A (c) and case B (f).

to the presence of a realistic thermal contact between the strands.

Thus, in case A, being the temperature field uniform in the cross-section, see figure

2.5(a), a single value of the temperature can be considered representative of the entire cross-section. Nevertheless, during the heat deposition, the temperature of strand W is tens of K larger than that of the other strands. Consequently, also the current is clearly different with respect to that carried by the other strands. In addition, the central copper rod, keeping the same temperature of all the other strands, except for W, carries more current than the others. This means that, in order to capture these non-uniformities during the (short) heating transient, a single thermal and electric region should be assigned to strand W, to the central copper rod and to other strands; considering also an additional one for the jacket, 4 regions are needed in total.

Concerning case B, the temperature difference of tens of K mentioned before lasts not only for the duration of the heat pulse, but for most of the transient, see figure 2.5(b); thus in this case, a fortiori, a dedicated region for strand W is needed. Also in this case, the current evolves in a very different way in strand W, in the central copper rod and in all the other strands. Therefore, also from the electric point of view, a dedicated region is required.

Note that the increasing level of detail is typically expensive also in terms of additional constitutive relations that should be known. For example, if a segregated region is dedicated to the central copper rod, then the heat transfer coefficient of the He in the sub-channels facing the central copper rod should be known. Instead, in case of lumping the solid in just one region, then a single "effective" heat transfer coefficient could have been used, perhaps calibrated experimentally.

Concerning the impact of the magnetic field gradient, which is taken into account in the model, on the temperature evolution, it is negligible. Although it is known that for large magnetic field gradients (in large CICC cross-section) it can play an important role in the quench initiation, inducing non-uniformities in the cross-section, even for the quench in LTS, see [61], here the effect is small, as expected also from the weak variation of the critical current densities of YBCO with respect to NbTi or Nb_3Sn. In conclusion, disregarding the thermal contact resistance, in order to properly capture the evolution of the temperature and of the current in the conductor cross-section, more than just one thermal and electric region is required for the simulation of this kind of transient in HTS CICCs.

Going deeper in the space scale, the next point to be addressed is the level of detail needed to model the single strand. Looking at the temperature difference in the strands of case B, see again figure 2.5(b), the differences are <0.5 K in the copper tubes and ∼2 K in the HTS stack. This means that, being these temperature differences much smaller than those between the strands, the HTS stack and the copper tubes around (plus the solder) could be lumped in a single thermal and electric region each. However, in order to understand the impact of the modelling assumptions done in this analysis, e.g., homogeneous HTS stack, with no transverse electrical resistance in the stack itself, a more detailed model of the stack is required.

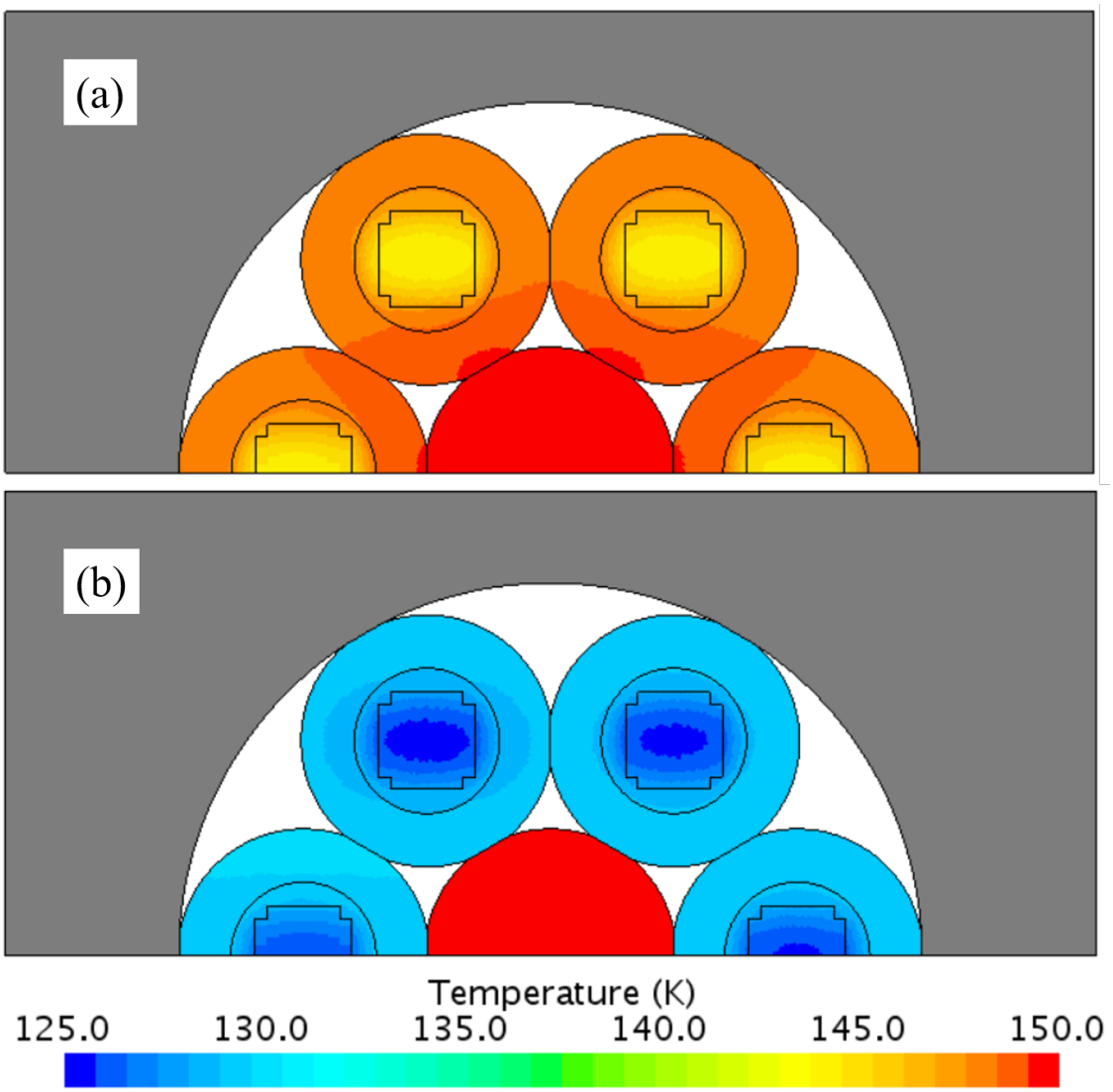

Figure 2.5: Temperature distribution computed with the 2D thermal + 0D electric model at 4.7 s after the beginning of the heat pulse in case A (a) and case B (b).

2.2.2 Electro-thermal model of the strand

The previous model and the results obtained were useful to understand a suitable strategy to lump the cross-section of the CICC, i.e., it is advised to consider different electrical and thermal region for the different strands in order to cope with non-uniformities in the cross-section. Focusing on a single strand, i.e., copper tube + HTS stack (+ solder), temperature gradients can be present also within the HTS stack, mainly induced by the anisotropic thermal conductivity. Concerning the current redistribution, two separate regions should be used to model the stack and the surrounding copper tube. However,

the stack was modelled as a homogeneous region, even though the preliminary assessment of the heat transfer time scales has shown that it cannot be, in principle, lumped into a single region during fast transients. Thus, to investigate deeper the evolution of the temperature and current distribution within the strand during a quench, a detailed electro-thermal model of the single strand has been implemented in COMSOL® Multiphysics [62]. The model is based on the following assumptions:

- the strand is, in principle, a 3D object. However, considering that (a) the thermal and electric conductivity of the copper is very high and isotropic and (b) the same properties are very high in the *ab* plane of the tape, it is possible to go from a 3D to a 2D model. In fact, assuming that the current and the heat can diffuse very quickly in the *ab* plane of the tapes, that direction can be lumped, thus simulating only the cross-section of the stack (in the longitudinal direction), see figure 2.7(a). Thus, the resulting computational domain is a 2D cartesian multi-layered structure with a 4 mm width in the third direction.

- also the copper needs to be converted into a 2D region. Thus, the vertical dimension of the copper is chosen in order to preserve its cross-section, going from a (sort of) cylindrical geometry to a 2D cartesian one.

- the tapes are modelled in detail, i.e., each layer of each tape is modelled. To reach this level of detail, a structured mesh is used, as proposed in [17], [18]. This is needed in order to take into account the anisotropy of the tape properties, while keeping the computational cost acceptable. The buffer layer, see figure 2.6, although very thin (0.1 μm), is highly resistive and has a strong impact in the redistribution of the current across it [63], [17]. Thus it was modelled as a purely resistive 1D layer.

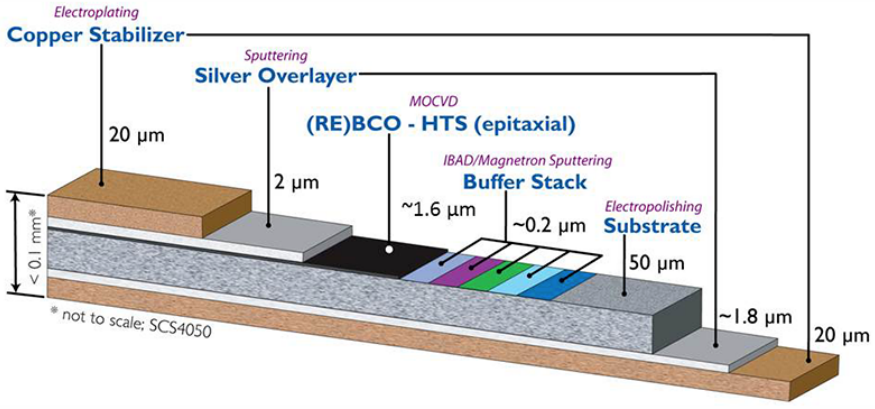

Figure 2.6: 3D view of the typical HTS tape architecture, reproduced from [64]

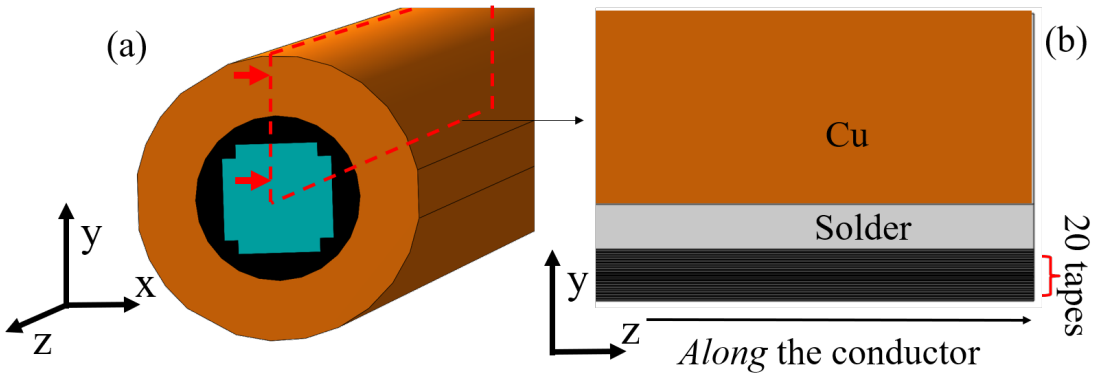

Figure 2.7: 3D view of the HTS CroCo strand (a) and 2D equivalent computational domain used for the 2D electro-thermal analysis (b).

Electro-thermal model The model is a 2D electro-thermal model. The electric model solves the 2D electro-dynamic equation adapted for the presence of superconducting materials, see also [18], [19]. No transverse electrical resistance is considered among the different materials and layers. Nonetheless, the anisotropy of the stack of tapes is taken into account since they are simulated in detail, down to each layer of each tape, see again figure 2.6. The electric properties of the materials are all temperature dependent: for this reason, the electric model is coupled to the temperature field. The superconductor scaling law is taken from [58].

The thermal model solves the 2D heat conduction equation. The thermo-physical properties of all the materials are temperature dependent and taken from [56]. Also in this case, the thermal contact resistance between adjacent materials is assumed to be negligible. However, since each layer of each tape in the stack is simulated, the anisotropy due to the multi-layer structure of each tape is directly resolved and it is not approximated.

Simulation setup and driver The setup of the 2D electro-thermal simulation is described in this section and represented in figure 2.8. The boundary conditions are the following:

- bottom boundary: symmetry condition
- left boundary: voltage set to V = 0 V; adiabatic for the thermal model
- right boundary: current set to I = 8 kA; adiabatic for the thermal model
- top boundary: Robin-type condition, accounting for the presence of the He at a constant temperature of 4.5 K and constant heat transfer coefficient set equal to 100 $W/m^2/K$ [55]; insulated for the electric model.

The driver of the transient is an external heat pulse, which is modeled as a localized power deposition equal to $1 \cdot 10^{10}$ W/m^3, which is deposited on the two central tapes of the stack (in order to investigate the effects of the stack anisotropy), over a length of 2 mm and a duration of 100 ms.

The temperature evolution is monitored in four points, all put at z = 5 mm and at increasing height, i.e. y_1 =0.2 mm, y_2 =1.7 mm, y_3 =2.5 mm, y_4 =7.5 mm, where y_1 is in the second tape, y_2 in the last but one tape, y_3 in the solder, y_4 in the copper tube, see again figure 2.8.

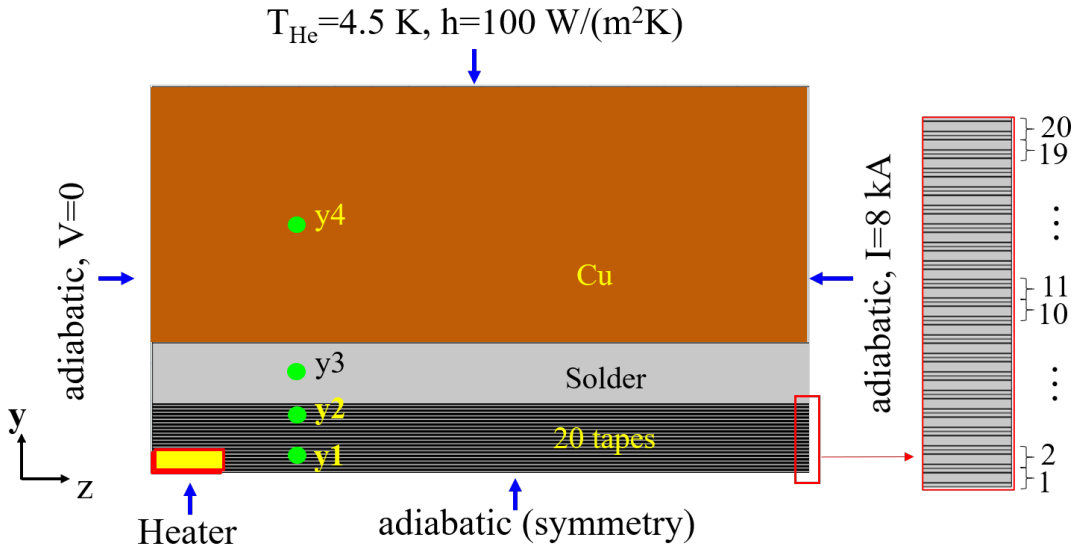

Figure 2.8: Boundary conditions and driver of the transient (yellow rectangle indicating the position of the external heating) simulated with the 2D electro-thermal model. The green dots (y1-y4) are the positions where the temperature is monitored, see below. A zoom highlighting the different layers of the tapes accounted for in the model and their numbering is shown.

Results The results to look at are the temperature evolution and distribution as well as the current evolution in the different regions of the stack and of the strand.

The heat pulse induces a temperature increase in the stack, even outside the region where the heat is directly deposited, due to (fast) heat diffusion, during the 100 ms when the external heating is switched on, see figure 2.9(a). In the heated region (and close to that point) the temperature overcomes the current sharing temperature for few tenths of seconds; as a consequence the current tries to migrate from the hotter tapes to the colder ones, see the first instants in figure 2.9(b). After the heater is switched off, the heat can diffuse along and across the tape, eventually to the heat sink on the outer side of the copper region. This explains the temperature decrease in the externally heated

region, which leads also to a partial and temporary recover (and increase) of the current, which flows back into the previously heated region, see the interval 0.1 to 0.5 s in figures 2.9(a) and 2.9(b). Nevertheless, part of the current has started flowing into the copper and heat has started to be generated there due to Joule effect. The heat generation overcomes the heat sink and the stack loses slowly its superconductivity, leading to a slow temperature increase, see the rest of figure 2.9(a) and, consequently, to a decrease of the transported current in the tapes, see the rest of figure 2.9(b).

This behavior is confirmed also by the evolution of the current in a single tape, see figure 2.9(c). The 10^{th} tape was considered in order to avoid a strong influence of the heating in the first tapes as well as to avoid the influence of the solder and copper regions in the last tapes of the stack. It can be seen that during the heating, the YBCO layer loses most of its current, which is shared with the adjacent copper layer and partly also with the silver layer. As expected, just fractions of amperes flow in the substrate, which has a high electric resistivity with respect to copper and silver. Even though silver has a very high electric conductivity, its cross-section is very small, so the overall electric resistance is larger than the copper layer. After the end of the heat pulse, the tape cools by conduction to other tapes and to the colder region along the stack itself. This leads to a partial recovery of the YBCO layer, which takes back most of the current. Nevertheless, due to the continuous heating of the strand due to the presence of the current in the copper tube around the stack as well as in the copper layers of each tape, the temperature continues to grow and slowly the current of the YBCO drops to zero and it is shared with the stabilizer layers as well as with the outer copper tube (not shown), acting as current bypass during the quench. Indeed, as it is visible from figure 2.9(c), the sum of the current flowing in the non superconducting layers is lower than the starting value of the current in the YBCO. Note however that the current transported by the resistive layers of the tapes is not negligible.

As a further analysis of the current evolution in the tape, in principle, the bottom copper layer should transport less current that the top one (and the same is true for the silver layers). This expectation is motivated by the presence of the highly resistive buffer layers as well as to the presence of the substrate. However, they appear to be equal in the tape considered in figure 2.9(c). This is because the bottom copper and silver layers of tape *i* are in (perfect) electrical contact with the top copper and silver layers of the tape *i-1*. Therefore, the asymmetry introduced by the presence of the buffer layers and by the substrate is compensated by the same asymmetry in the neighboring tape.

Concerning the temperature distribution within the strand, during the heat deposition, the strong anisotropy in the thermal conductivity of the stack (caused by the piling of all the tapes, each made by several layers of different materials) causes a large temperature difference (larger than 30 K). Furthermore, the thermal model does not take into account all the inter-layer and inter-tape thermal contact resistances (mainly because there are strong uncertainties on such quantities). Thus, the anisotropy (in the direction normal to the tapes) is, in reality, even more pronounced, which means

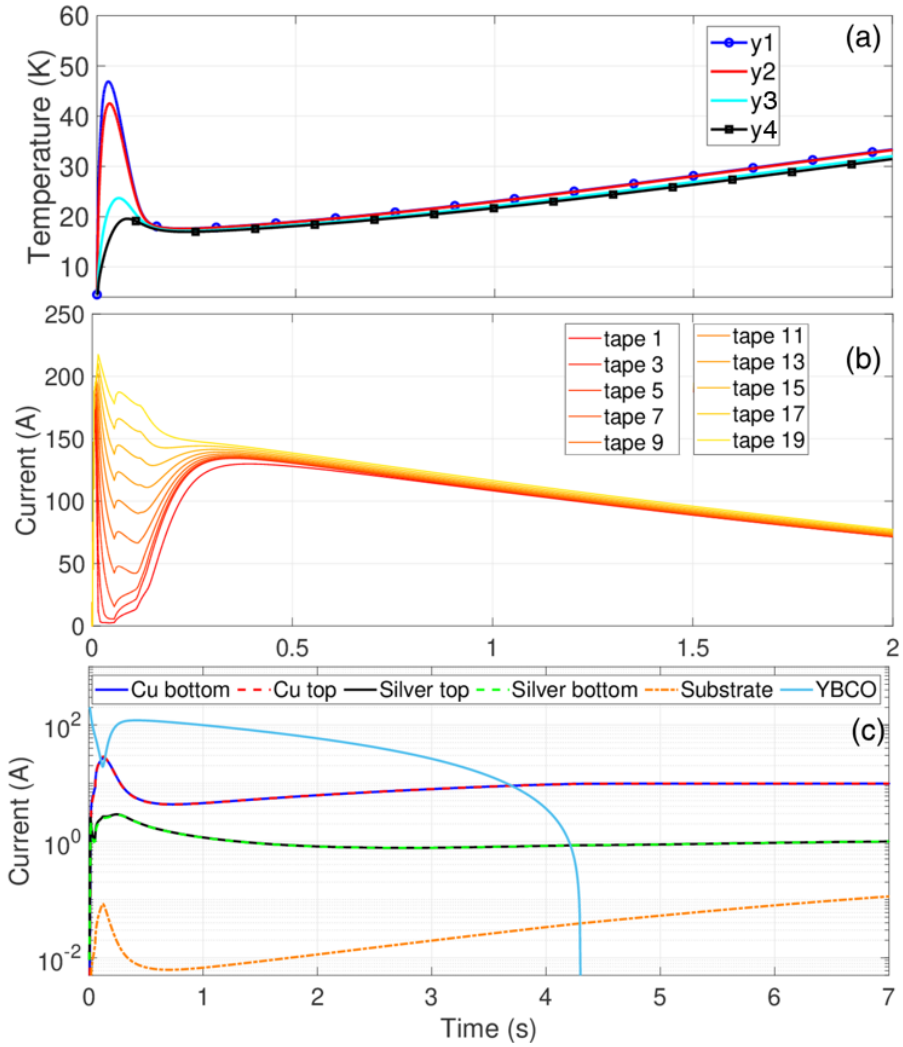

Figure 2.9: 2D electro-thermal model results: evolution of the temperature in selected locations (y1-y4 in figure 2.8) (a). Evolution of the current in the superconducting layer of each tape (even numbered tapes are not shown for clarity) (b). Evolution of the current in the layers of the 10^{th} tape (c).

that the temperature difference can grow even further. Outside the stack of tapes, there are also contact resistances - not considered in the present model - between the solder and the stack and between the solder and the copper tube. Also, the strong mechanical loads acting on the conductor during its nominal operation in a coil could induce a detachment of the solder from the stack, leading to a null thermal contact in some region of the strand between the stack and the surrounding solder. All these considerations point to the possibility of having even larger temperature difference within the *strand* cross-section during a quench, i.e. not only in the conductor cross-section.

Therefore, a possible lumping strategy which is at the foundation of a thermal-hydraulic model of the entire conductor, should account at least for the possible different thermodynamic state of the stack with respect to the solder + copper around it. This approximation seems reasonable, because it could lead to a relative error on the temperature, based on the 2D electro-thermal model results, of less than 5%.

The 2D electro-thermal model of the strand allows also to compare and assess the reliability of the results computed by the 0D electric + 2D thermal model of the conductor cross-section presented in section 2.2.1. The comparison of the current evolution computed by the two models is reported in figure 2.10. Starting from the end of the transient, it can be noted that current flowing in the stack, according to the stack model, is ~ 1 kA, while in the conductor cross-section model is zero. This is because the strand model accounts for the presence of the copper and silver layers, which can transport current even after the transition to the normal state of the superconductor, while the stack in the conductor model is approximated as a unique superconducting region, which, after the quench, carries no current. Even with this approximation, the qualitative evolution of the current is well captured by the conductor cross-section model: the (fast) sharing of the current from the stack to the copper during the heating and the subsequent attempt of recovery after the end of the heating are all well simulated by the conductor cross-section model, which features just a 0D model for the current. Note that the comparison has been performed on the directly heated strand, because the strand model simulates in detail just one (and that) strand, while the conductor model accounts for the presence of all the strands.

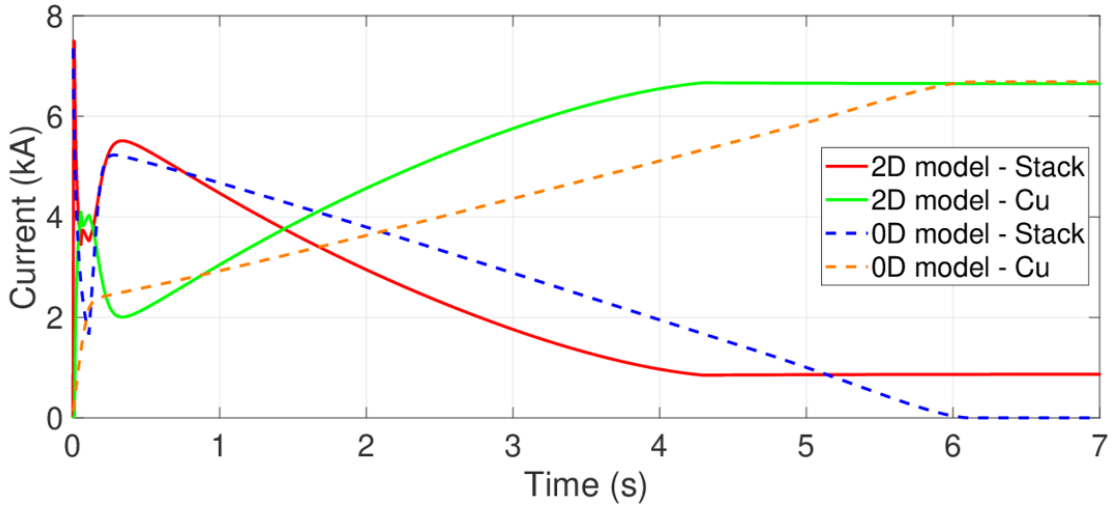

Figure 2.10: Comparison of the evolution of the current the HTS stack and surrounding copper tube computed with the 2D electro-thermal model and the 2D thermal + 0D electric model

Concerning the temperature distribution in the strand, extracting a map of the temperature within the stack during the quench propagation, see figure 2.11, it is evident

that strong temperature gradients are present also in the axial direction; therefore, in view of the development of a 1D model, it needs to be equipped with a mesh adaptive algorithm, in order to refine the region where the quench front is, while sparing mesh elements where no temperature or current variations are present.

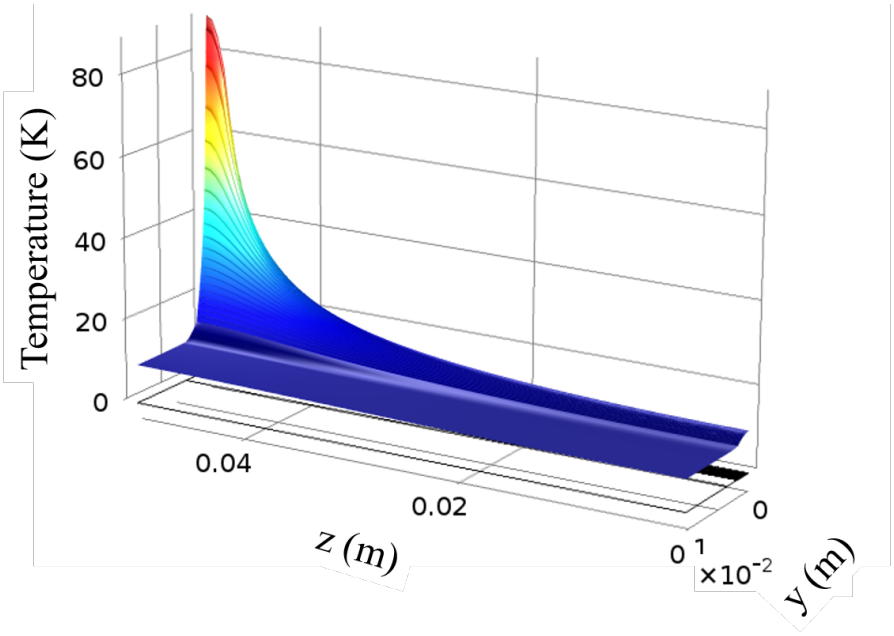

Figure 2.11: Distribution of the temperature computed by the 2D electro-thermal model 0.2 s after the beginning of the heat pulse.

Chapter 3

1D Model Development: the H4C code

3.1 General features

The description of the new conductor model for the simulation of fast transients in HTS conductors is based on the CroCo CICC. However, it has been developed in order to be flexible and simulate other conductors, see section 5.1.2.3.

The detailed analyses have shown that to simulate fast thermal-hydraulic and electric transients in cables based on TSTC idea, it is necessary to discretize the cross-section of the cable with a larger number of thermal and electric regions than in the typical LTS CICC models. In particular, the low (and anisotropic) thermal conductivity of the stack and the non-zero thermal resistance between the strands lead to non-negligible temperature gradients in the cable cross-section, thus leading to a non-uniform current distribution. It is then necessary to model separately each strand (and the stack and the surrounding copper profile separately within each strand). The temperature difference among the strands and/or the presence of a non-negligible electric contact resistance can lead to non-uniformity of the current distribution in the cable cross-section, thus also the current model should be segregated in multiple 1D regions.

The level of discretization of each strand is based on the 2D electro-thermal analysis of the CroCo strand. It has been shown that temperature difference between the stack and the surrounding copper profile are present during the quench initiation, while during the quench propagation the temperature of the different regions becomes basically uniform. Thus, the strand should be approximated with at least two different 1D thermal regions, and, of course, two different electric regions, since redistribution of the current occurs during the propagation of the quench.

Concerning the coolant, considering as reference the CroCo CICC shown in figure 3.1, it can flow in the different voids available among the strands. A realistic assumption is that poor or no mixing is present between the different voids. Additionally, as discussed above, the temperature of the strands can be different during the transient to be

simulated, thus, since the coolant is in contact with different strands, the fluid regions can reach different temperatures. These considerations lead to the need of several fluid regions to be described by different thermodynamic states, thus with several 1D fluid regions, one for each fluid sub-region present in the cable cross-section.

Summarizing, the model needs to take into account the presence of multiple 1D coupled thermal, electric and fluid regions in order to guarantee the flexibility needed for the simulation of different CICC designs. In this case, the tight coupling between the HTS stack and the surrounding copper is taken into account directly in the model, see below.

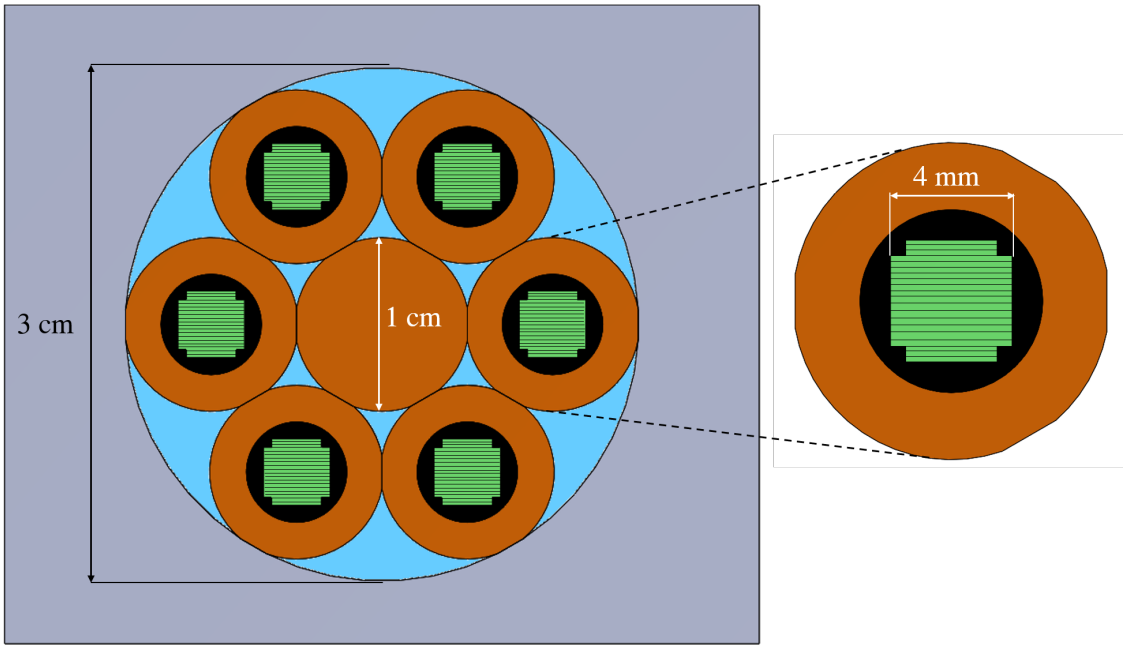

Figure 3.1: Cross-section of the HTS CroCo CICC. THe jacket is represented in grey. The copper tube and central copper rod is colored in orange, while the solder in black. The HTS stacks are green and the voids where the coolant flows are in light blue. A zoom of the single HTS CroCo is also reported.

3.2 Mathematical formulation

The temperature along the axial direction of the solid components of the conductor is modelled with a 1D transient heat conduction equation. Two equations are solved for each strand, see eq. 3.1a and eq. 3.1b, since it is discretized as a 2-regions component:

a superconducting (SC) region and a copper (Cu) region.

$$(\rho c_p A)_{SC,i}\frac{\partial T_{SC,i}}{\partial t} - \frac{\partial}{\partial x}\left[(kA)_{SC,i}\frac{\partial T_{SC,i}}{\partial x}\right] = \sum_{p=1}^{N_{strands}}(UA')_{SC,i\leftrightarrow p}\cdot(T_{p,i}-T_{SC,i}) + \sum_{j=1}^{N_{fluids}}(Ph)_{SC,i\leftrightarrow j}\cdot(T_j - T_{SC,i}) + q'_{SC,i} \tag{3.1a}$$

$$(\rho c_p A)_{Cu,i}\frac{\partial T_{Cu,i}}{\partial t} - \frac{\partial}{\partial x}\left[(kA)_{Cu,i}\frac{\partial T_{Cu,i}}{\partial x}\right] = \sum_{p=1}^{N_{strands}}(UA')_{p\leftrightarrow Cu,i}\cdot(T_{p,i}-T_{Cu,i}) + \sum_{j=1}^{N_{fluids}}(Ph)_{Cu,i\leftrightarrow j}\cdot(T_j - T_{Cu,i}) + q'_{Cu,i} \tag{3.1b}$$

Each i-th thermal component (or strand) can be coupled with:

- other strands or thermal components, more in general, described by the temperature T_p and through an equivalent transmittance U, computed as the inverse of the product of the thermal resistance between the two components, R, and the contact area per unit length, A', thus resulting in $U = 1/(R \cdot A')$. In the specific case of the HTS CroCo CICC, there is no direct thermal coupling between an SC component and another, thus the first term on the right-hand side of eq. 3.1a is limited to the i-th SC-Cu couple. However, it has been implemented the possibility to have a direct coupling between different superconducting regions, such as in the case when more than one regions are chosen to discretize the HTS stack.
- fluid regions with a temperature T_j and through a heat transfer coefficient h and a wetted perimeter P, see the second term on the right-hand side of eq. 3.1b and eq. 3.1a.

Thermal regions which are different from a strand as in the CroCo case, e.g., the central pure copper rod or the jacket, can be simulated putting to zero the heat transfer between the "SC" and "Cu" equation and, of course, considering the proper material properties.

The presence of heat generation in the i-th solid region is accounted for in the term q', which could be larger than zero in case of AC losses and/or Joule power deposited during a quench.

The thermal-fluid dynamics of the coolant is modelled with a set of 1D Euler-like equations, written in non-conservative form, solving for the coolant speed, pressure

and temperature [65]. The set of equations 3.2a-3.2c is solved for each j-th fluid region.

$$\frac{\partial v_j}{\partial t} + v_j \frac{\partial v_j}{\partial x} + \frac{1}{\rho_j}\frac{\partial pj}{\partial x} + 2 f_j v_j \frac{|v_j|}{D_{h,j}} = 0 \tag{3.2a}$$

$$\begin{aligned}
&\frac{\partial p_t}{\partial t} + v_j \frac{\partial p_j}{\partial x} + (\rho c^2)_j \frac{\partial v_j}{\partial x} - 2(\phi \rho f v^2)_j = \\
&\frac{\phi_j}{A_j}\left(\sum_{i=1}^{N_{strands}} (Ph)_{SC,i\leftrightarrow j} \cdot (T_{SC} - T_j) + \right. \\
&\left. \sum_{i=1}^{N_{strands}} (Ph)_{Cu,i\leftrightarrow j} \cdot (T_{Cu} - T_j) + q'_j \right)
\end{aligned} \tag{3.2b}$$

$$\begin{aligned}
&\frac{\partial T_j}{\partial t} + v_j \frac{\partial T_j}{\partial x} + \phi_j T_j \frac{\partial v_j}{\partial x} - 2(f v^2)_j \frac{|v_j|}{(c_v D_h j)} = \frac{1}{(c_v \rho A)_j} \\
&\left(\sum_{i=1}^{N_{strands}} (Ph)_{SC,i\leftrightarrow j} \cdot (T_{SC} - T_j) + \right. \\
&\left. \sum_{i=1}^{N_{strands}} (Ph)_{Cu,i\leftrightarrow j} \cdot (T_{Cu} - T_j) + \phi_j q'_j \right)
\end{aligned} \tag{3.2c}$$

Since a 1D model is adopted, the shear stress at the solid walls and the heat transfer with the solids have been lumped in the friction factor, f, and heat transfer coefficient, h, which contain the information of the distributed pressure loss along the hydraulic length and the convective resistance between the fluid bulk temperature and the (surface) temperature of the solids.

In order to provide suitable friction factor and heat transfer coefficient to the 1D model, given also the large variation of the conductor designs, which lead to several different coolant paths, a feasible and flexible strategy is to develop correlations tailored on the given geometry using Computational Fluid Dynamics (CFD). This strategy was used also in this work, see section 5.1.3.1.

The evolution of the current in each current-carrying element is computed with a distributed parameter model [66], which solves a diffusion-like equation in each electric region. This approach has the advantage of taking into account the transverse resistance present between electric elements, while in the typical approach used for LTS CICC modelling, e.g., in 4C, it is assumed that a perfect transverse coupling is present. Also, the typical approach assumes steady (at each time step) condition for the current, thus not accounting for inductive effects. Of course, the cost to be payed to have a more complete model is to solve a set of partial differential equations rather than a much simpler non-linear algebraic equation in each node.

The current in each k-th electric region obeys the set of equations reported below in eq. 3.3.

$$\left(\overline{\overline{G}}\,\overline{\overline{L}}\right)\frac{\partial I_k}{\partial t}+\frac{\partial^2 I_k}{\partial x^2}+\left(\overline{\overline{G}}\,\overline{\overline{R}}\right)_m\cdot I_k=0 \tag{3.3}$$

In eq. 3.3, G is the matrix of the transverse electric conductance among all the electric regions. In particular, each element $g_{i,j}$ represents the transverse conductance between the electric region i and j, see eq. 3.4. L is the inductance matrix, where the elements on the diagonal, $l_{i,i}$ are the self-inductance of the region i and $l_{i,j}$ is the mutual inductance (per unit length) between the region i and j, see eq. 3.5. $\overline{\overline{R}}$ is the longitudinal resistance matrix, where $r_{i,i}$ is the resistance per unit length of the electric region i along the region itself, see eq. 3.6. The latter is typically the only contribution considered in the algebraic models used for LTS CICCs, so that the $\overline{\overline{R}}$ matrix is typically diagonal. Also, the scaling law of the superconductor is used in these elements to compute the Joule power which contributes to the last term on the right-hand side of eq. 3.1a and 3.1b.

$$\overline{\overline{G}}=\begin{bmatrix}-\sum_{i=1}^{N_{elec}} g_{1,i} & g_{1,2} & \cdots & g_{1,n}\\ g_{2,1} & -\sum_{i=1}^{N_{elec}} g_{2,i} & \cdots & g_{2,n}\\ \vdots & \vdots & \ddots & \vdots\\ g_{n,1} & g_{n,2} & \cdots & -\sum_{i=1}^{N_{elec}} g_{n,i}\end{bmatrix} \tag{3.4}$$

$$\overline{\overline{L}}=\begin{bmatrix}l_{1,1} & l_{1,2} & \cdots & l_{1,n}\\ l_{2,1} & l_{2,2} & \cdots & l_{2,n}\\ \vdots & \vdots & \ddots & \vdots\\ l_{n,1} & l_{n,2} & \cdots & l_{n,n}\end{bmatrix} \tag{3.5}$$

$$\overline{\overline{R}}=\begin{bmatrix}r_{1,1} & 0 & \cdots & 0\\ 0 & r_{2,2} & \cdots & 0\\ \vdots & \vdots & \ddots & \vdots\\ 0 & 0 & \cdots & r_{n,n}\end{bmatrix} \tag{3.6}$$

The system of PDEs presented above (3.1a-3.1b, 3.2a-3.2b-3.2c, 3.3) is solved using the following strategy. According to the method of lines, the PDEs are first discretized in space, thus obtaining a system of Ordinary Differential Equations (ODEs) in time, using finite elements on an adaptive mesh. The (axial) mesh in each thermal, fluid and electric region is rebuilt at each time step accounting for the evolution of the solution. In particular, dealing with quench simulations, the temperature and the current are expected to have strong gradients across the axial positions of the quench fronts. Thus, in order to properly capture those gradients without employing a huge number of elements, the mesh is refined where needed, i.e. where the conductor temperature is equal to the current sharing temperature, and it is coarsened far from those points [67].

The time marching is performed with a backward Euler scheme and the non-linearities are solved through frozen coefficients. The current redistribution in each node is performed using a Newton-Raphson algorithm, in order to cope with the strong non-linearity of the SC power law.

The coupling between the equations is handled in the following way: in case of strong coupling, i.e. happening on a very short time scale, it is solved implicitly, otherwise the coupling is solved explicitly. The implicit coupling means that the equations are solved together in the same time steps. The explicit coupling means that the coupling term present in the equation to be solved is taken from the previous time step. The implicit coupling has the advantage of being much less prone to numerical oscillations and it allows the use of larger time steps with respect to the explicit one. On the other hand, the explicit coupling has a simpler implementation and it allows the decoupling of the equations, meaning that the memory required to solver the linear algebraic system is smaller and it allows the parallelization of the solution algorithm.

In the particular case of the HTS CroCo CICC, the two thermal equations describing the temperature of the stack and copper of each single strand are solved implicitly, since a tight coupling is present there. However, the coupling between the thermal equations of the different strands is handled explicitly, since it acts on a longer time scale. For the coolant equations, the three equations 3.2a-3.2b-3.2c are solved implicitly for each fluid region, since the three equations are tightly coupled, but the coupling with the thermal regions is solved explicitly, thus taking the value of temperature of the solids of the previous time step. Concerning eq. 3.3, the inductance matrix couples all the electric elements on a very short time scale, thus this set of equations is solved implicitly, otherwise a too small time step would have been required not to have numerical oscillations.

The key differences with respect to the conductor model implemented in 4C are the following:

- the number of thermal, hydraulic and electric regions with which the conductor cross-section can be discretized is arbitrary in H4C, while in 4C the user is forced to use up to two electric, thermal and hydraulic regions;
- the model for the current distribution, as mentioned before, is a distributed parameter or diffusion-like model in H4C, thus accounting for transverse electric resistance which is expected not to be negligible in HTS CICCs, while in 4C it is a simple parallel of resistances between the superconducting and normal conductor regions.
- the equations (for each conductor) are implemented in 4C in a way that prevents its parallelization, which, when dealing with the simulation of an entire magnet featuring several conductors, can strongly reduce the computational time.

3.3 Verification

3.3.1 Order of Accuracy

The most accurate verification procedure is the order of accuracy check [68]. It consists in checking the order of convergence of the solvers implemented in the code. To reliably compute the error on the computed solution, a reference solution is needed, which is here the solution computed with the smallest time step and grid size achievable, since the sets of equations 3.1b-3.1b, 3.2a-3.2b-3.2c, 3.3 has no analytical solution. The equations are solved in time using the implicit Euler scheme; therefore the expected order of convergence is 1. All the equations follow the expected trend with sufficiently large time steps, i.e. 0.1 – 0.01 s, see figure 3.2. Using lower time steps, the error due to the spatial discretization becomes important, therefore the curves saturate towards a constant error. Similar considerations hold for the space convergence analysis: the expected order of accuracy is 1 for all the equations. In principle, the heat conduction equations are solved using a second-order scheme. However, since the solid temperature equations are coupled with that of the fluid that converges with order 1, also the solid temperature is expected to converge with the same order. The order of accuracy check is therefore accomplished successfully, demonstrating that the equations implemented are solved correctly, following the expected order of convergence in both time and space.

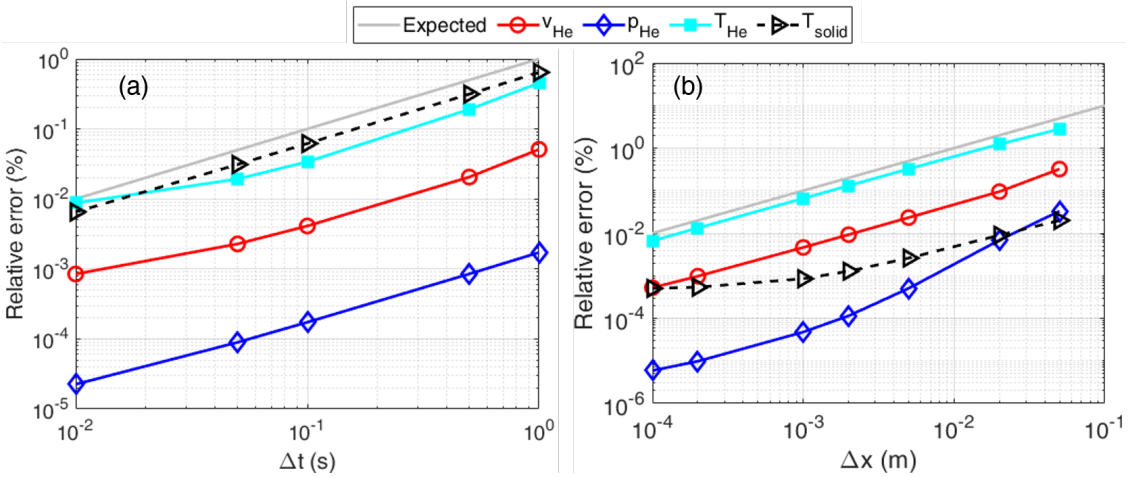

Figure 3.2: Code verification: order of accuracy check in (a) time and (b) space of solid (thermal) and fluid equations. The expected order of convergence is also shown in grey.

3.3.2 Benchmark against the 4C code

Another step in the verification of the H4C model has been performed through a benchmark against the validated conductor model implemented in 4C. The test case is shown

in figure 3.3 and it includes three thermal regions (a superconducting and a copper region - which in 4C are simulated as a single region - and a steel region, simulating the structure of a simple conductor) and a single fluid region. In H4C, the three solid regions are also current-carrying regions. The current is supposed to be constant, the inlet and outlet pressure of the fluid are imposed, as well as the inlet temperature, and the driver of the transient is the power deposition, localized in the region shown in figure 3.3.

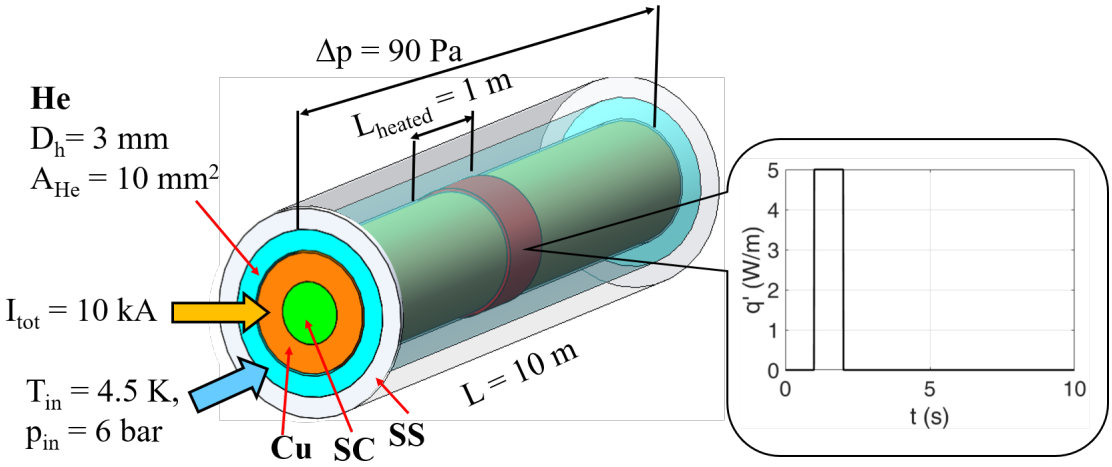

Figure 3.3: Scheme of the test case used for the benchmark with the 4C code. The geometry and simulation setup (fluid boundary conditions and position and evolution of driver of the transient) are shown.

Its value has been chosen in order to induce a quench, to test also the adaptive mesh algorithm. Constant friction factor (0.09) and heat transfer coefficient (1000 W/m^2/K) are assumed in both codes. The solids are supposed to be adiabatic on both sides. The thermal regions facing the external environment are considered adiabatic if not otherwise stated. The mass flow rate value was chosen in order to obtain a visible acceleration of the flow across the normal zone, thus to test the correct solution of the set of equations 3.2a-3.2b-3.2c.

In this setup, the codes are expected to produce the same results, and indeed, as shown in figure 3.4, the results computed by H4C and those computed by 4C are identical. Also other variables, such as the pressure profile, have been compared and they show the same agreement. This means that the equations are solved correctly by H4C as well as that the adaptive mesh algorithm works properly.

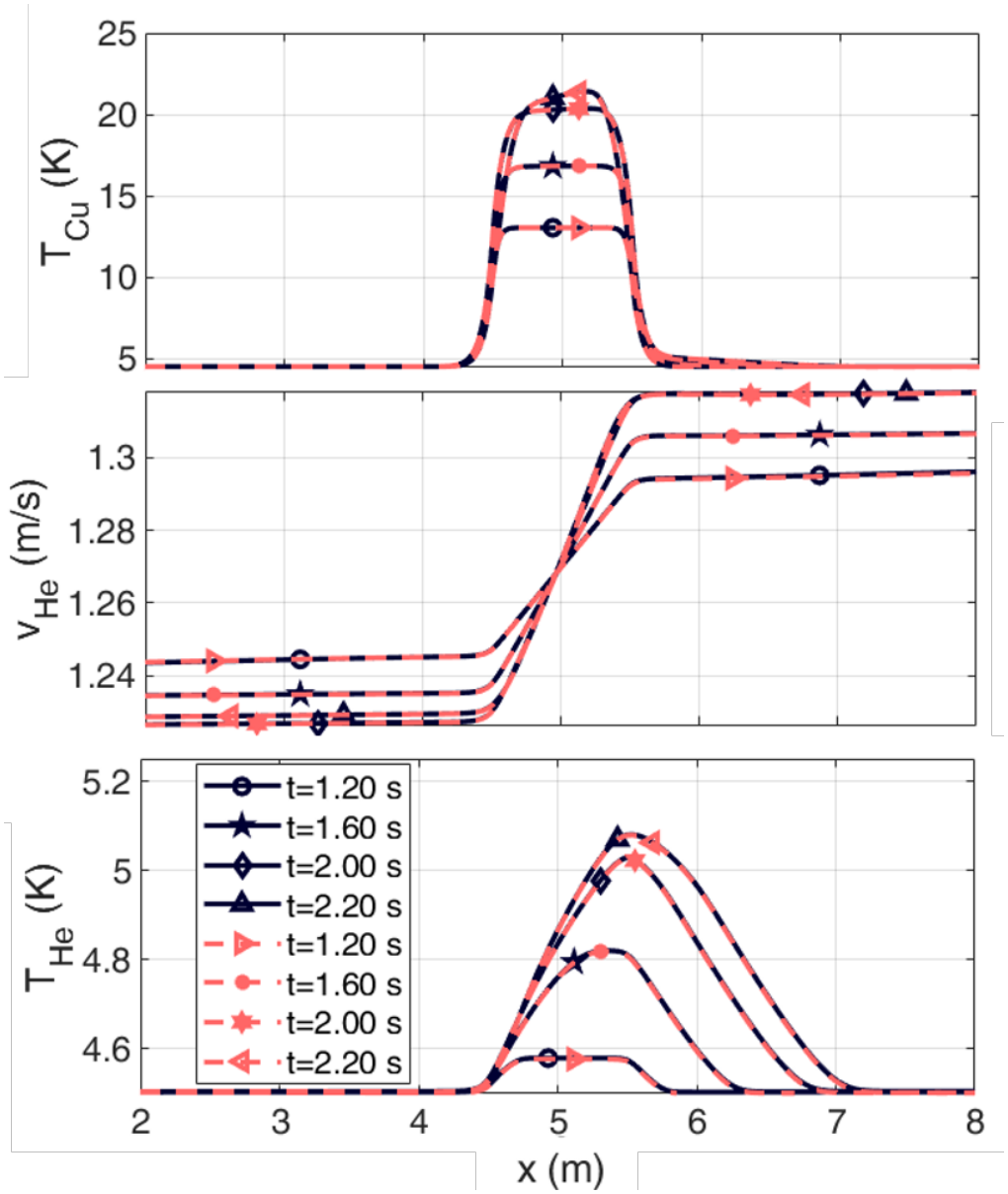

Figure 3.4: Results of the benchmark with the 4C code: evolution of the temperature in the copper (a), speed of the helium (b) and distribution of the helium temperature taken at different instants during the transient. The dashed lines are produced from the results of the new model, the solid lines report the 4C results.

Chapter 4

Preliminary validation

The quench experiments on four conductor samples designed by SPC [69] were successfully completed. Here we report an analysis of the experimental data of both DC and quench tests which are particularly useful to feed the computational model. Preliminary numerical simulations of two quench tests on two different conductors, i.e., the "reference" and the "non-twisted" designs, are also discussed, together with the presentation of the conductor model used for the analysis. The experimental layout useful for the discussion below is reported in figure 4.1. In all the tests, the quench is initiated rising the He inlet temperature beyond T_{CS} with an electrical heater positioned on the inlet pipe.

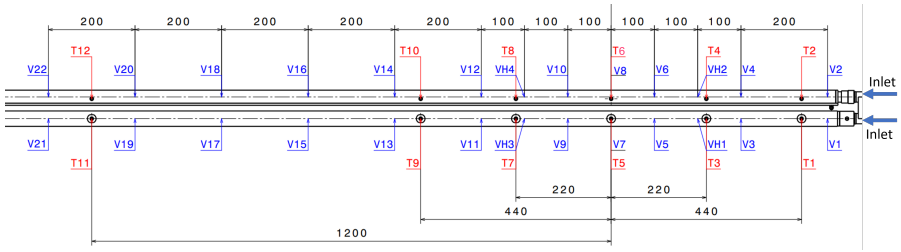

Figure 4.1: Voltage and temperature sensors layout used during the quench experiment, reproduced from [69]. The inlets are shown with the arrows. The HFZ is between T7 and T3.

4.1 DC performance

In this section, the DC performance (critical current, I_C and current sharing temperature, T_{CS}) of the tested samples are discussed.

4.1.1 Critical current

The cable critical current is extracted fitting the average electric field measured with the voltage taps in the High Field Zone (HFZ), as function of the applied current with the following power law:

$$E = E_{offset} + E_C \cdot \left(\frac{I}{I_C}\right)^n \tag{4.1}$$

where E_{offset} is an electric field offset, E_C is the critical field equal to 100 $\mu V/m$, I is the transport current, I_C is the critical current, and n is the n-value of the cable, which rules the transition from the superconducting to the normal state. The fitted quantities are E_{offset}, I_C and the n-value. The voltage, thus the electric field, is averaged in each time interval when the current is constant. The critical current is then used to compute the "effective" superconducting cross-section which is in turn used as input for the numerical model. The calculation is simply done according to the following:

$$A_{SC} = \frac{I_C}{J_C(B,T)} \tag{4.2}$$

where A_{SC} is the cable (total) superconducting cross-section and J_C is the superconductor scaling law, B is the magnetic field and T the superconductor temperature. The scaling law adopted is taken from [58]. As an example, the fit of the electric field as a function of the current is shown for the not-twisted sample, see figure 4.2.

From the fit, the values of I_C and n-value are computed. Their average (among the different couples of voltage taps) is considered for further analyses. The average values are summarized in table 4.1 for the two different conductors tested.

Table 4.1: Average critical current and n-value for the two conductors analysed

Conductor	Critical current (kA)	n-value
Not twisted (L2)	13.9 (7 K, 7 T)	16.4
Reference (R3)	14.5 (5.6 K, 4 T)	8.6

4.1.2 Current sharing temperature

The current sharing temperature is taken as the value at which the electric field in the HFZ reaches E_C = 100 μV/m. In this case, the average of the four crown sensors (VH) across the HFZ are considered. When available, tests at different magnetic fields have been analysed. The experimental results are also used to cross-check the soundness of the scaling law adopted for the modelling of the samples.

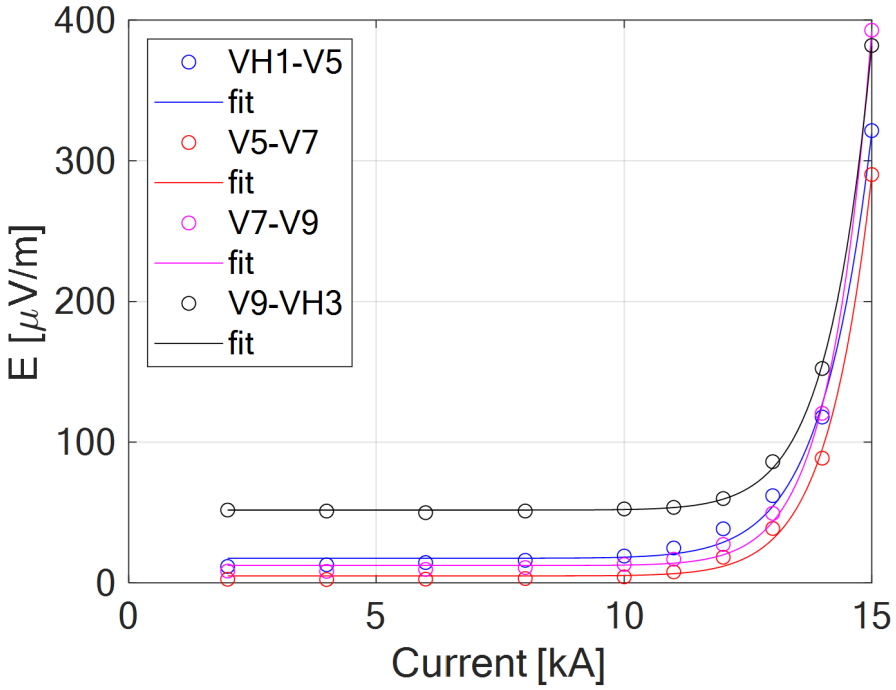

Figure 4.2: Fit of the electric field as a function of current for the four couples of voltage taps in the HFZ. Refer to figure 4.1 for the sensors location.

Table 4.2: T_{CS} of the two samples analysed

Conductor	$T_{CS}(K)$
Not twisted (L2)	7.17 (15 kA, 6 T)
Reference (R3)	6.96 (15 kA, 3.5 T)

4.2 Quench experiments

In this section, a preliminary analysis of the experimental results is carried out. In particular, key features of the quench propagation, such as the normal zone propagation velocity (NZPV) and the hotspot temperature, are assessed.

4.2.1 NZPV

The NZPV is assessed considering the voltage measurements. The reason is that, in principle, the voltage signals are the most reliable for this estimation since they instantly react to the normal zone propagation. The alternative could be to use the temperature measurements. However, they typically react on the scale of seconds and delays are not acceptable for the purpose of assessing the NZPV. The rationale followed for the

estimation of the NZPV in the HFZ is the same adopted for the analysis of quench in LTS [70] and it is summarized below. To fix the ideas, let us suppose that the quench starts in V5-V7, i.e., between voltage taps V5 and V7. Let us also focus on only one front, e.g., the left front, i.e., the front that is propagating towards the He outlet. As soon as the front enters the region between V7-V9, the voltage measured by that couple of voltage taps starts increasing at time t_{V7V9}. The front travels and then enters the region between V9 and VH3. Here a resistive voltage starts to be measured, say at t_{V9VH3}. Therefore, the front took $\Delta t = t_{V9VH3} - t_{V7V9}$ to travel from V7 to V9, thus to travel $\Delta L = 10\,cm$. The average velocity in that interval can then be computed as $\Delta t/\Delta L$. From this, it is clear that to compute a single value of propagation speed, two couples of voltage taps are needed. It is also clear that the couple in which the resistive voltage is measured first, i.e. the portion in which the quench starts propagating, cannot be used to estimate the NZPV there. Looking at the quench tests on L2, it appears that the couples V1-V3 and V11-V13 start measuring a voltage too soon, see figure 4.3(a), thus they cannot be considered reliable and used to estimate NZPV. The region of interest to quantify NZPV is the HFZ, thus V11-V13 and V1-V3 would not have been useful for this purpose, since the sharp decrease of the magnetic field strongly impact on the NZPV. The propagation of the right front, in case the quench starts in V5-V7, can be characterized with a single value of speed, i.e., that computed using VH1-V5 and V3-VH1. Instead, on the other side, two values can be computed using V7-V9 with V9-VH3 and V9-VH3 with VH3-V11. Another crucial point is to define a voltage, or equivalently an average electric field, to confirm that the front has entered for the first time between a couple of voltage sensors. Here a threshold of $E_{threshold} = 0.15\,mV/cm$ will be used, see figure 4.3(b). This threshold has been set low enough to exclude as much as possible the increase of voltage due to the temperature increase, but sufficiently high to exclude sensor noise. There are shots in which the electric field in V9-V7 crosses first the threshold, i.e., the quench is assumed to start propagating there, therefore the velocities that can be computed are those between V5-V7, VH1-V5 and V9-VH3. In any case, using this strategy, three values of NZPV can be computed, at best: two for the left front and one for the right front or vice-versa. The NZPV (indirect) measurement should be improved, since, from the available set of measurements, only one value of acceleration can be computed in only one quench front. Indeed, for the next experiments, more voltage taps will be employed in the HFZ.

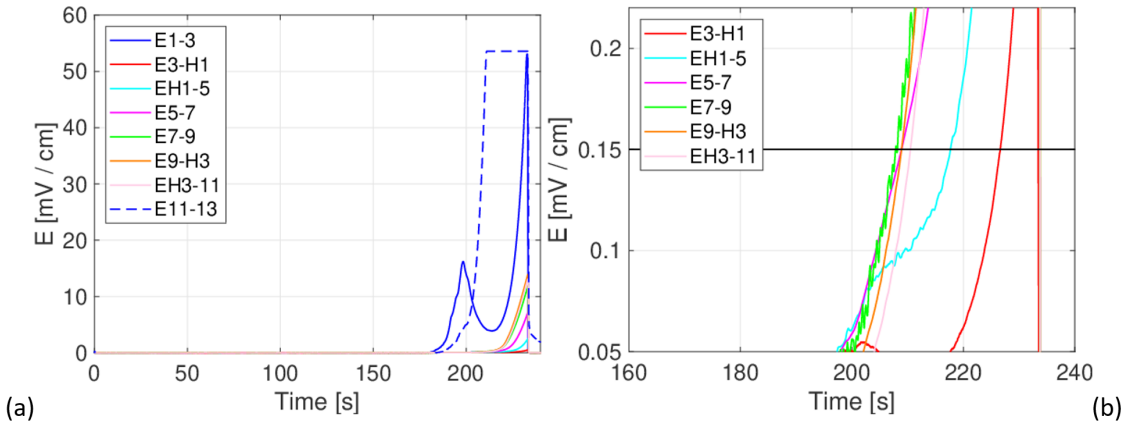

Figure 4.3: (a) Evolution of the average electric field during shot 170807. The zoom where the $E_{threshold}$ is set is shown in (b).

The results on the quench tests on L2 are summarized in table 4.3.

Table 4.3: NZPV (mm/s) in L2

Shot	VH1-V5	V5-V7	V7-V9	V9-VH3
170802	68	-	103	39
170803	28	-	61	64
170804	18	-	67	64
170805	43	223	-	45
170806	46	-	84	51
170807	11	11	-	107
170808	23	305	-	144
180801	63	236	-	52
190804	107	-	72	42

Note that, according to the strategy reported above, the quench starts sometimes between V5-V7 and other times between V7-V9. The electric field in V5-V7 and V7-V9 are always very close and the decision on where the quench starts depends on $E_{threshold}$. As a result, high values of NZPV can be found, much larger than the average value. They are not fully reliable, while, on the other hand, VH1-V5 and V9-VH3, being always further from the initiation zone, lead to less noisy values. In any case, the strategy adopted and the data available lead to NZPV ranging from 20 to 70 mm/s, confirming that the NZPV in HTS CICCs is 1-2 orders of magnitude lower than in LTS CICCs [70].

4.2.2 Virtual temperature

In the experiment, not only (as usually done for LTS tests) the jacket temperature, but also the He temperature is directly measured. Nevertheless, the hot spot cable temperature (namely, the copper and HTS stack temperature) is not measured. An experimental indication (the so-called "virtual sensor") of the hot spot temperature in the cable ($T_{HOTSPOT}$), can be extracted from the voltage measurement VD_{ab} between two generic voltage taps a and b, following a well-established strategy for the LTS, see e.g. [71], solving for $T_{ab} = T_{HOTSPOT}(exp)$ the implicit equation

$$VD_{ab} = \rho_{Cu}(T_{ab}) \cdot (L_{ab}/A_{Cu}) \cdot I_{Cu} \tag{4.3}$$

where L_{ab} is the strand length between a and b, assuming that from a simple electrical model with two resistors in parallel (jacket and Cu) it is possible to estimate the current I_{Cu} flowing at any time in the Cu strands and in the Cu fraction of the HTS stacks, and knowing the dependence of the Cu (and steel) resistivity ρ_{Cu} on the temperature [56]. Note that the Cu resistivity also depends on the residual resistivity ratio (RRR), assumed here to be 100. This procedure is based on the following assumptions:

- the cable temperature is uniform (both on the cross section and along the axis length) between a and b, i.e., T(x) = T_{ab}
- the entire length L_{ab} is normal, i.e. both quench fronts have already crossed both boundaries a and b.
- no current is flowing in the SC
- temperature of the copper equal to that of the jacket, in order to compute the current repartition between cable, i.e. Cu, and jacket (the effect of this assumption on the current repartition is small, because the steel resistivity relative variation with temperature is much smaller, in the considered range, than that of the Cu.)

While the second assumption can be guaranteed by the measurements (if the quench is initiated in L_{ab} and also the two VD signals closest to VD_{ab} measure a non-zero voltage, it means that the quench fronts crossed both boundaries), the first assumption needs to be confirmed by a reliable numerical analysis. In order to assess the validity of this method to estimate the $T_{HOTSPOT}$ also in the specific case of the L2 SPC sample, the H4C simulation results reported in Section 4.4.2 are used as reference, thanks to the good agreement between experimental and computed results (as far as the jacket and He temperature is concerned) reported in Section 4.3.3.1, after the proper calibration of the code (see below). Applying the above-mentioned methodology to the simulation results for the shot 170802, with special reference to the V5-V7 pair of voltage taps, the $T_{HOTSPOT}$ estimated is 95 K (with 0.5 kA in the jacket, 14.5 kA in the Cu). It turns

out to be 15 K larger than the He temperature computed with the H4C code in T5 (80 K), as expected, being the cable temperature higher than the He one. The evolution of the measured voltage and temperature within VH1 and VH3 for shot 170802 is shown in figure 4.4. The $T_{HOTSPOT}$ evaluated with the virtual temperature sensor shown in figure 4.4(b) is 50-60 K higher than the measured He temperature. The hot-spot temperature in the cable looks then to be higher than the He temperature, as expected. Note that this difference is even larger than the above-mentioned 15 K in the simulation, as the simulation shows a less steep (and smaller, in absolute terms) voltage increase. The $T_{HOTSPOT}$ evaluation will be further cross-checked with other H4C simulations.

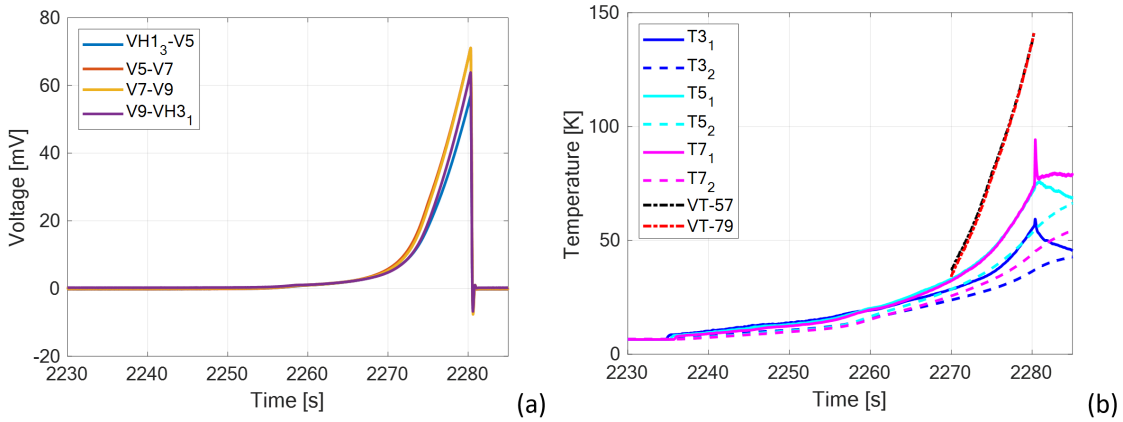

Figure 4.4: Evolution of (a) the measured voltage and (b) the measured temperature in the region within VH1 and VH3, for the shot 170802. In (b) the virtual hot-spot temperature (VT) evaluated from a subset of the voltage measurements in (a) is also reported.

4.3 H4C model

The H4C code [46] simulates an arbitrary number of thermal, fluid and electric 1D regions, solving the heat diffusion, a set of Euler-like equations and a diffusion-like equation for the current, respectively, see chapter 3. The development of the H4C model of the tested samples was focused on L2 and R3 in order to analyze first REBCO samples (thus excluding for the time being L3) and because the solder properties of the solder-filled sample are not known (thus excluding R2). In order to account in perspective for defects at the strand level, the 3 strands have been modelled separately. Each strand is modelled with two thermal and electric regions (HTS stack and Cu profile around it). Together with a thermal and electric region for the jacket, the total number of electric and thermal regions is 7. On the other hand, the fluid is modelled as a single region, because no local effects are expected. The interfaces between the different regions as

well as the constitutive laws for the fluid and for the superconductor are reported in table 4.4.

Table 4.4: Interface parameters and constitutive laws.

Electric contact resistance	$[\mu\Omega/m]$
Stack-Copper	0.07
Copper-Copper	7
Copper-Stainless steel	70
Thermal contact resistance	$[m^2K/m]$
Stack-Copper	$8 \cdot 10^{-5}$
Copper-Copper	$1 \cdot 10^{-3}$
Copper-Stainless steel	$1 \cdot 10^{-4}$
Friction factor correlation	Petukhov [72]
Nusselt number correlation	Dittus-Boelter [60] (to be calibrated)

4.3.1 Boundary conditions

The boundary conditions considered in these preliminary simulations are the following:
Fluid model:

- Inlet temperature: T1-1;
- Inlet and outlet pressure: such that the mass flow rate agrees with the measured one.

Thermal model of the solids:

- Zero heat flux (adiabatic) at both conductor ends.

Current model:

- Imposed current in SC at conductor outlet;
- Zero current gradient at conductor inlet.

4.3.2 Stack and cable twisting

Except for L2 conductor (not-twisted), all the CICCs are made by a twisted cable: each strand is twisted with a twist pitch equal to 400 mm, then the strand triplet is twisted with a twist pitch equal to 1000 mm. The effect of the twisting on the critical current is taken into account using the approach proposed in [73]. The resulting twist pitch has been computed as superposition of the two twist stages, leading to a twist pitch equal to 285 mm. The resulting distribution of critical current in the HFZ is shown in figure 4.5.

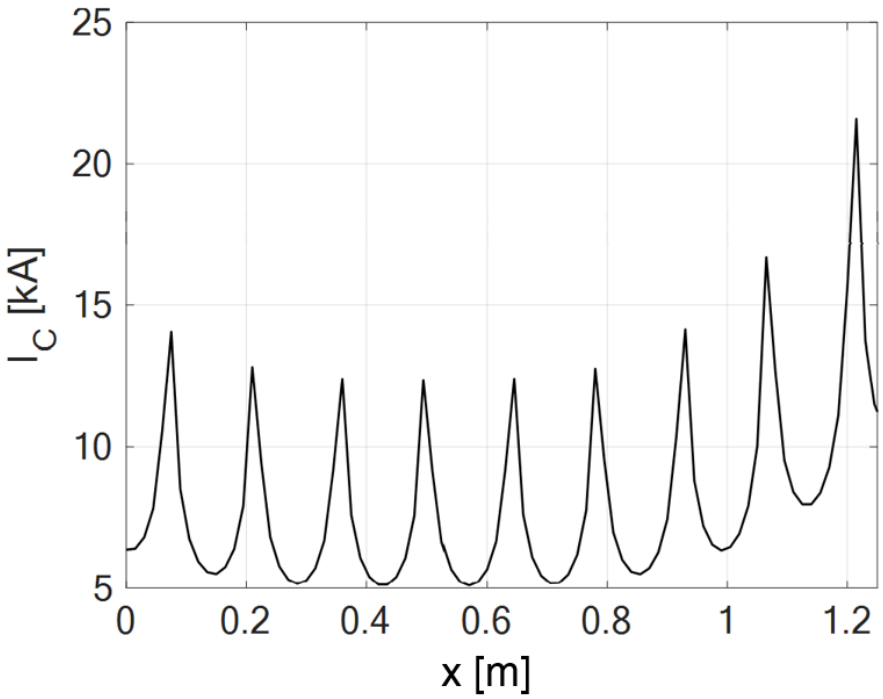

Figure 4.5: Distribution of I_C in the first half of R3 at 3.5 T and 5.7 K.

4.3.3 Model calibration

The rationale of the model calibration is to find the optimal value of a free model parameter, i.e., the value that leads to the best agreement between computed and experimental results on a selected shot. In order to assess the soundness of such calibration, the same type of transient is simulated keeping frozen the model parameter on another – independent with respect to the previous – shot, for which the parameter is not expected to change.

4.3.3.1 Heat transfer coefficient

One of the free model parameters is the heat transfer coefficient between He and Cu strands and between He and jacket. It is a free parameter since it is still not measured on this geometry and/or it would require a dedicated CFD study. Thus, the rationale here is to find the best multiplier M to the Dittus-Boelter correlation based on the heat slug tests, i.e. tests where the heat pulse was not strong enough to induce a quench. The parametric study has been performed on the 30 V - 10 s heat pulse of shot 170802, see figures 4.6 and 4.7. The optimal value of M is between 0.05 and 0.1. The comparison with the T11 sensor is not as satisfactory (especially for the He temperature increase, T11-1). However, the most interesting region is the HFZ, where the He and jacket temperature increases are well captured; therefore this (calibrated) model is then reliably

used for the quench simulations, see Section 4.4.

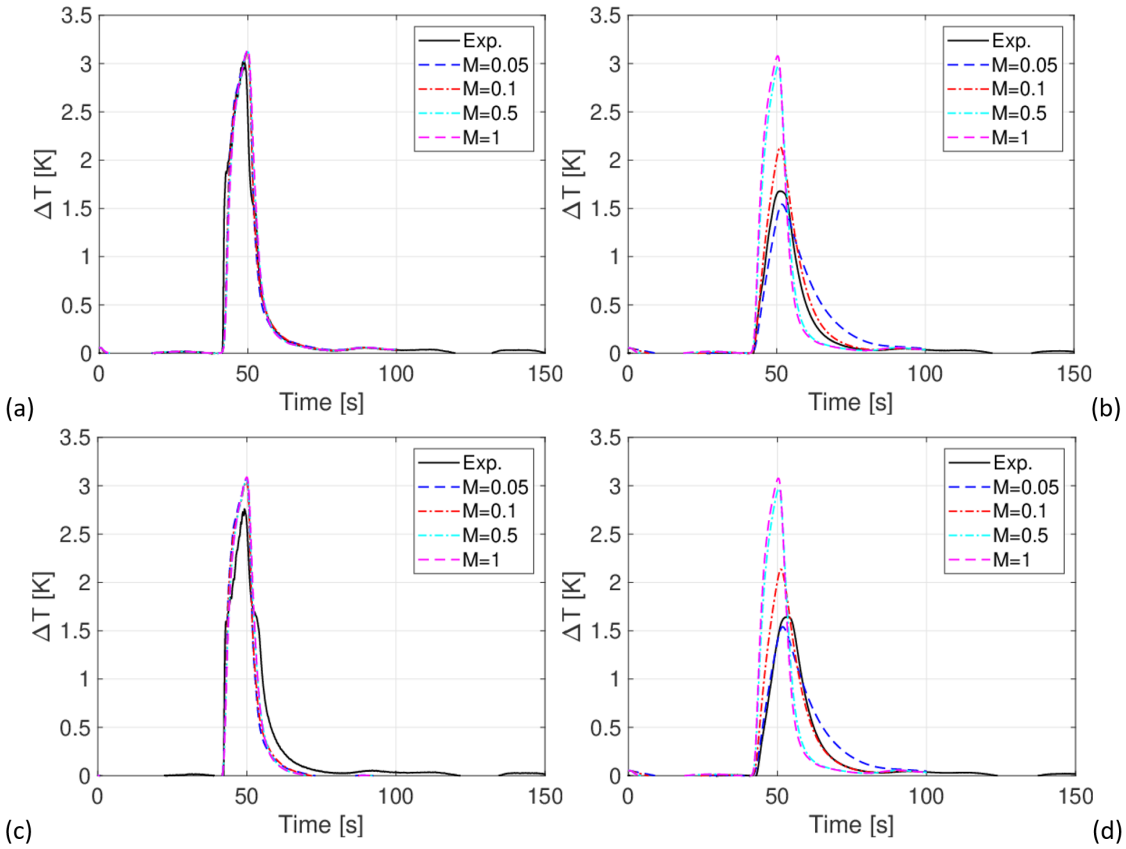

Figure 4.6: Evolution of the measured (solid lines) and computed (dashed or dash-dotted lines) helium (Sensors T#-1) and jacket (Sensors T#-2) temperature increases, parametrically scanning the He-jacket heat transfer coefficient multiplier. Sensors T3-1 (a), T3 - 2 (b), T5-1 (c), T5-2 (d)

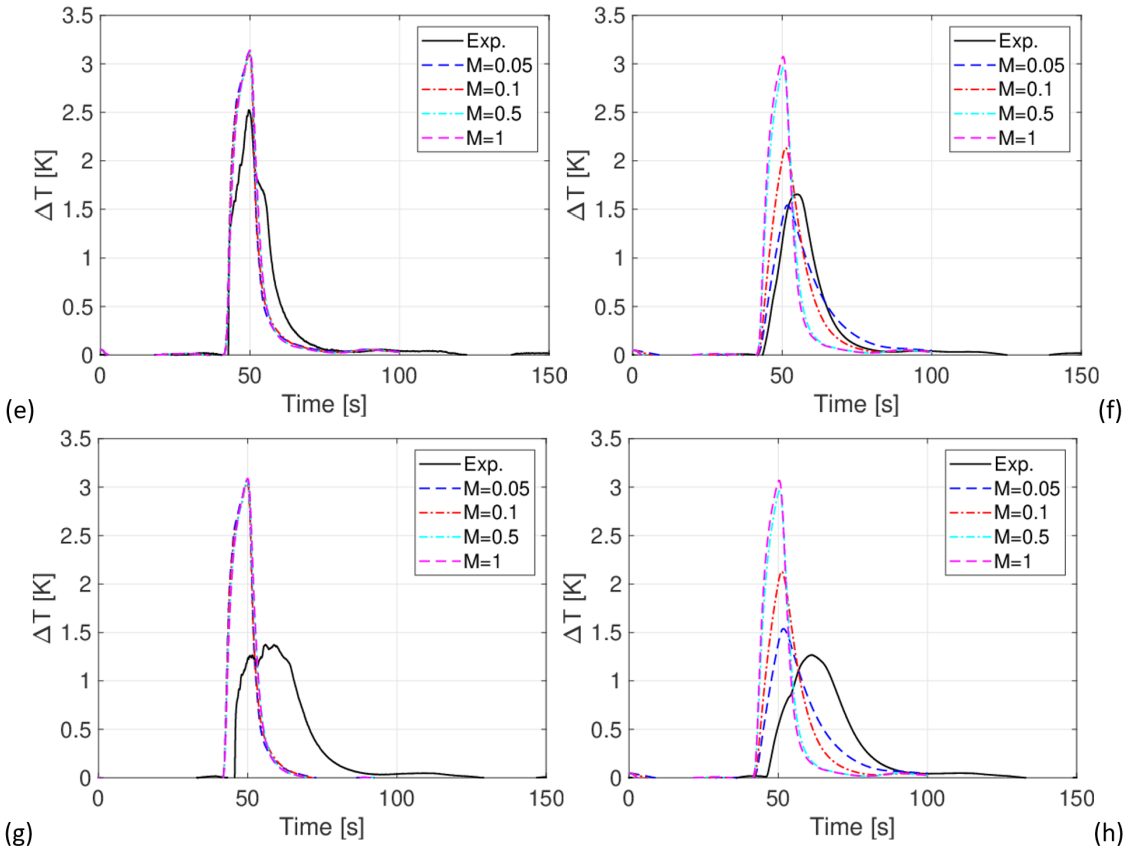

Figure 4.7: Evolution of the measured (solid lines) and computed (dashed or dash-dotted lines) helium and jacket temperature increases, parametrically scanning the He-jacket heat transfer coefficient multiplier. Sensors T7-1 (e), T7-2 (f), T11-1 (g), T11-2 (h)

The cross-check of the calibration is performed on another heat slug, i.e. the 45 V - 10 s heat pulse of shot 170802. This slug was chosen also because it reached higher temperature then the calibration one, thus making the cross-check non-trivial. The agreement between measured and computed helium and jacket temperature increase with multiplier M = 0.05 is satisfactory, see figure 4.8. The same, odd behavior of T11 is also present here, but again the interesting region is the HFZ.

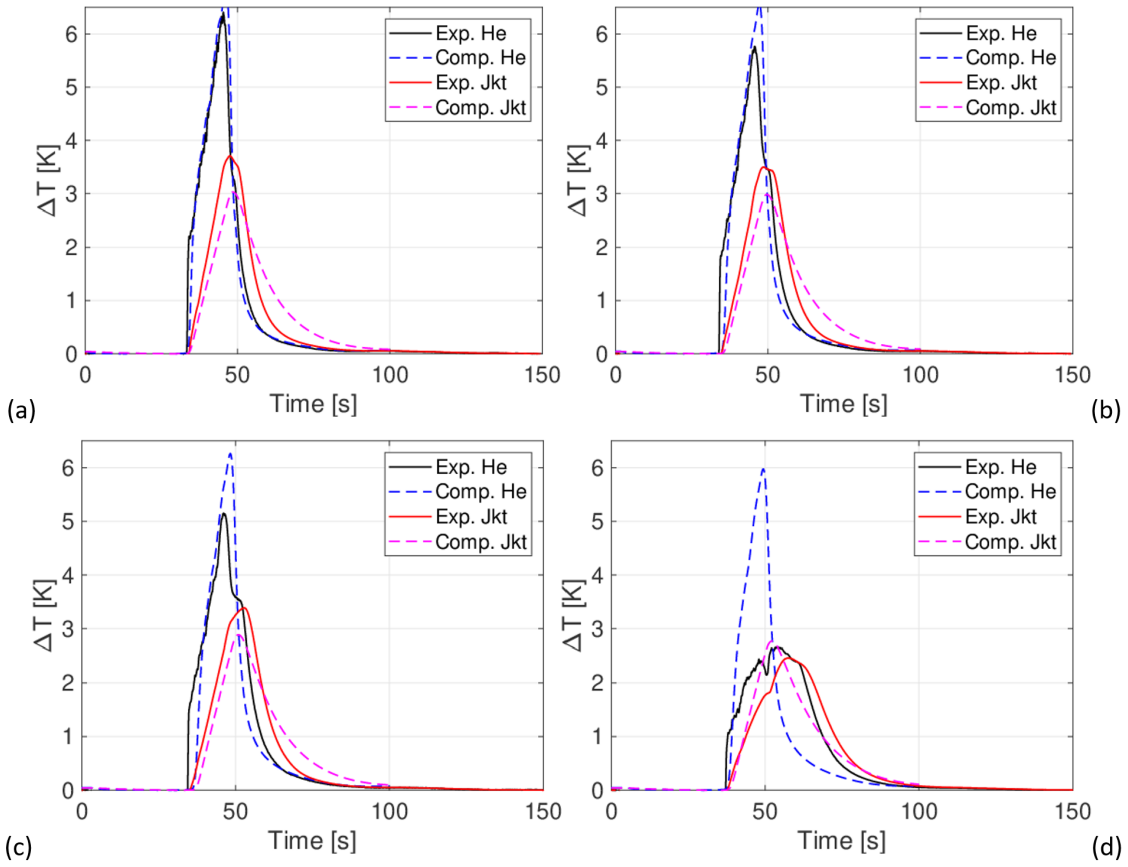

Figure 4.8: Evolution of measured and computed helium and jacket temperature increases in shot 170802 (heat pulse 45 V - 12 s). Sensors T3 (a), T5 (b), T7 (c) and T11 (d) are shown

4.4 Quench simulation results

In this section, the preliminary results of quench simulations carried out with the model described and calibrated before are presented and discussed. The simulated shots are 170802 (L2, not-twisted conductor) and q101102 (R3, reference conductor).

4.4.1 Quench detection and current discharge

The quench detection depends on the strategy adopted during the experiments. For 170802, the detection occurs when the maximum temperature among the sensors reaches 70 K. For q101102, it occurs when the total voltage exceeds 150 mV. The delay time before the current discharge is not known for 170802 and it is assumed to be 0.5 s, while for q101102 is set equal to 4 s. The current discharge characteristic time is assumed equal to 1.1 s.

4.4.2 Shot 170802 (not-twisted conductor)

The comparison of the measured and computed voltages is shown in figures 4.9 and 4.10. For reference, in the following plots t = 0 s corresponds to t = 2200 s of the data file. Since T1-1 is used as He inlet temperature in the model, the computed results are not shifted with respect to those measured. The computed voltages agree well with those measured during initial phase of the quench propagation, i.e. until the total voltage is below 20 mV. After that, the computed voltage grows less rapidly with respect to the measurements. This delay during the quench propagation will be further investigated to improve the model performance. Most probably, the assumed RRR of 100 for the copper is too optimistic (since the measured one is currently not available), indeed a smaller value would lead to a faster increase of the voltage. Nevertheless, in the HFZ, the voltage reaches values that are close to the measured ones, even though with a delay of ~5 s.

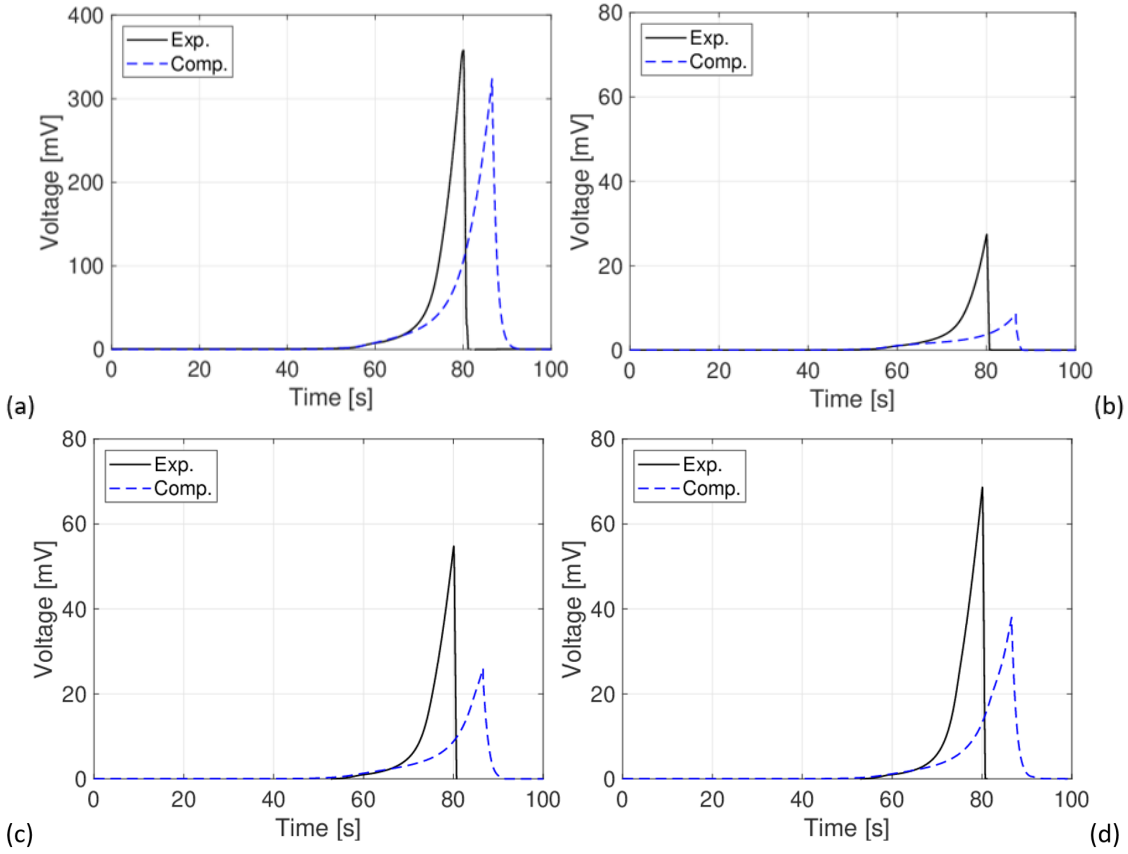

Figure 4.9: Evolution of measured and computed voltage across the entire conductor length (a), V3-VH1 (b), VH1-V5 (c), V5-V7 (d).

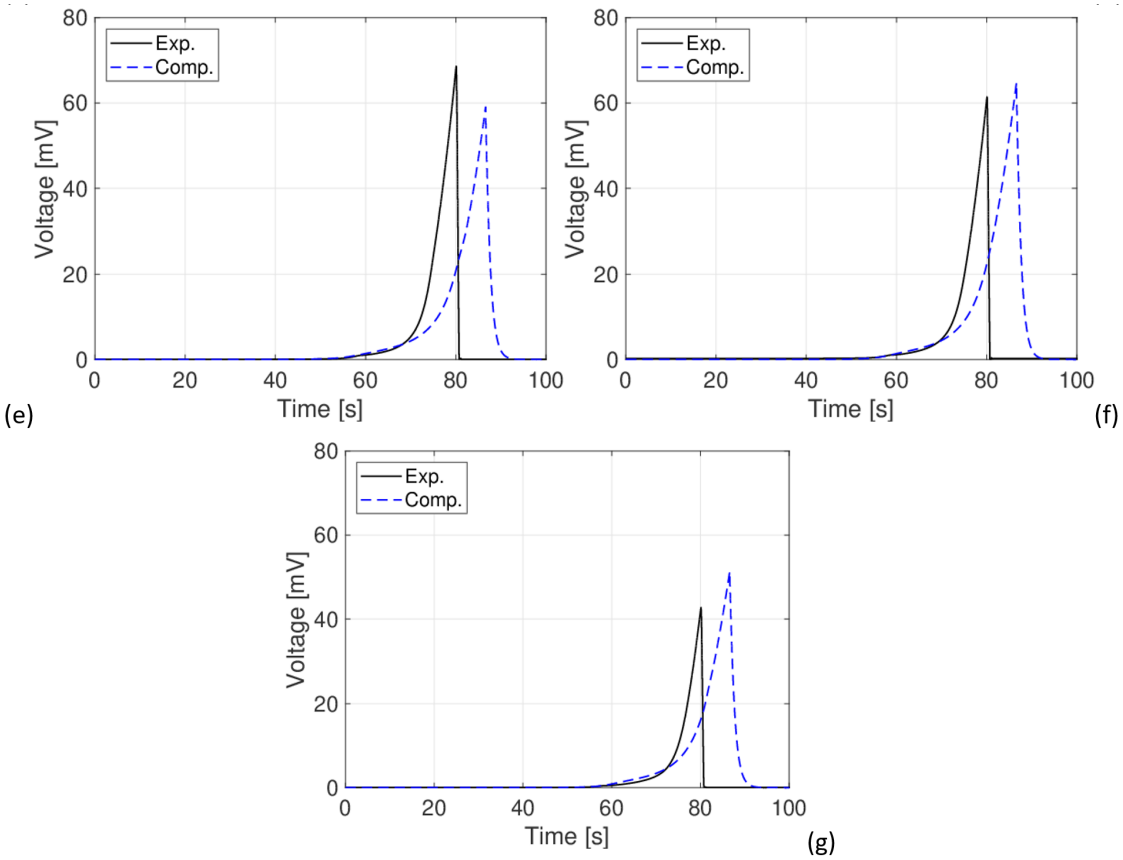

Figure 4.10: Evolution of measured and computed voltage across V7-V9 (e), V9-VH3 (f), VH3-V11 (g).

The computed temperature is compared with the measurements in figure 4.11. As already hinted by the discussion of the voltage results, the initial phase of the quench propagation is well captured by the simulation and the quantitative agreement is good for T3 and T5 for both He and jacket temperature during the increase and decrease of the temperature. The agreement is less good looking at the sensors downstream with respect to the maximum magnetic field position. In particular, the decrease of the temperature due to fresh He entering again in the conductor is slower in the simulations with respect to the measured evolution. Nevertheless, the most interesting phase of the transient, i.e., the quench initiation and propagation, is well captured.

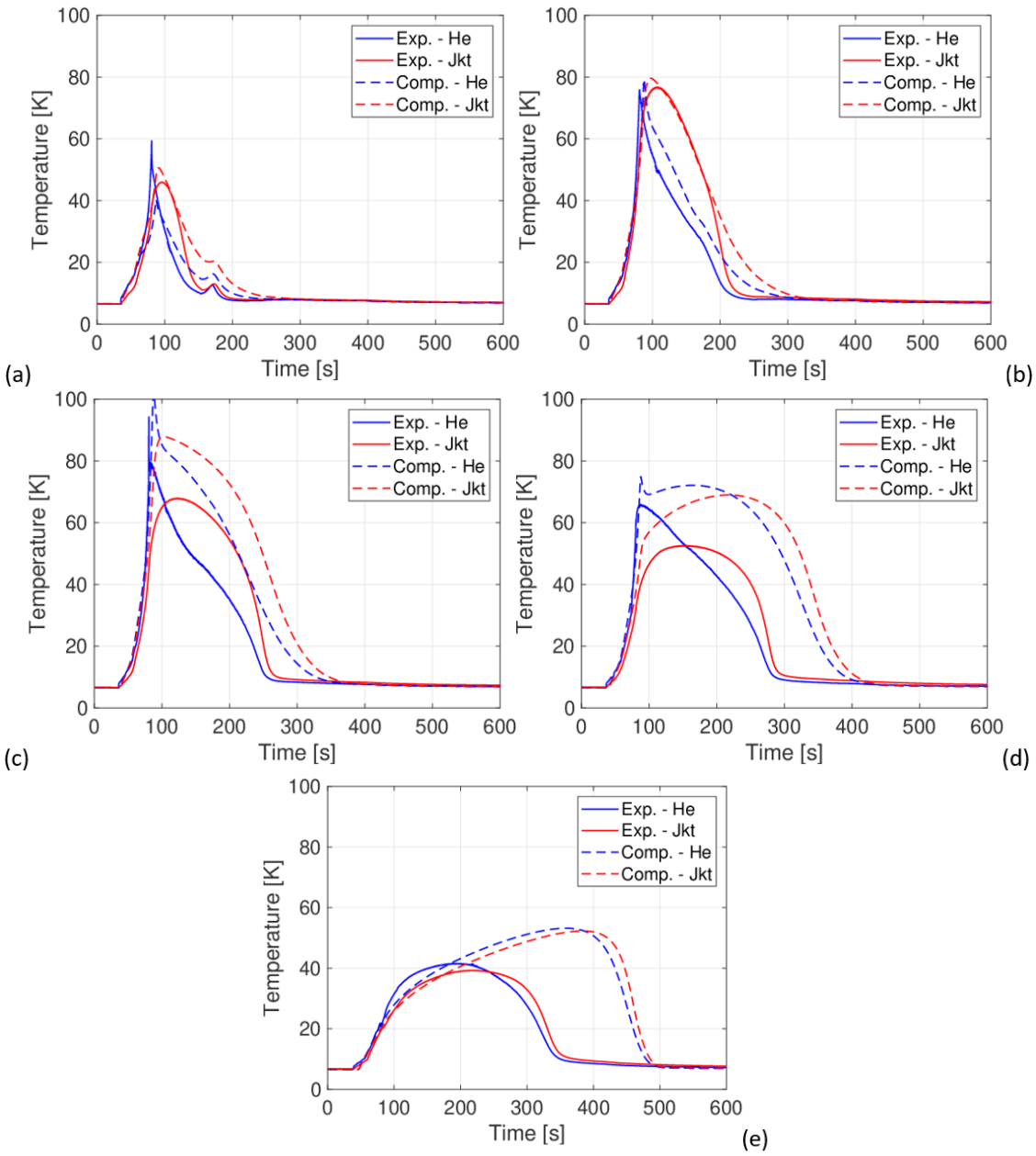

Figure 4.11: Evolution of the measured and computed temperatures at T3-1/2 (a), T5-1/2 (b), T7-1/2 (c), T9-1/2 (d) and T11-1/2 (e).

4.4.2.1 Current redistribution

A first qualitative information that can be extracted from the simulation is the behaviour of the current during quench propagation. figure 4.12 shows the evolution of the current in a stack, in its copper profile and in the jacket. The same current flows for symmetry

in the other two stacks and copper profiles. The plateau reached in the stack is due to the current flowing in the copper stabilizer of the tapes. A non-negligible current flows in the steel jacket, reaching ∼ 550 A before the dump.

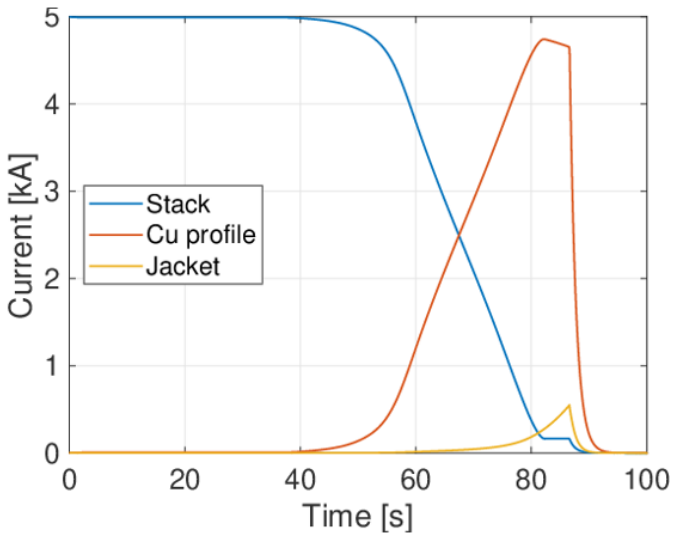

Figure 4.12: Computed evolution of the current in the conductor sub elements.

4.4.3 Shot q101102 (reference conductor)

A qualitatively similar picture emerges from the preliminary simulations of R3. Again, the first phase of the quench propagation in terms of global and local voltage rise as well as He and jacket temperature is well captured. Concerning the voltage, its increase is slower than in the experiment, see figure 4.13. On the other hand, the temperatures agree better in this case than in L2 simulation, see figure 4.14. The integration of the conductor model in the circuit model will be pursued as well as the further investigations needed to improve the agreement. Nevertheless, this looks a good starting point and the mismatch between measured and computed results appears to be caused by similar factors in the two simulations analysed here, thus we expect to improve the quality of the results quickly and in all simulations.

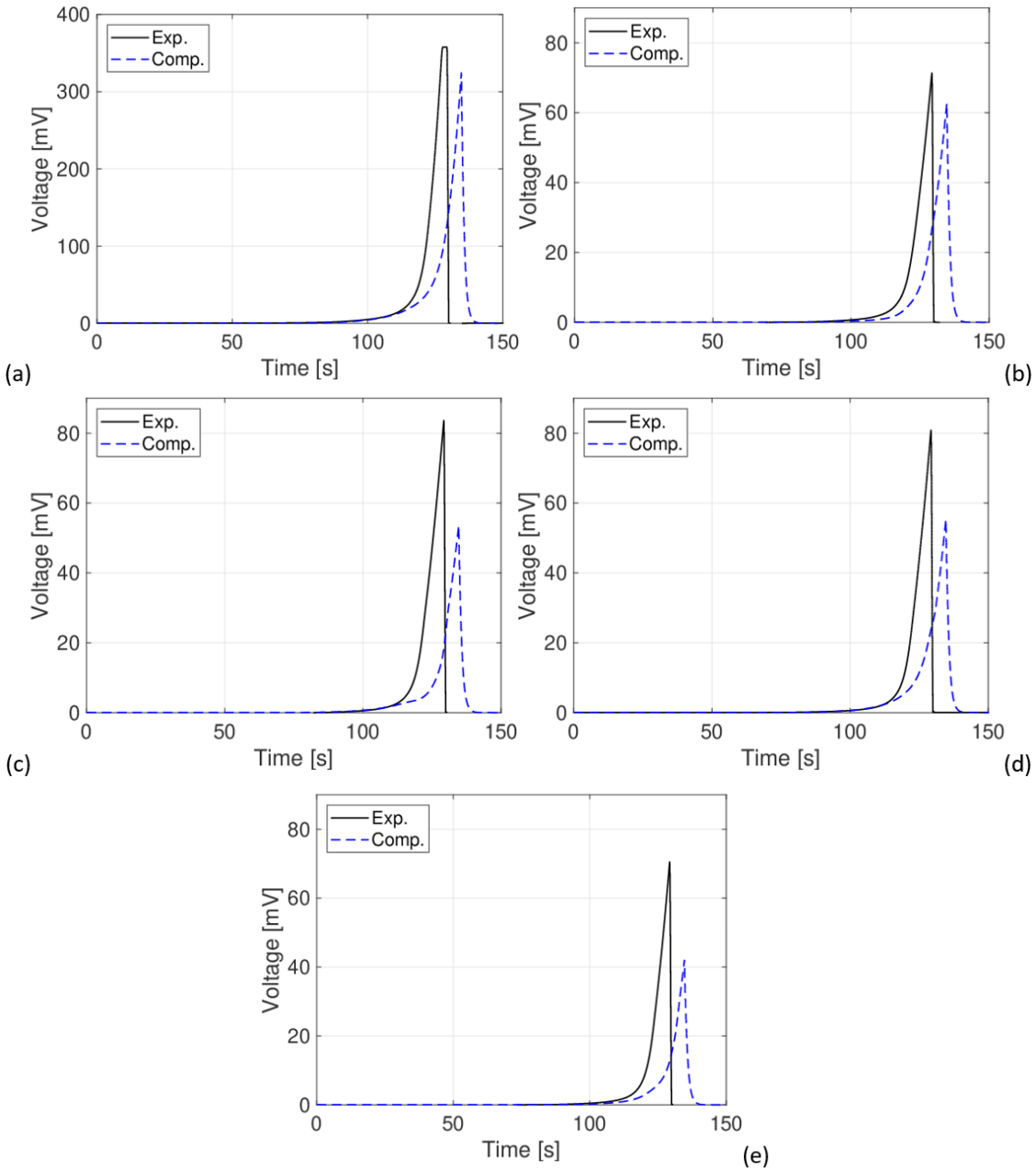

Figure 4.13: Evolution of measured and computed voltage across the entire conductor length (a), VH2-4-V6 (b), V6-V8 (c), V8-V10 (d), V10-VH4-4 (e).

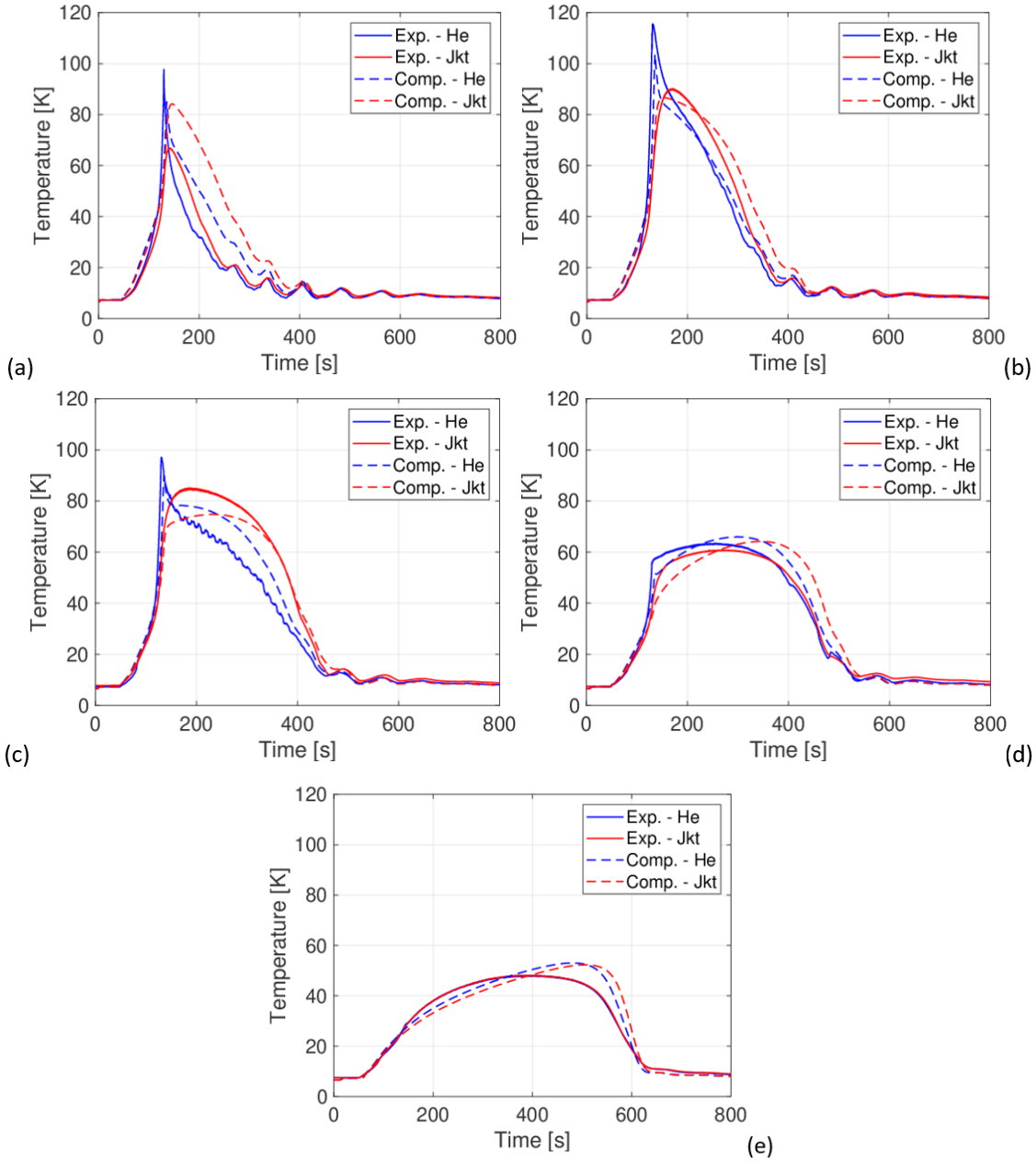

Figure 4.14: Evolution of the measured and computed temperatures at T4-1/2 (a), T6-1/2 (b), T8-1/2 (c), T10 - 1/2 (d) and T12-1/2 (e).

Chapter 5

Applications

5.1 CICCs

5.1.1 Slotted-core full conductor

5.1.1.1 Conductor Layout

In this section the most recent ENEA HTS CICC layout is described. An older version of the design is presented in [8], while the latest is analyzed in the following, see figure 5.1. It is constituted by an Aluminum core which features six twisted slots, with a twist pitch equal to 0.5 m. In each slot, 20 REBCO tapes are piled up without soldering. In order to hold them in position, an aluminum ”filler” is used on top of the stack. The cable is the inserted in a jacket for structural and/or coolant confinement purposes, which could be round (1.5 mm thick) or square. Here the round jacket option is investigated. The space available for the forced-flow of He is mainly the central channel, but also the portion of the slots that is left empty by the HTS stack. In this way, the He is in direct contact with the tapes, which is a unique feature with respect to other designs, such as those proposed by SPC and KIT.

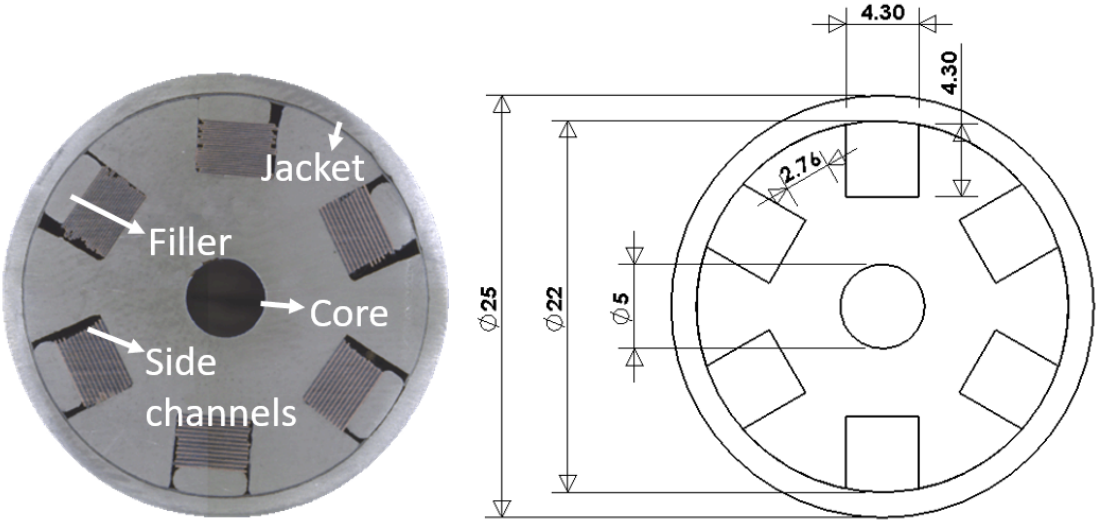

Figure 5.1: Picture of the HTS ENEA CICC. The sub-components of the conductor are indicated. The dimensions are shown in mm in the drawing.

This conductor is planned to be used as DTT CS insert coil [74] and it will likely be cooled using the same He that is circulated in the LTS magnets, thus at 6 bar and 4.5 K.

5.1.1.2 Preliminary analysis

The analysis performed for the KIT conductor to assess the time and space scales [45] has to be performed also for this new design, since they strongly differ for dimensions, material and cable layout. Thus, back of the envelope estimations are required for both fluid and solid, in order to assess whether the classical approach adopted for LTS could be suitable also for the ENEA HTS CICC.

Concerning the fluid and considering:

- $\sim$ 5 g/s mass flow rate, at the thermodynamic state mentioned previously
- an available cross-section for the He flow (summing the central channel and the side channels) $A_{He} = 27.4\ mm^2$
- a wetted perimeter $P_{wetted} = 57\ mm$

the resulting Peclet number Pe, which is defined as the ratio of the advective to the conductive heat transfer that takes place in the fluid ($v \times D_h/\alpha$), is equal to $\sim\ 10^5$. The speed used here is $\sim 2\ m/s$ and the hydraulic diameter is $D_h = 2\ mm$, computed as $D_h = 4{\times}A_{He}/P_{wetted}$. The thermal diffusivity α at 6 bar and 4.5 K is equal to $5{\cdot}10^{-8}\ m^2/s$ [60]. Since $Pe \gg 1$, the dominant mechanism for the heat transfer in the fluid is the advective one, thus the fluid can reliably be modelled with a 1D approximation along the conductor axis, which is the same approach adopted in LTS CICC modelling.

The same critical assessment must be performed on the solids, i.e. to check whether a single 1D region is suitable to model all the solids, as it is typically done for the strand bundle in LTS CICC. For the solids, the Biot number ($Bi = h \cdot L_c / k$) is used to estimate the entity of the gradients within the solids with respect to those between fluid and solid surface. Bi is computed using:

- a characteristic length L_c equal to 3 mm for the HTS stack or equal to the core radius (11 mm) for the slotted core
- a thermal conductivity k equal to $\sim$ 0.21 $W/m/K$ for the stack in the direction perpendicular to the tape plane [44] or equal to 190 $W/m/K$ for the aluminum core.

These values lead to $Bi > 1$ for both the HTS stack and the core. For comparison, following the same strategy for LTS, considering $L_c = 40$ mm and $k \sim 350$ $W/m/K$, a $Bi \sim 0.01$ is obtained, for which a 1D approximation of the strand bundle is justified. Therefore, being $Bi > 0.1$ for the HTS CICC under consideration, the adoption of a single 1D region to model all the stacks and the core is not reliable.

In previous works, attempts to model in a more detailed way this type of CICC have been proposed. For example, a 3D [75] electro-thermal or 2D + 1D thermal-hydraulic [76] models have been developed to simulate quench or heat slug propagation. However, since the final aim is to extend the conductor model to simulate an entire magnet wound with this conductor, one of the key features of the conductor model needs to be (up-)scalability. Therefore, adopting the same strategy proposed for the KIT conductor [45], the analysis of the thermal gradients within the conductor cross-section during the quench propagation should be performed with a detailed model, in order to have a more quantitative assessment and develop on that base an up-scalable model. To do this, a detailed electro-thermal model of the ENEA HTS CICC was developed, in order to model the temperature evolution *and* distribution during the transient. The detailed model features a 2D thermal model of the conductor cross-section coupled with a 0D electric model and it was implemented in STAR-CCM+ [57]. The thermal model solves the heat conduction equation in the conductor cross-section, see figure 5.2(a). The electric model solves a coupled set of non-linear algebraic equations, assuming no inductive effects, thus computing at each time-step the current in each current-carrying region, according to the schematic circuit reported in figure 5.2(b). The set of equations constituting the the electric model is as follows:

$$V = R_{Al} I_{Al} \tag{5.1}$$

$$V = V_C \left(\frac{I_{HTS,i}}{I_{C,i(B,T)}} \right)^n \tag{5.2}$$

$$I_{tot} = I_{Al} + \sum_{i=1}^{N_{stack}} I_{HTS,i} \tag{5.3}$$

where V is the voltage (per unit length), R_{Al} is the resistance of the aluminum core, I_{Al} is the current flowing in the core, V_C is the critical voltage, i.e., the critical electric field over a unit length, thus equal to 10^{-4} V, $I_{HTS,i}$ is the current in the i-th superconducting stack, $I_{C,i}(B,T)$ is the critical current of the i-th superconducting stack computed at magnetic field B and temperature T (the average stack temperature from the 2D thermal model is used), n is the stack n-value. I_{tot} is the imposed transport current. This electric model assumes that the redistribution of the current is much faster than the thermal time-scales, as already quantified in [42], thus inductive effects are neglected. As a first approximation, also the transverse electric resistance among the electrical regions (HTS stacks and core) is neglected.

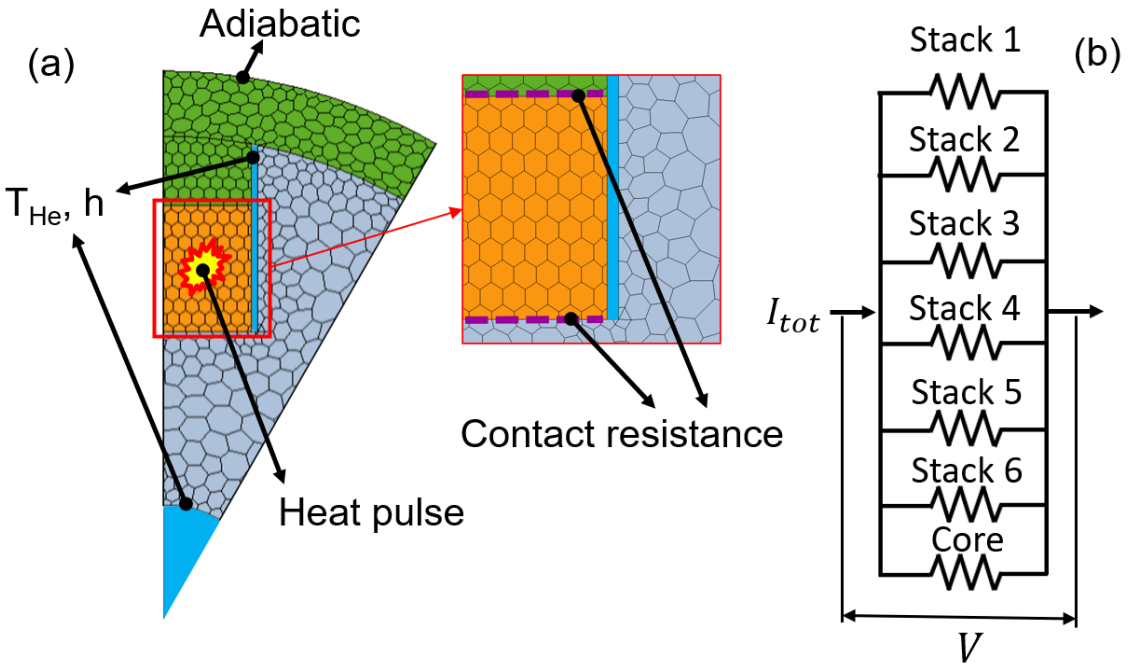

Figure 5.2: (a) 2D thermal model of the HTS ENEA CICC. The finite volume mesh is shown. The aluminum jacket and filler are shown in green, the HTS stack is colored in orange, the aluminum core is in light grey and the voids for the He are in light blue. The position where the contact resistances are considered are highlighted in the inset. The boundary conditions and the thermal driver are shown. (b) Scheme of the 0D electric circuit model, coupled with the 2D thermal model.

The thermal model simulates for symmetry just 1/12 of the conductor cross-section, assuming circumferential symmetry of the geometry, thermal driver and boundary conditions. Indeed, the thermal driver is supposed to be a heat pulse occurring in all the stacks. This mimics the inductive heating which is typical of quench experiments on LTS CICCs [70]. The heat pulse is the smallest possible to induce the quench and it resulted in 1500 J/m (considering a constant power deposited for 0.1 s). The transient is

simulated for 0.5 s after the end of the heat pulse. This is because the aim of the model is to quantify the temperature difference within the cross-section, which is expected to be large in the first part of the transient. Furthermore, the model cannot account for current discharge, since it would require the quantification of the voltage *along* the quenched region. Simulating the first part of the transient it is reasonable to assume a constant transport current. Nevertheless, after the external heat deposition, the current redistributes according to the current model, which computes also the deposited heat due to Joule effect and it feeds this information back to the thermal model. The boundary conditions of the thermal model are the following:

- adiabatic external jacket surface
- Robin-type boundary conditions at the interface with the fluid ($T_{He} = 4.5\ K$, $h = 2000\ W/m^2/K$ for the central hole computed from the Dittus-Boelter correlation [60] and $h = 15000\ W/m^2/K$ for the side channels of each slot from the ad-hoc correlation described in the next paragraph 5.1.1.3).

The results of the detailed model, see figure 5.3(a)-(b), show that temperature differences in the cross-section of the conductor can arise and they can be as high as 50 K. The most severe temperature gradients are concentrated in the HTS stack, since there the heat deposition due to Joule effect is strong *and* they have an anisotropic thermal conductivity, which is particularly low in the direction perpendicular to the tape plane.

The grid independence of the results shown in this section is ensured by a dedicated study in the case of uniform heating, see figure 5.4. The relative error on the temperature increase in both the core and the HTS stack has been computed as function of the characteristic grid size, which is in turn defined as $\sqrt[3]{V_i/N_i}$, where V_i is the volume of the i-th region and N_i the corresponding number of control volumes. The reference value with respect to which the error has been computed was obtained with the Richardson extrapolation [77].

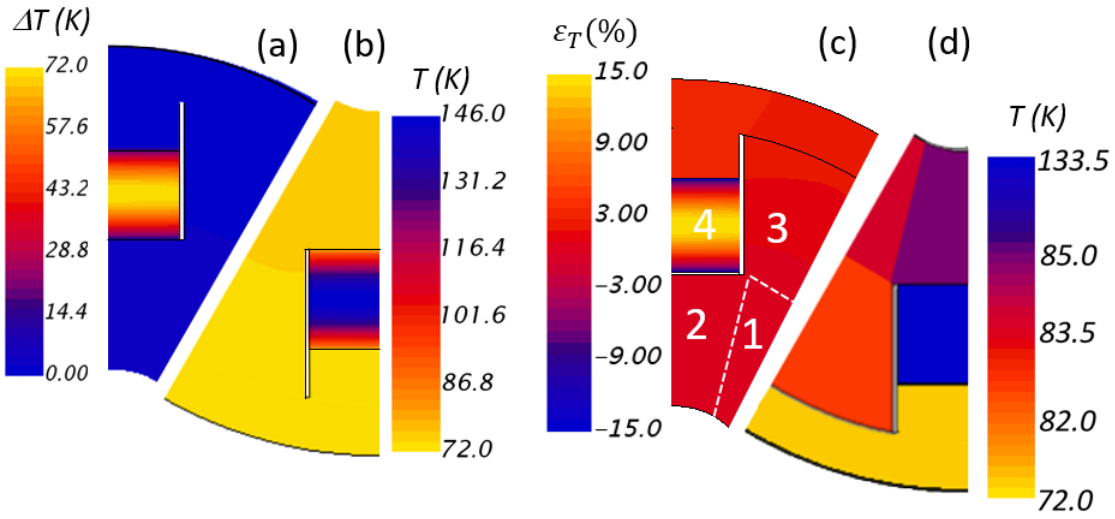

Figure 5.3: 2D distribution of the temperature increase with respect to the core temperature (a), temperature of the cross-section (b), non-dimensional difference of the local to average temperature (c) and average temperature of the conductor sub-regions (d). The distributions are shown after 0.5 s from the end of the heat pulse. The sub-regions adopted in the 1D model are shown and numbered in (c).

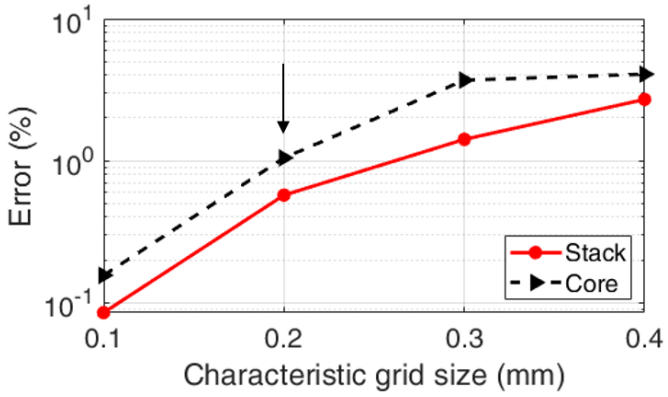

Figure 5.4: Grid independence analysis of the 2D thermal model, focused on the temperature of the HTS stack and core. The arrow indicates the characteristic size used for the analysis.

According to the results obtained with detailed cross-sectional model, it is possible to identify sub-portions of the cross-section in which the normalized temperature difference ϵ_T computed according to Equation 5.4 is below a certain threshold.

$$\epsilon_T = \frac{T - T_{ave}}{T_{ave} - T_0} \tag{5.4}$$

Given that the aim of the present model is to analyze trends parametrically varying different parameters rather than the most accurate estimation of, e.g., the temperature in a particular point of the conductor, an $\epsilon_T \lesssim 15\%$ was considered as acceptable. On top of this, a different number of sub-portions of the core could satisfy the criterion. Therefore, the effect of the variation of the number of regions in the core on the computed peak temperature in the stack has been studied, see table 5.1. As a result, a total number of regions in the core equal to 18 has been chosen. Considering that one region for each stack was adopted and that the fillers were assumed to be in perfect contact with the jacket, thus assigning one thermal (and electric) region to the jacket + fillers, a total number of 18 + 6 + 1 = 25 regions were used to discretized the conductor cross-section. The resulting multi-1D region model is still up-scalable to the magnet level, since the key feature is to still be a set of 1D regions that keeps the model scalable.

Table 5.1: Grid independence analysis on the number of 1D regions used for the discretization of the core

Number of regions in the core	$T_{peak,stacks}$ (K)
6	162.3
18	133.2
30	130.4
36	129.8

5.1.1.3 1D CICC model and conductor characterization

The set of PDEs solved is reported below.

$$(\rho c_p A)_i \frac{\partial T_i}{\partial t} - \frac{\partial}{\partial x}\left[(kA)_i \frac{\partial T_i}{\partial x}\right] = q'_{i\leftrightarrow solids} + q'_{i\leftrightarrow j} + q'_i \tag{5.5}$$

$$\frac{\partial v_j}{\partial t} + v_j \frac{\partial v_j}{\partial x} + \frac{1}{\rho_j}\frac{\partial pj}{\partial x} + 2 f_j v_j \frac{|v_j|}{D_{h,j}} = 0 \tag{5.6a}$$

$$\frac{\partial p_t}{\partial t} + v_j \frac{\partial p_j}{\partial x} + (\rho c^2)_j \frac{\partial v_j}{\partial x} - 2(\phi \rho f v^2)_j = \frac{\phi_j}{A_j} q'_{j\leftrightarrow i} \tag{5.6b}$$

$$\frac{\partial T_j}{\partial t} + v_j \frac{\partial T_j}{\partial x} + \phi_j T_j \frac{\partial v_j}{\partial x} - 2(f v^2)_j \frac{|v_j|}{(c_v D_h j)} = \frac{q'}{(c_v \rho A)_j} \tag{5.6c}$$

$$\left(\overline{\overline{G}}\,\overline{\overline{L}}\right)\frac{\partial I_m}{\partial t} + \frac{\partial^2 I_m}{\partial x^2} + \left(\overline{\overline{G}}\,\overline{\overline{R}}\right)_m \cdot I_m = 0 \tag{5.7}$$

where in Equation 5.5 to 5.7 i, j and m are the solid (thermal), fluid and electric regions, respectively, ρ is the density of the solid material or that of the fluid, c_p is the specific heat of the solid or of the fluid, T is the solid or fluid temperature, k is the thermal conductivity of the material considered, A the cross-section of the region, q'_i is the external power deposition per unit length, $q'_{i\leftrightarrow solids}$ is the power per unit length transferred from/to region i from/to other solid regions, $q'_{i\leftrightarrow j}$ is the power per unit length transferred between the solid region i and fluid region j. In Equations from 5.6a to 5.6c, v, p and T are the fluid speed, pressure and temperature, respectively; f is the friction factor, c the speed of sound in the fluid, Φ is the Gruneisen parameter, D_h is the hydraulic diameter, c_v is the specific heat at constant volume. In Equation 5.7, $\overline{\overline{G}}$ is the matrix of the transverse electrical conductance per unit length, $\overline{\overline{L}}$ is the matrix of the inductances and $\overline{\overline{R}}$ is the matrix of the resistances per unit length of the electric region considered (indeed, it is a diagonal matrix) and I is the current in each electric region.

The interfaces among solid (thermal), fluid and electric regions are modelled as follows:

1. $q'_{i\leftrightarrow j}$ in 5.5, 5.6b and 5.6c is equal to $Ph(T_i - T_j)$ where P is the wetted perimeter, h is the heat transfer coefficient, T_i and T_j are the temperatures of the solid and fluid regions, respectively.

2. $q'_{i\leftrightarrow solids}$ in 5.5 is equal to $(UA')_{i\leftrightarrow k}(T_i - T_k)$, where U is the inverse of the thermal contact resistance, A' is the heat transfer area per unit length, T_i is the temperature of the i-th solid region considered and T_k the temperature of the k-th surrounding solid region in contact with the i-th one, thus with $k = 1, ..., i-1, i+1, ..., N$. The thermal contact resistances are taken:

   (a) for HTS stack (copper) to core (aluminum) from [78]

   (b) for adjacent core (aluminum) regions it has been computed as δ/k, where k is the aluminum thermal conductivity and $\delta = 0.1\ mm$ and it is assumed to have no thermal capacity

3. the elements in $\overline{\overline{G}}$ are obtained as follows:

   (a) between core sub-regions: here the transverse conductance is assumed to be very large

   (b) between HTS stack and core: from dedicated experiments described in section 5.1.2.2.

The heat transfer coefficient and friction factor of the side channels have been computed through a dedicated Computational Fluid Dynamics analysis, based on the approach used, e.g., in [79]. This analysis was driven by the absence of experimental data

on this type of geometry and reliable literature value, since the geometry is a rectangular shaped and twisted duct, see figure 5.5. The resulting correlations as a function of the Reynolds number are reported in table 5.2. The correlations have been obtained best-fitting the computed values as shown in figure 5.6. For all the simulations, the He thermodynamic state is set at 4.5 K and 6 bar.

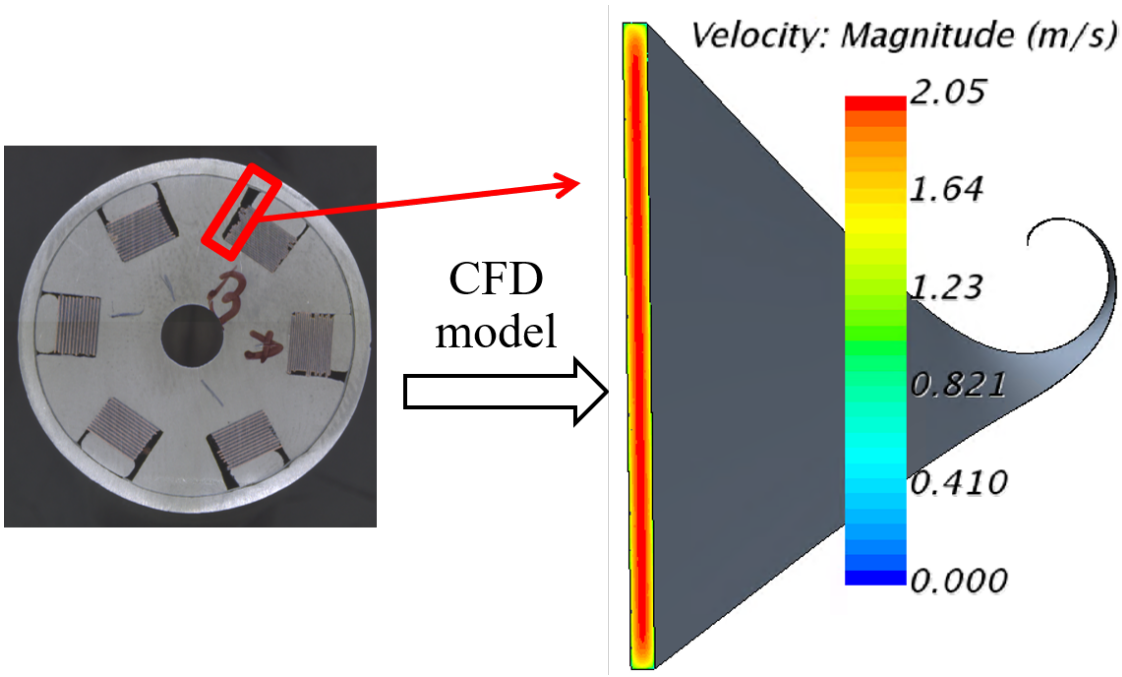

Figure 5.5: 3D Computational Fluid Dynamics model of the (twisted) sub-channel of the HTS ENEA CICC. The 2D distribution of the velocity is als shown.

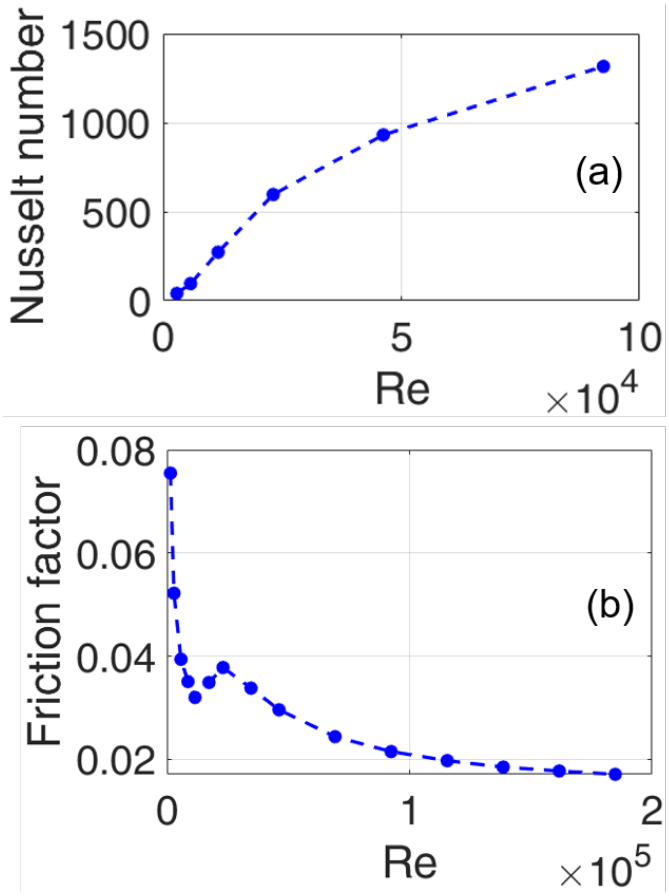

Figure 5.6: (a) Nusselt number and (b) friction factor as function of the Reynolds number. The dots are the points computed from the CFD model.

5.1.1.4 Simulation setup

The boundary conditions and constitutive relations adopted for the 1D CICC model are listed in table 5.2. Also the operating conditions (current and magnetic field) expected for the DTT Central Solenoid Insert Coil are reported.

The transient (quench) is induced by a heat pulse with a duration of 0.1 s over 10 cm and amplitude slightly above the minimum quench energy. The total energy deposited is 150 J and it corresponds to that used in the 2D detailed model, see section 5.1.1.2.

The quench is detected when the total voltage overcomes 100 mV. After the quench detection, the quench protection system awaits a so-called delay time (τ_{del}) before discharging the current from the coil. The current is then discharged exponentially with a characteristic time equal to τ_{dis}, see again 5.2.

The mesh of the 1D domains is built according to an adaptive algorithm which refines the mesh at each time step close to the quench fronts, see section 3 for more

details. This strategy was also used and validated in the LTS quench simulations performed with the 4C code [70]. The minimum mesh size is set to 1 mm. Also the time step is adaptive and it ranges from a minimum of 0.1 ms to a maximum of 1 ms. With this setup.

Table 5.2: Operating conditions of the HTS ENEA CICC. Boundary conditions and constitutive relations used in the 1D analysis.

Parameter	Value
Length (m)	132
Current (kA)	32.1
Inlet/Outlet pressure (bar)	6/5
Inlet temperature (K)	4.5
Voltage at conductor end (V)	0
t_{delay} (s)	0.25
$\tau_{discharge}$ (s)	0.5
P_{wetted} (cm)	6.7
$f_{central\ channel}$	Colebrook correlation [60]
$f_{side\ channels}$	$2.21 \cdot Re^{-0.4}$ ($Re > 10^4$)
$Nu_{central\ channel}$	Dittus-Boelter correlation [60]
$Nu_{side\ channels}$	$0.42 \cdot Re^{0.71}$

5.1.1.5 Results

In this section, the most relevant results of the 1D model are presented and discussed.

Peak temperature The evolution of the peak temperature in the different regions simulated is reported in figure 5.7. The temperature of the HTS stacks increases more and faster than the core sub-regions, simply because heat is being deposited there first. The multi-1D region allows having a quantification of the temperature differences within the conductor cross-section during the quench propagation. Indeed, the differences can reach up to 50 K between the stacks and the core. The impact of these large temperature differences, which are not encountered in, e.g., LTS CICCs, should be investigated from the thermo-mechanical point of view. Furthermore, the peak temperature reaches 130 K ($\pm$ 20 K). Also concerning the design criterion of the maximum hot-spot temperature to be reached during a quench, the only available reference is that for LTS in, e.g., ITER, which is set equal to 150 K. Nevertheless, this does not necessarily extends also to HTS CICC.

It is worth noticing that the maximum temperature computed with the 1D model is higher than that with the 2D thermal + 0D electric model. This is mainly caused by the

He boundary conditions considered in the 2D model, which assumes a He temperature constant and equal to 4.5 K, while in the 1D model the He temperature increase is taken into account.

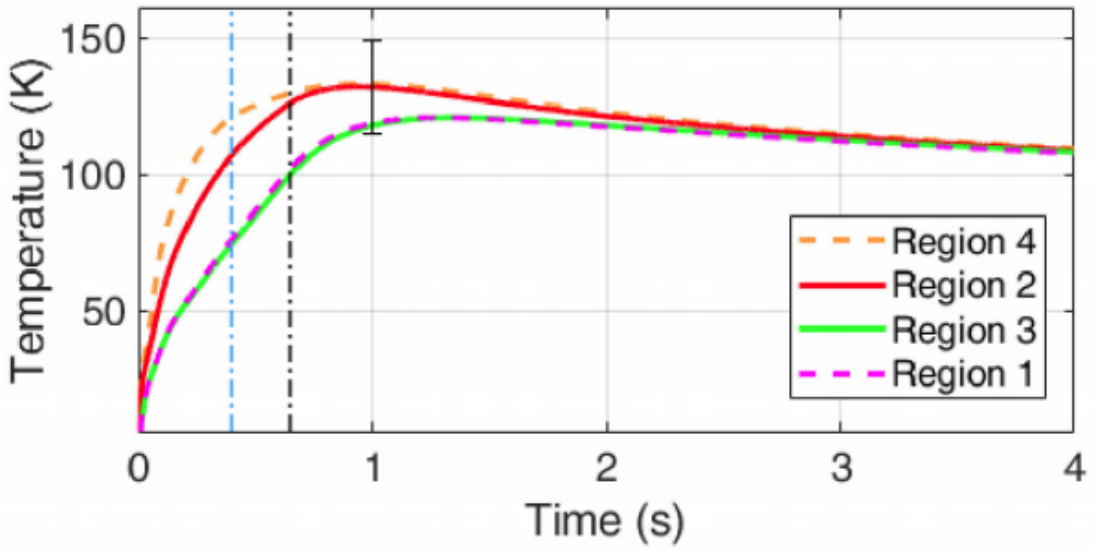

Figure 5.7: Temperature evolution in the four sub-regions of the HTS ENEA CICC during quench, computed with the 1D model. The numbering of the regions refers to figure 5.3. The cyan and black dashed dotted lines identify the quench detection and the start of the current discharge, respectively. The ±15% error-bar shows the uncertainty found in the detailed analysis.

Current evolution The evolution of the current throughout the transient is shown in figure 5.8. Before the current dump, the current manages to flow from the HTS stacks to the aluminum core. This is because the core resistance increases less than that of the stacks. This means that the inter-slot resistance (which is dominated by the contact resistance between stack and core) is sufficiently low to ensure a fast redistribution of the current, which contributes to reach manageable peak temperatures. In addition, once the current is mainly flowing through the core, the heat removal capability is improved, since the heat is generated closer to the heat sink, which is almost entirely located in the central channel. Actually, this helps on longer time scales, e.g., for the conductor re-cooling once the flow is re-established.

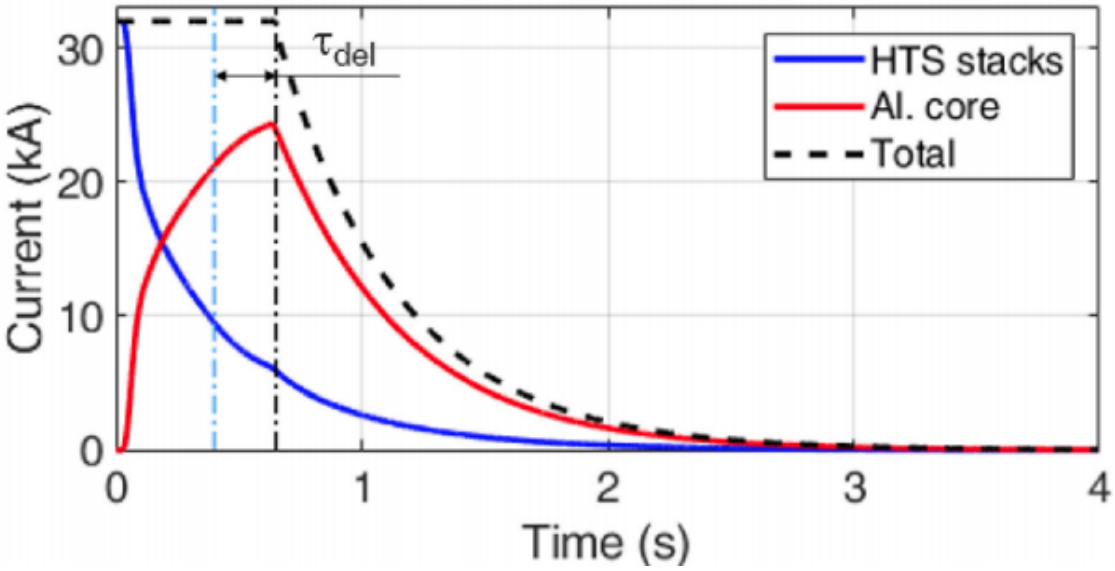

Figure 5.8: Current evolution in all the HTS stacks and in the core. The cyan and black lines identify the quench detection and current discharge instants, respectively.

Parametric analysis Fundamental parameters of magnet protection are the discharge time constant, $\tau_{discharge}$, and the delay time, t_{delay}, already discussed before in section 5.1.1.4. Indeed, these parameters for the DTT CS Insert Coil are still under discussion, while they have been fixed for the CS protection to $\tau_{discharge} = 4\ s$ and $t_{delay} = 2\ s$.

These values have been adopted also in a simulation of the quench of the HTS Insert Coil. It has been reported in figure 5.9 the peak temperature reached with that couple of parameters, which is clearly unacceptable. Therefore, since both parameters can, to some extent, be varied in the protection system tuning, they have been scanned parametrically. It is clear that the delay time has a strong impact on the peak temperature and it needs to be decreased to less than 0.5 s to have a peak temperature below 300 K. This should limit the risk of damaging the tapes because of, e.g., delamination. Also, a further decrease of the peak temperature can be obtained reducing the discharge time constant from 4 s to 0.5 s. However, this solution would go also in the direction of increasing the inductive voltage and AC losses, thus it should be considered as a second option with respect to reducing the delay time. Further analyses should be performed once the AC losses are quantified more reliably, perhaps through electromagnetic models and/or experiments.

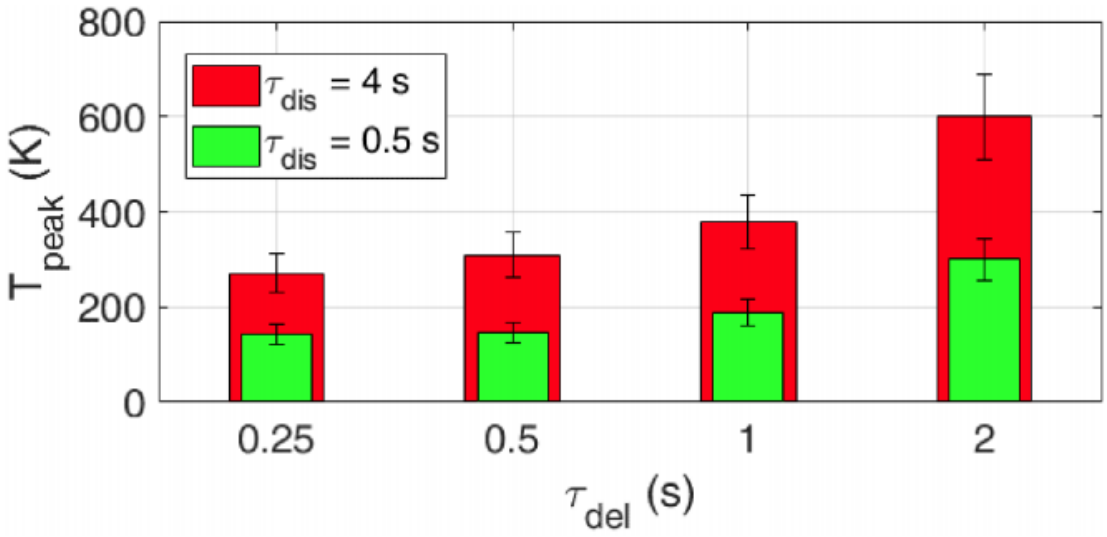

Figure 5.9: Parametric study on the delay (τ_{del}) and discharge (τ_{dis}) times on the hotspot temperature reached in the stacks during the quench evolution.

5.1.2 Slotted-core subsized conductors

5.1.2.1 The ENEA Samples

The HTS samples proposed by ENEA to be tested in SULTAN [80] are sketched in figure 5.10. The operating conditions foreseen in the tests are summarized in table 5.3. The samples are all straight, even though the design of the real conductor is twisted to reduce AC losses. This choice was made to greatly simplify the manufacturing process of the samples as well as to place more easily the diagnostics needed for the tests. They are equipped with $\sim$ 80 tapes, in contrast to the 120 foreseen in the full conductor. This reduction was driven by the maximum current which can be supplied by the SULTAN power supply, i.e. 15 kA; the full conductor would be able to carry 30 kA, but in this way it would be very hard to induce a quench in the testing conditions foreseen in SULTAN as it would have had a too large temperature margin. Reducing the number of tapes, the critical current in the maximum field region should be of the order of the maximum current supplied by the SULTAN power supply at 4.5 K.

The three samples analyzed here differ for orientation and distribution of the tapes in the slots. Sample C1 and C2 differ for the tape orientation with respect to the magnetic field direction, see again figure 5.10. C3 has a different number of tapes per slot with respect to the first two, see table 5.4. These differences cause different performance in terms of T_{CS} of each sample. Indeed, the tapes that are normal to the direction of the magnetic field have the lowest T_{CS}, i.e. in slots A and D of samples C1 and C3, see figure 5.10. C3 has less tapes than the other two samples (78 in C3 and 80 in C1 and C2), thus the current per tape is slightly higher, thus the T_{CS} is slightly lower than in C1 (in which the tapes have the same orientation of C3). C2 has the tapes oriented in

the same way, thus it is characterized by a unique value of the T_{CS}. On the other hand, C1 and C3 have tapes that are normal to the magnetic field and others whose normal has an angle of 60° with respect to the magnetic field direction, thus leading to a much larger T_{CS}, see table 5.4.

The samples will be cooled with supercritical He and it will flow in the central hole of the aluminum core, see figure 5.10. An external stainless steel jacket will be put around the aluminum jacket to ensure leak tightness. The quench is planned to be initiated increasing the He inlet temperature thanks to an external heater or through an AC pulse induced by an external fast-varying magnetic field.

Table 5.3: Operating conditions in SULTAN.

Parameter	Value
Current (kA)	15
Magnetic field (T)	10.9
He inlet temperature (K)	4.5
Maximum He inlet temperature (K)	15
He pressure at conductor inlet (bar)	6
He mass flow rate at conductor inlet (g/s)	5
$\tau_{discharge}$ (s)	0.1
t_{delay} (s)	0.5

Table 5.4: Features of the three samples.

C1: tapes in each slot	20
C2: tapes in each slot	20
C3: tapes in each slot	13
C1: T_{CS} (K)	8.8, 20.9
C2: T_{CS} (K)	11.6
C3: T_{CS} (K)	8.0, 20.1

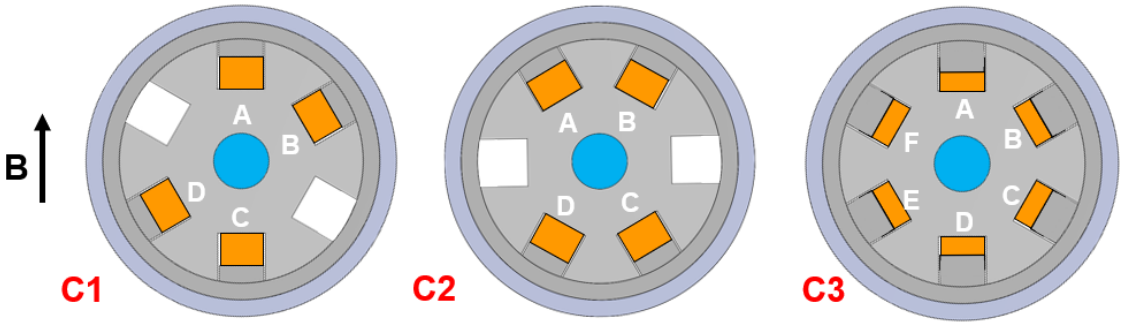

Figure 5.10: Sketch of the three configurations designed for the SULTAN tests. The color code is as follows: the orange regions are the HTS stacks, the grey regions are the aluminum core, filler and jacket, the light purple region is the external stainless steel jacket, the white regions, if any, are empty slots and the light blue regions is where He flows. The direction of the magnetic field is also shown.

5.1.2.2 Electric characterization of the CICC

Important interface parameters in the electric model of the H4C are the contact (electric) resistances among different current carrying regions. For this reason, an experimental characterization of the ENEA CICC was performed at ENEA Frascati.

A 50 cm long sample was tested electrically in a liquid nitrogen bath. In order to measure the contact resistance between tapes in the same slot or between tapes in different slots, the following procedure was adopted.

Each tape was exposed at the samples ends, see figure 5.11(a). In this way, selected tapes could be connected to the bus-bars. For example, to measure the electric contact resistance between two adjacent tapes in the same slot, one tape, say B1 (see figure 5.11(b), end was connected to a bus-bar and the adjacent tape, B2, was connected to the other bus-bar at the end located at the opposite side of the sample. In this way, the current is forced to flow from B1 to B2. Varying the current value and measuring the voltage was then possible to extract the electric resistance, see figure 5.11(c). Depending on the level of discretization of the HTS stack, it is possible to input to the model each measured value of contact resistance (which is supposed to be uniform along the sample length). It can be noticed that the inter-tape resistance is quite uniform within the slot, except for the first two tapes, between which the contact resistance in clearly smaller than the other couples considered in the experiment. This is probably due to the larger pressure present at the bottom of the slot, leading to a better electrical contact with the core.

The inter-slot resistance was also measured. This was achieved connecting to one bus-bar a tape of one slot and a tape of the other slot to the other bus-bar. In order to assess the impact on the contact resistance of the different position of the tape in one slot, this measure was performed keeping fixed one tape (A20) from one stack for all tests while the other bus-bar was connected to one tape of another stack, scanning all

the tapes of that stack, i.e. from B1 to B18, in subsequent tests, see again figure 5.11(c). In this way, the constant contribution is given by the (double) contact resistance of the bottom tapes with the aluminum core and by the resistance of the aluminum core itself, that is the inter-slot resistance. On top of this, it is clearly visible the impact of the piling up of the tapes within the slots, since the resistance going from A20-B18 to A20-B1 gradually increases, as more and more tapes are placed between A20 and the other tape in slot B.

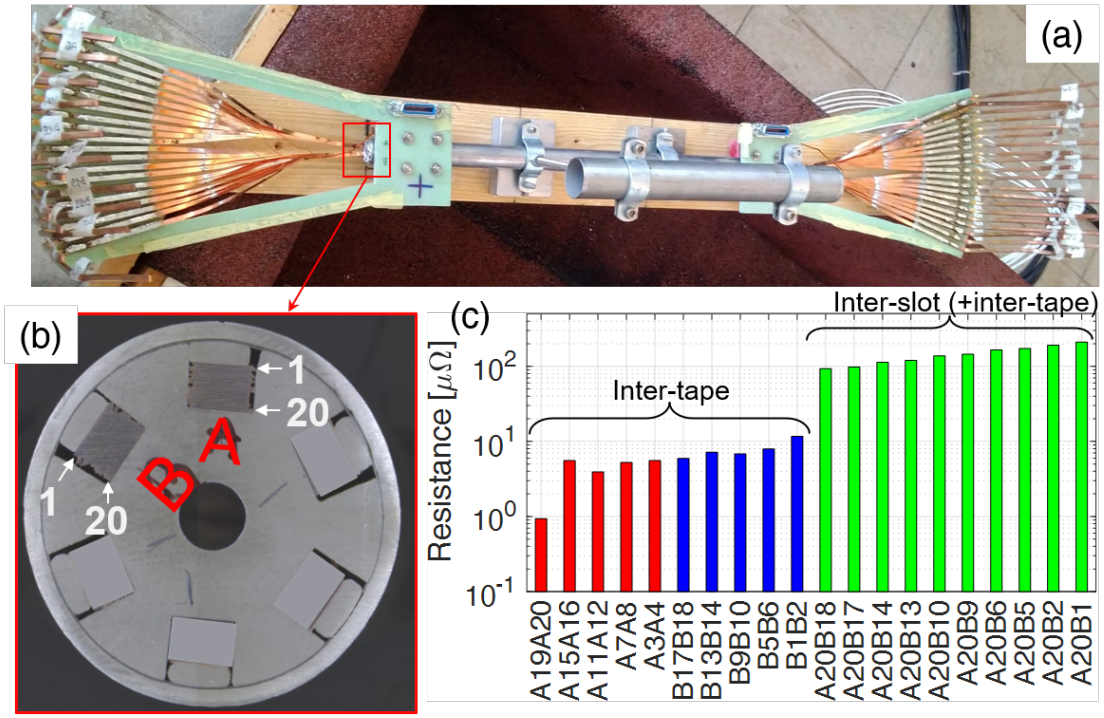

Figure 5.11: Photograph of the sample electrically tested in Frascati (a) and its cross-section (b). Numbering of the tapes is also shown. Data measured for inter-tape and inter-slot electric resistance (c).

5.1.2.3 H4C model

The H4C code [81] was here employed to simulate the quench initiation and propagation within the ENEA HTS samples. A key point of the modelling of fast transients in HTS conductors is the discretization of the cross-section, as discussed in [81] and in Section 2.2.1. The detailed cross-section analysis of the ENEA conductor, using an electro-thermal model, is presented in [48] and in Section 5.1.1.2. It was shown that, lumping the entire slot in just one thermal and electric region could lead to an error on the temperature increase of up to 15 %. Therefore, in this analysis, a finer discretization (to be implemented in H4C) of the conductor cross-section was adopted. This leads to

a more accurate description of key quantities such as the hotspot temperature, since it is expected to be reached within the HTS stack itself, as well as a closer insight on the evolution of the current *within* the stack itself. The cost of this finer discretization is an increase of the 1D regions by roughly one order of magnitude with respect to the model used in [48]. Indeed, assigning one thermal and one electric region to each tape, the total number of 1D regions modelled rises to $\sim$ 80, depending on the number of tapes of the sample modelled. Nevertheless, the computational time required for such an analysis is still acceptable, i.e. few hours. The He flow is modelled with just one fluid region, since it is expected to flow only in the central hole. The friction factor correlation adopted in this case is the Petukhov correlation [60].

The interfaces between different regions of the same type and between regions of different types are modelled as follows:

- Electric contact resistances
  - Tape to tape: values taken from the measurements described in Section 5.1.2.2 (on average, 5 $\mu\Omega/m$);
  - Tape to core: values taken from the measurements described in Section 5.1.2.2 (on average, 50 $\mu\Omega/m$);
- Thermal contact resistances
  - Tape to tape, i.e. copper to copper, taken from [82], set constant and uniformly equal to 0.5 m^2K/W;
  - Tape to core, i.e. copper to aluminum, taken from [78], set constant and uniformly equal to 0.6 m^2K/W;
- Heat transfer coefficient
  - He to core: Dittus-Boelter correlation taken from [60].

The superconductor scaling law is taken from [58] and the dependence of the J_C on the tape orientation is accounted for considering the Ginzburg-Landau law [73].

The inductances between the current carrying elements have been computed using the (mutual) inductance definition:

$$M_{12} = \frac{\mu_0}{4\pi S_1 S_2} \int_{V1} \int_{V2} \frac{1}{r_{12}} dV_1 dV_2 \tag{5.8}$$

where μ_0 is the permeability of the vacuum, S_1 and S_2 are the cross-section of the two tapes considered, V_1 and V_2 are their volumes and r_{12} is the distance between the infinitesimal volumes dV_1 and dV_2. Equation 5.8 has been solved numerically using a Matlab script and the procedure was benchmarked against the solution shown in [83].

The inductance of the core would have required more expensive calculations and, above all, its contribution is expected to be marginal on the (very short) time scales of interest here. The reason is that, due to its high electric resistance (higher than the copper and the HTS while transitioning to normal state) the current will preferably redistribute among the tapes and their copper stabilizer rather than in the core itself.

The values of inductance between the tapes (in the C1 configuration) are the following:

- from 4.9 μH (self) to 3.9 μH, within the same slot
- $3.6 - 3.2$ μH between tapes in slots A and B
- $3.1 - 2.8$ μH between tapes in slots A and C
- $3.3 - 3.0$ μH between tapes in slots A and D

The values computed in configurations C2 and C3 are very similar to those reported above.

The boundary conditions adopted for this analysis are the following:

- heat conduction equation
  - adiabatic conductor ends
- fluid equations
  - imposed (constant) outlet and inlet pressure
  - imposed (variable in time) inlet temperature
- current equation
  - imposed (variable in time) current (larger than zero in each tape, equal to zero in the core and in the jacket) on the outlet side
  - imposed zero current gradient (zero voltage) at the inlet side

The initial conditions used are the following:

- solid and fluid temperatures: uniform and equal to the initial inlet He temperature (4.5 K)
- fluid speed: uniform and compliant with the imposed pressure drop
- fluid pressure: linear from inlet to outlet pressure
- current: uniform and equal to the total current divided by the total number of tapes in each superconducting region and equal to zero in the resistive regions

The quench detection threshold is set to 100 mV and the current is dumped according to the characteristic time reported in table 5.3.

5.1.2.4 Results

In this section, the results of the quench simulations are presented. First, a detailed discussion on the current and temperature evolution and distribution in the configuration C1 is carried out. Then, the comparison of the quench propagation in the three configurations is discussed.

Quench propagation in C1

Current evolution The current evolution in the tapes of the slots A and B of configuration C1 is shown in figure 5.12. Recall that the quench is induced heating the conductor through warm He flowing in the central channel. Therefore, the temperature starts increasing (equally) in the tapes at the bottom of all the slots. Recall also that the different orientation of the tapes in slots A and B leads to very different current sharing temperatures.

According to the heating coming from the lower part of the slot, the current in the bottom tapes starts decreasing and it is transferred to the tapes at the top of the slot, since they are still cold. This happens first in slot A because it has a lower T_{CS} and the current redistribution starts at t = 0.8 s, see figure 5.12(b). After few hundredths of seconds, the top tapes have slightly more current than the nominal (initial) one. However, at t = 0.87 s, the current sharing between the superconducting layers and the tape stabilizers starts to be visible, see the dashed curves in figure 5.12(a). As soon as the current sharing within the tapes starts, the current further redistribute among the slots. Indeed, in figure 5.12(b) it is visible that, first, the top tapes host more current than the bottom ones, but then the current starts flowing away from the slots, thus passing from the top tapes to the bottom ones, as highlighted after t = 0.9 s in figure 5.12(b).

The current in slot A, in fact, starts decreasing, see figure 5.12(a) and it is shared between the aluminum core and slot B, see the black curves in figure 5.12(c). More in detail, part of the current from slot A penetrates in slot B from the bottom. However, also those tapes are heating up and the current approaches the critical current in the bottom tapes, thus they share part of their current with the top tapes of slot B, see the blue curves in figure 5.12(c). Note that the tapes reach roughly 250 A, while the steady state value is around 180 A. As the entire slot B is heating up, also here the current starts flowing away from the stack into the aluminum core. Meanwhile, slot A has become normal after t = 1.1 s, since the current in the superconducting portion of its tapes reaches zero, see the red-to-yellow curves in figure 5.12(c). At this point, the aluminum core becomes the most relevant current carrying element, until the current is discharged.

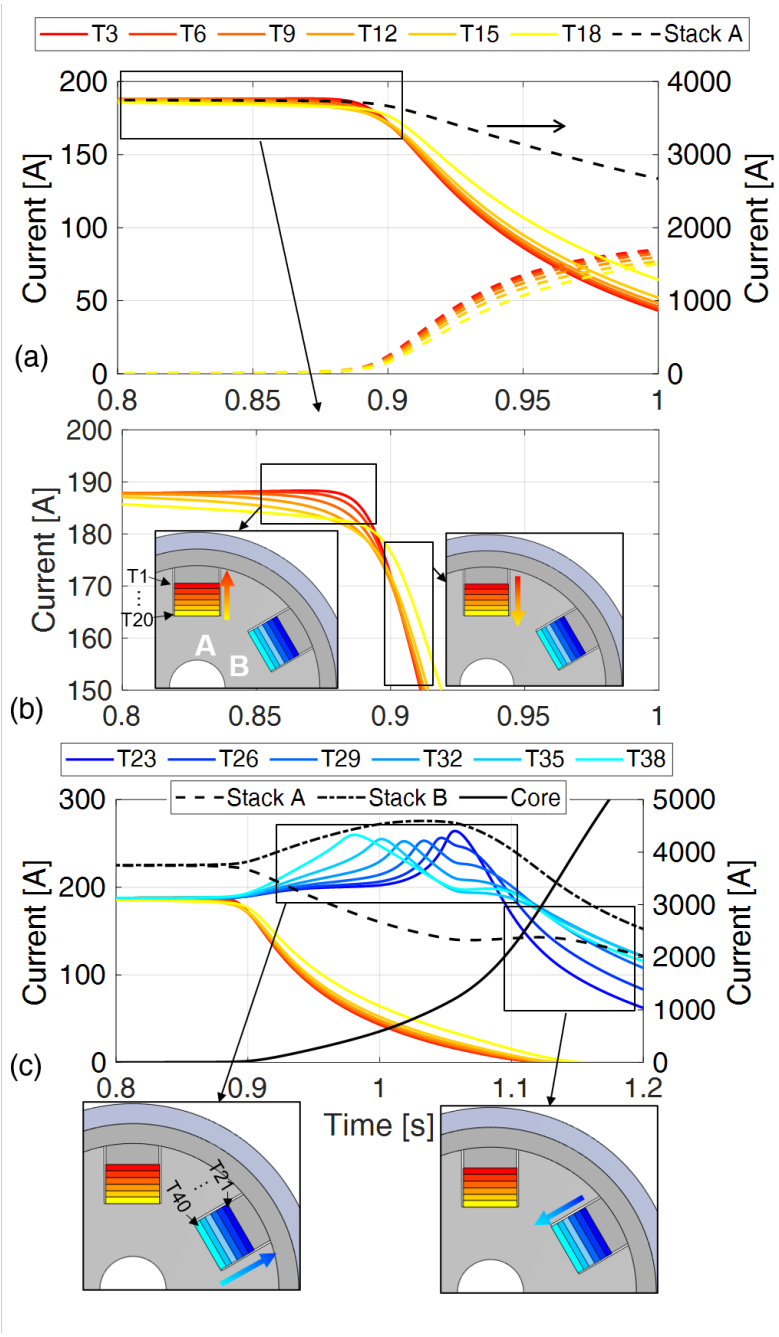

Figure 5.12: Current evolution in the superconductor (solid lines) and copper (dashed lines) of selected tapes (a). The evolution of the total current in stack A is also shown on the right axis. Zoom of the current evolution in the superconductor of selected tapes. The qualitative paths and trends in the cross section are also sketched (b). Evolution of the current in the superconductor of selected tapes in stack A and B (c). The total current flowing in the stacks is shown on the right axis with black dashed lines.

Temperature evolution The evolution of the temperature in the tapes of slots A and B is shown in figure 5.13. During the quench initiation, the temperature rise in the tapes is driven by the current flowing in the stabilizer of the tapes themselves. This is the reason for which the temperature of the top tapes rises before that of the bottom tapes, even though the heating provided by the warm helium comes from the central channel. As already shown in figure 5.12(a), slightly more current is present in the stabilizer of the top tapes of slot A (and also, later, of slot B). Thus a stronger heating is generated in the top part of slot A. Concerning slot B, between t = 0.98 s and t = 1.07 s, the temperature rises first in the bottom tapes, since here more current - part of which coming from slot A - is flowing (also in the stabilizer). After t = 1.07 s, however, a similar phenomenon to that discussed for slot A happens also and more evidently in slot B: a larger amount of current is ”trapped” in the top part of the slot, thus more current flows in the stabilizer and the temperature increases more there. Note that a temperature difference of about 20-30 K is present after t = 1.1 s, *within* the stack in slot B, confirming that large temperature difference within a stack can arise during the quench evolution.

Note also that, for symmetry, the same considerations discussed for slots A and B are valid here for slots C and D, respectively.

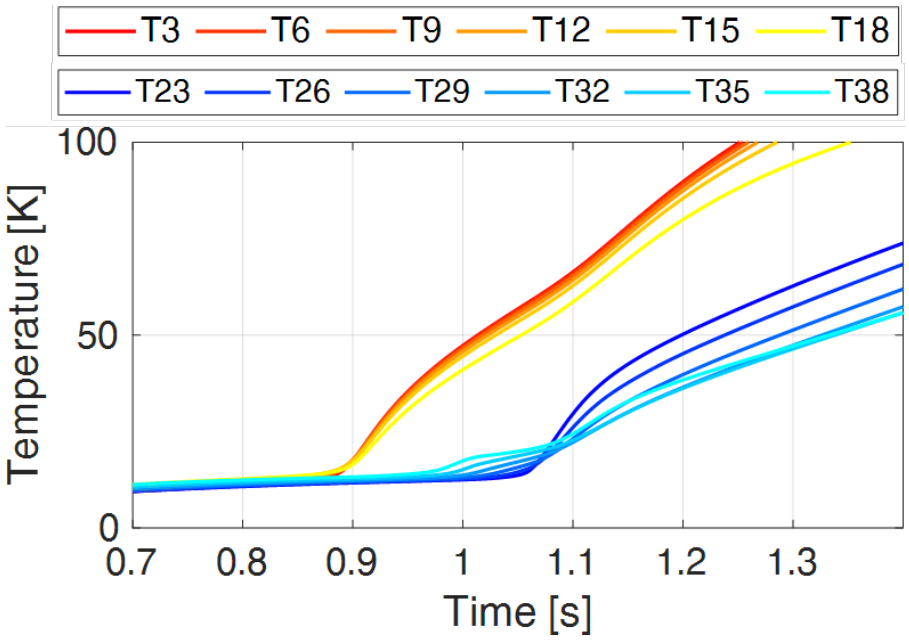

Figure 5.13: Temperature evolution in selected tapes of stack A and stack B.

Comparison of the three samples The comparison of the evolution of the hot-spot temperature in the three different configurations is shown in figure 5.14(a). The times at which the current is dumped are also shown. It can be seen that the current

dump, thus the quench detection, in C1 and C3 happens almost at the same time, while it is delayed by 0.5 s in C2. This is caused by the higher T_{CS} in C2 with respect to (half of) the tapes in C1 and C3. Having a higher T_{CS}, given the same conditions for all the three configurations, it requires more time for C2 to reach the quench detection threshold. Also, this is the reason for which it reaches a higher hot-spot temperature than, e.g., C3. This behavior, i.e., reaching a higher hot-spot temperature in case of higher T_{CS}, is consistent with what was observed also in LTS magnets [84]. In addition, even though the T_{CS} in C1 and C3 are very similar, the respective hot-spot temperatures are quite different. This is caused by the different configuration of the tapes. Indeed, C3 features a more uniform distribution of the tapes, thus it is easier for the current to flow from one slot to another or, eventually, from one slot to the core.

Concerning the quench fronts, for all the three configurations, the initial propagation is rather fast, while it slows down as soon as the fronts reach the regions where the magnetic field starts decreasing, see figure 5.14(b). The comparison is carried out considering the top tapes of slot A for all the three configurations. In all cases, the quench starts upstream with respect to the position where the maximum magnetic field is located. This asymmetry is introduced by the fact that the warm helium is flowing from left to right, thus the quench starts at the beginning of the region where the temperature margin is zero, i.e., at the beginning of the region at maximum magnetic field. The region inside the quench front then shrinks due to the current sharing with other (resistive) regions, which leads to an increase of the current sharing temperature in the superconductor.

The quench analyses carried out on the three samples had helped in designing the diagnostics of the samples. In particular:

- in more than one axial location, a temperature sensor as well as a voltage tap should be put on the jacket as well as inside the conductor cross-section. This should help quantifying the temperature and/or voltage difference present during the quench propagation within the conductor cross-section itself. It would be desirable to put sensors close to the stacks, close to the central channel and on the jacket, to describe with three values the temperature and voltage evolution in the cross-section.

- in order to capture with an acceptable level of accuracy the quench front propagation, both thermally and electrically, it was suggested to equip the sample with temperature and voltage sensors along the axial direction at least every 10 cm in the high field region.

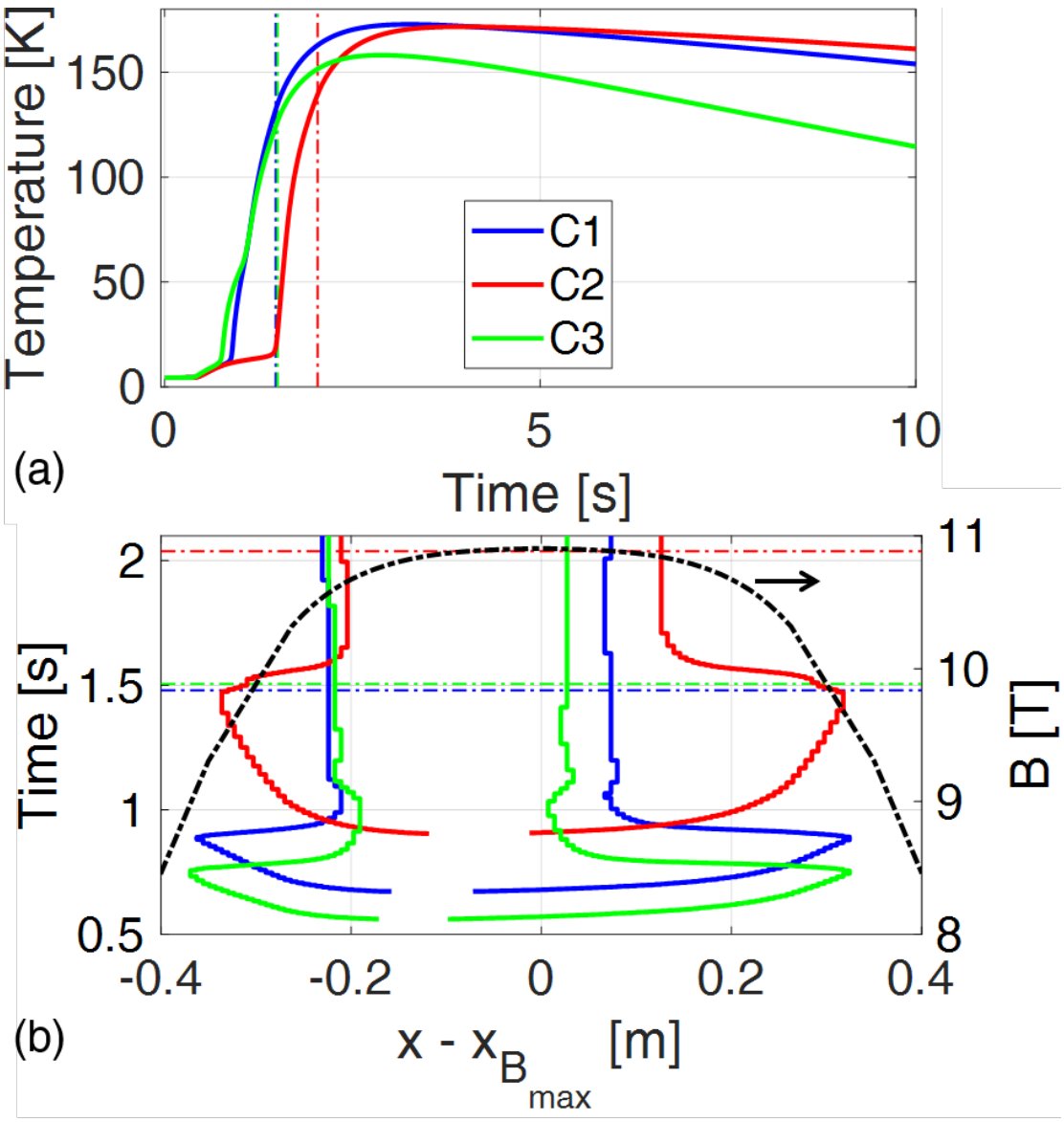

Figure 5.14: (a) Hotspot temperature evolution in the three configurations. (b) Normal zone propagation in tape T1 in the three configurations. The dashed-dotted lines indicates the current discharge times. On the right axis, the magnetic field distribution is also shown.

Quench initiated by AC pulse The strongest pulse that can be produced in SULTAN (in terms of amplitude and frequency) is a ± 2 T pulse (with period equal to 130 ms). However, it is needed to understand whether such strategy can induce a quench or not. In order to estimate the power (per unit length) deposited in the core by the AC pulse, a 2D electro-magnetic model, based on [85], has been developed. The model

computes, using the A-formulation of the Maxwell equations, the evolution of the (induced) current density, see figure 5.15 and electric field in the core cross-section. The evolution of the power deposition is computed as integral over the surface of the power density (**J**·**E**), see figure 5.16. The AC power evolution has then been used as input to the same 1D model described in Section 5.1.2.3. According to the model, and taking into account just the power deposited in the core (i.e., neglecting that deposited in the tapes), a quench will be induced in the CICC, if the maximum current and magnetic field in SULTAN are retained.

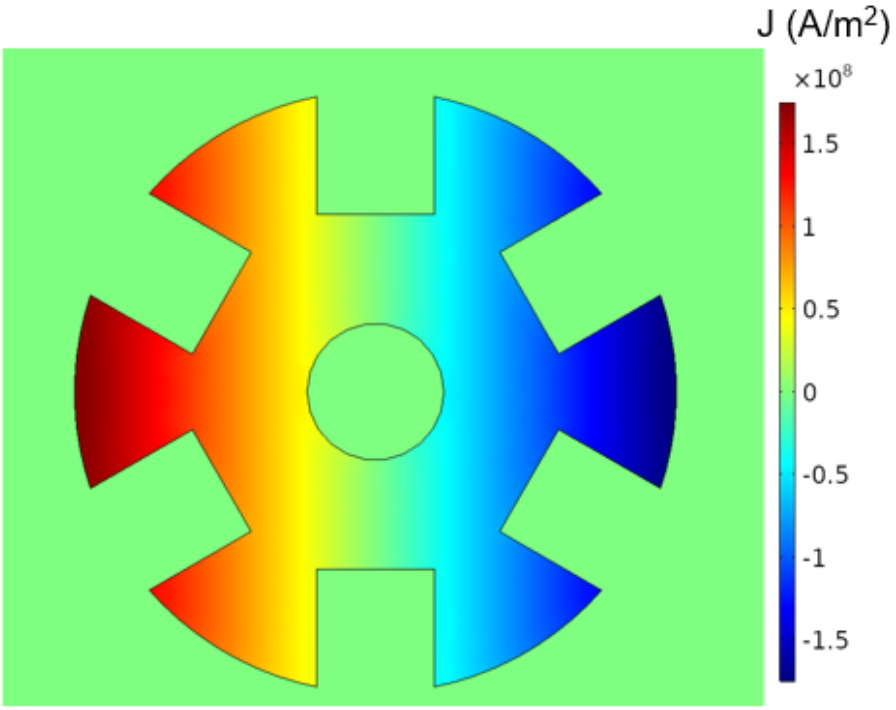

Figure 5.15: Distribution of the eddy current density during the AC pulse, computed with the 2D electromagnetic model.

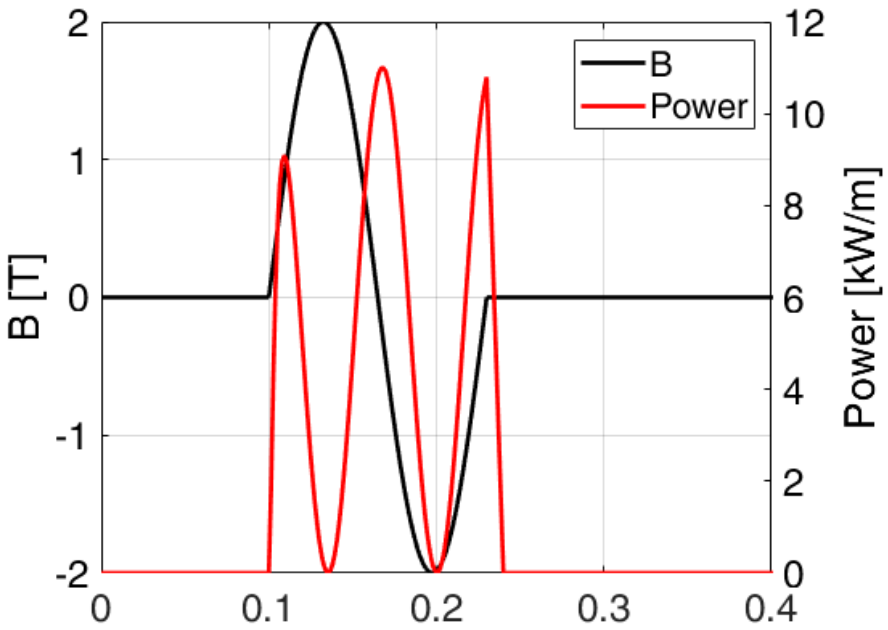

Figure 5.16: Evolution of the magnetic field pulse and evolution of the corresponding power coming from eddy currents computed in the core.

5.1.3 CroCo

In this section, the KIT CICC characterization from the thermal-hydraulic point of view, using CFD, is presented. After the characterization, the 1D model of the conductor is described and the quench analysis is carried out. The comparison between the results obtained with the two modelling approaches (using 4C and H4C) is discussed.

5.1.3.1 Conductor characterization

CFD analysis The aim is to derive, through numerical simulations, correlations for the friction factor (f) and heat transfer coefficient (h), for the CroCo layout of sub-channels. Here the interest is limited in exploring the dependence of f and h on the Reynolds number, i.e. on the mass flow rate flowing in the single subchannel, assuming SHe as fluid. In principle, however, the correlations can include the dependence on the geometry of the sub-channel, on the Prandtl number and so on [39], but this goes beyond the scope of this analysis.

Simulation setup The setup of the thermal-hydraulic simulations is summarized in this sub-section. We performed the simulations using the commercial software Simcenter STAR-CCM+ 2019.1.1 [57]. The computational domains considered in the analyses are two: the inter-strand sub-channel, see figure 5.17(b), and the strand-jacket

sub-channel, see figure 5.17(a). They are simulated independently, since it is assumed that there is no mixing between adjacent SHe sub-channels, for the sake of simplicity. The boundary conditions are set to fully-developed periodic [57]: this setting allows simulating only one twist pitch of the channels, reaching thermal-hydraulic fully-developed conditions and minimizing the computational domain as much as possible. This is achieved automatically imposing the outlet velocity, pressure and temperature fields as inlet boundary conditions after a suitable number of iterations. Note that the iterative procedure slows down the convergence, but the overall CPU time is lower with respect to a simulation with more than one twist pitch needed to reach fully-developed flow conditions in an entire twist pitch. The mesh adopted on the sub-channels cross-section is polyhedral equipped with prism layers at the wall in order to reliably solve the velocity and temperature gradients at the solid surface. The "directed mesher" [57] has been adopted: the inlet surface is meshed with the polyhedral mesh and the 2D cells are extruded in the flow direction, resulting in a 3D mesh. This approach has two advantages: 1) The number of cells is kept low, since each cell is elongated in the axial direction, which is consistent with the main flow direction; 2) The match between the inlet and outlet surface mesh is perfect and this is essential for the use of periodic boundary conditions. The simulations are steady-state, with constant He properties evaluated at 4.5 K and 6 bar. The selected turbulence model is the SST k-ω [86], with a second order constitutive relation between the shear stress and the derivative of the velocity components, in order to account for secondary flows, without the need of employing a more sophisticated and computationally expensive turbulence model, e.g. RSM. The wall treatment adopted in the simulation is a low y+ approach.

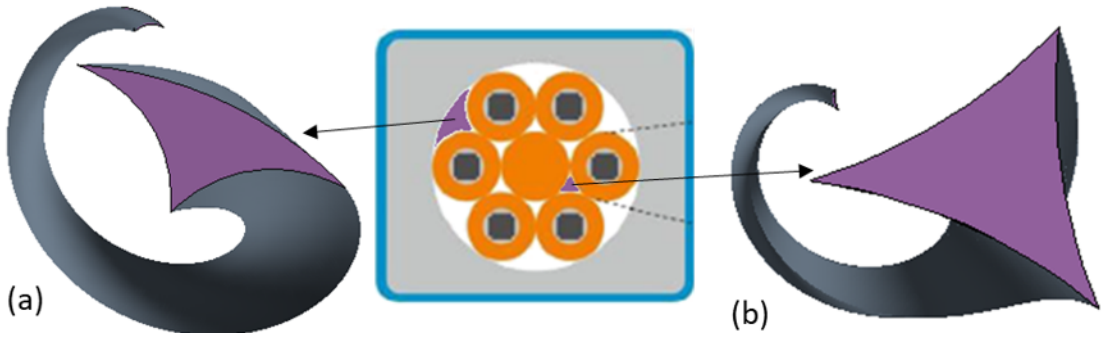

Figure 5.17: Computational thermal-fluid dynamic simulation: twisted single pitch fluid domains of the (a) strand-jacket and (b) inter-strand sub-channel, in the case of the HTS CroCo CICC.

Results The thermal-hydraulic results have been obtained after a careful mesh independence study and they are reported in figure 5.18. They show both the computed points for each selected mass flow rate and the best-fit that is used in the simulations presented in the main text. The expected decreasing and increasing trend for f and

h respectively is retrieved. However, the comparison with typical correlations with a suitable hydraulic diameter, e.g. Haaland and Dittus-Boelter correlations [60], confirms the need for the development of an ad-hoc correlation due to the very peculiar geometry of the sub-channels. Note also that, given the common hydraulic features of the geometry, e.g., triangular-like cross-section with sharp edges and same twist pitch, of both sub-channels, it is possible to find a single best-fitting correlation for the friction and for the Nusselt number. For both, an error bar of ± 10% brackets all the computed points.

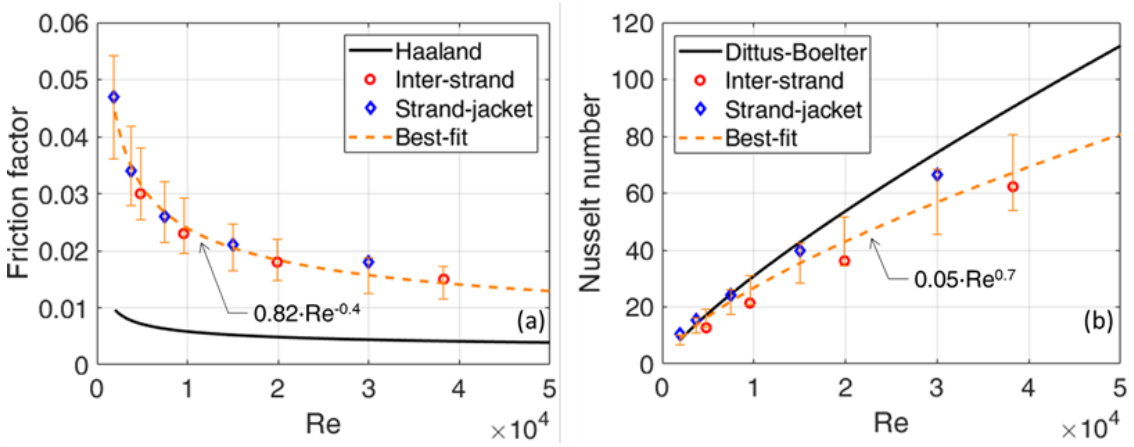

Figure 5.18: Computational thermal-fluid dynamic simulation: (a) friction factor and (b) Nusselt number correlations derived from the CFD analysis (symbols) of the strand-jacket and inter-strand sub-channels, compared with those available from literature (solid lines). The best-fit equations (dashed lines) are also reported.

5.1.3.2 1D model of the CICC

Simulation setup The main geometrical parameters and operating conditions considered in both 4C and H4C models are reported in table 5.5. The length considered is sufficient to observe the quench propagation while keeping the computational cost low.

Two cases have been simulated, both inducing the quench through external heating:

1. Case A: all the HTS strands are heated;
2. Case B: just one strand is heated with the same power considered in the previous case.

The power is injected through a heat pulse whose characteristics are reported in table 5.5 and it is slightly above the minimum quench energy. It is worth noticing that the pulse energy is about four times that necessary to induce a quench in an LTS CICC,

Table 5.5: Geometry, properties and operating conditions of the CICC.

Conductor length (m)	10
Magnetic field (T)	12
Current (kA)	50
Superconductor scaling law	From [58]
Inlet temperature (K)	4.5
Inlet pressure (bar)	6
Mass flow rate (g/s)	2.5
Material properties	[56]
Heated length (m)	0.1
Heat pulse duration (s)	0.1
Pulse energy (J)	400

such as the ITER Toroidal Field Insert Coil [70]. This agrees with the expectations of having a much larger minimum quench energy for HTS than for LTS [87].

The mesh of the 1D domains is adaptive following the algorithm proposed in [67], which refines/coarsens the mesh according to the (moving) quench front position. The time step is also adaptive according to the rate of change of the solution [67].

The discretization of the cross-section with the H4C is performed assigning one thermal and electric region at each HTS stack and another to each surrounding copper profile. One thermal and electric region is assigned to the central Cu rod as well as to the jacket, see figure 5.19(a). Thus, the thermal and electric regions are 6 + 6 + 1 +1 = 14 in total. Concerning the coolant, a fluid region is assigned to each He sub-regions, leading to 12 fluid regions. On the other hand, the discretization of the cross-section implemented in the 4C model is done assigning a single homogenized thermal region to the HTS stacks and all the surrounding copper profiles. A separate region is assigned to the jacket and a single fluid region is considered for the He, see figure 5.19.

The thermal resistance values for the copper-copper and copper-steel contacts were set equal to 0.005 m^2K/W and 0.002 m^2K/W, respectively, assuming a contact length equal to 2 mm and uniform along the length of the conductor. It has been shown that these interface parameters have a strong impact on the quench evolution, e.g., on the hot-spot temperature, see [88]. However, they are characterized by large uncertainties, thus an experimental characterization is envisaged in order to reduce the uncertainties to allow more reliable estimation on key quantities in quench analysis.

Results In this section, the results of the quench simulated in case A and B with H4C and 4C are reported and discussed.

Table 5.6: Models of the CICC cross-section implemented in H4C and 4C.

	H4C	4C
Thermal reg.	6 HTS SC 6 Cu profiles 1 jacket	1 Homogenized HTS stack + Cu
Fluid reg.	12	1
Electric model	Transient, 1D	Steady, perfect parallel of resistances
Electric reg.	14	3
Electric interface: transverse resistance	Transverse conductance: 10 MS/m [89]	No transverse resistance
Electric interface: inductances ($\mu H/m$)	Self: 1.7 [90] Mutual: 1.3 [90]	No inductive effects
Thermal contact resistance (m^2K/W)	Stack-Cu: 0.005 [88] Cu-SS: 0.002 [88]	Stack-Cu: 0 Cu-SS: 0.002 [88]
Interface between thermal and fluid regions	Heat transfer coefficient from correlation reported in section 5.1.3.1	Heat transfer coefficient from correlation reported in section 5.1.3.1

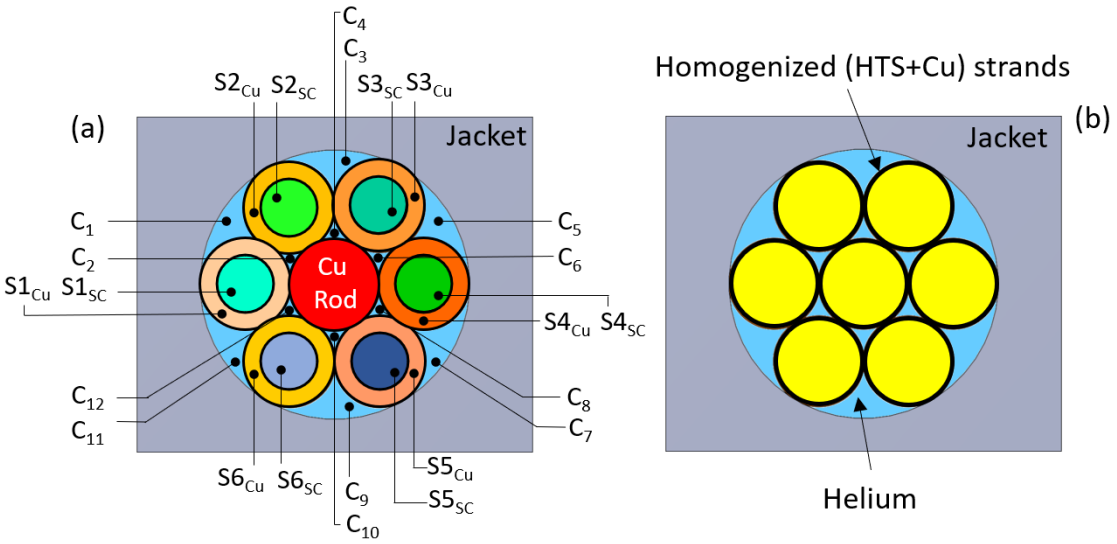

Figure 5.19: H4C (a) and 4C (b) cross-section discretization adopted for the HTS CroCo CICC. In (a), the distinction of the different thermal, electric (S#, with sub-regions SC and Cu) and fluid (C#) regions is shown.

Current The evolution of the current during the quench initiation and propagation is reported in figure 5.20. Recall that the H4C model can account for current redistribution in the different current-carrying elements and models separately the HTS stack (with its stabilizer) and the surrounding copper tubes.

In case A, the cross-section is uniformly heated, therefore the current and temperature evolution is the same in all the strands. Thus, for symmetry, only strand S1 has been reported in figure 5.20(a). During the heating, roughly half of the current is shared from the stack to the surrounding copper tube and the central copper rod. Note that the central copper rod has a larger (copper) cross-section than the strand equipped with HTS tapes, thus it has a lower resistance than the other copper tubes. After the end of the heating, the heat produced by Joule effect in the resistive materials, inducing a continuous increase of the temperature, leads (after an attempt of recovery at $t \sim 2.5\ s$), to the full transition to normal state of the HTS stacks at $t \sim 6\ s$.

The comparison with the 4C results, see figure 5.20(b), shows qualitatively the same evolution, i.e., part of the current is soon transferred from the stacks to the copper and then on a longer time scale it entirely flows in the copper regions. However, from a quantitative point of view, the fact that the copper rod has a different (lower) resistance with respect to the copper tubes is not taken into account in 4C, where the current flows through a single equivalent copper region. This implies that the resistance, thus the current and in turn the temperature evolution are slightly different. In particular, a larger portion of the current flows in the SC region according to the 4C results. Consequently, less current flows in the copper, thus less heat is produced, which in turn has an impact on the temperature, see the next section.

As far as Case B is concerned, the effect of a more localized heat deposition is investigated. In this case, heat is deposited in S1, which loses fast its superconducting state. In few tens of ms, also S2 (and for symmetry S6) is heated above its T_{CS}, thus becoming normal see figure 5.20(c). Nevertheless, strands S3 (and for symmetry S5) and even more S4 are colder and they are still superconducting. Indeed, the current is transferred from the quenched strand (S1, S2 and S6) to them, which carry more than 15 kA each. However, also those strands are being heated by conduction from the others and the current reaches their critical current, thus current starts to be shared progressively more with the copper tubes and the central copper rod. In this case, the evolution of the current, seen from a global point of view, is smoother, see figure 5.20(d), than the previous case. The current evolution computed by 4C is instead of course the same as in Case A: its "homogenized" model of the cross-section does not allow to catch the qualitatively different (much slower) current evolution, due to the much more localized heat deposition.

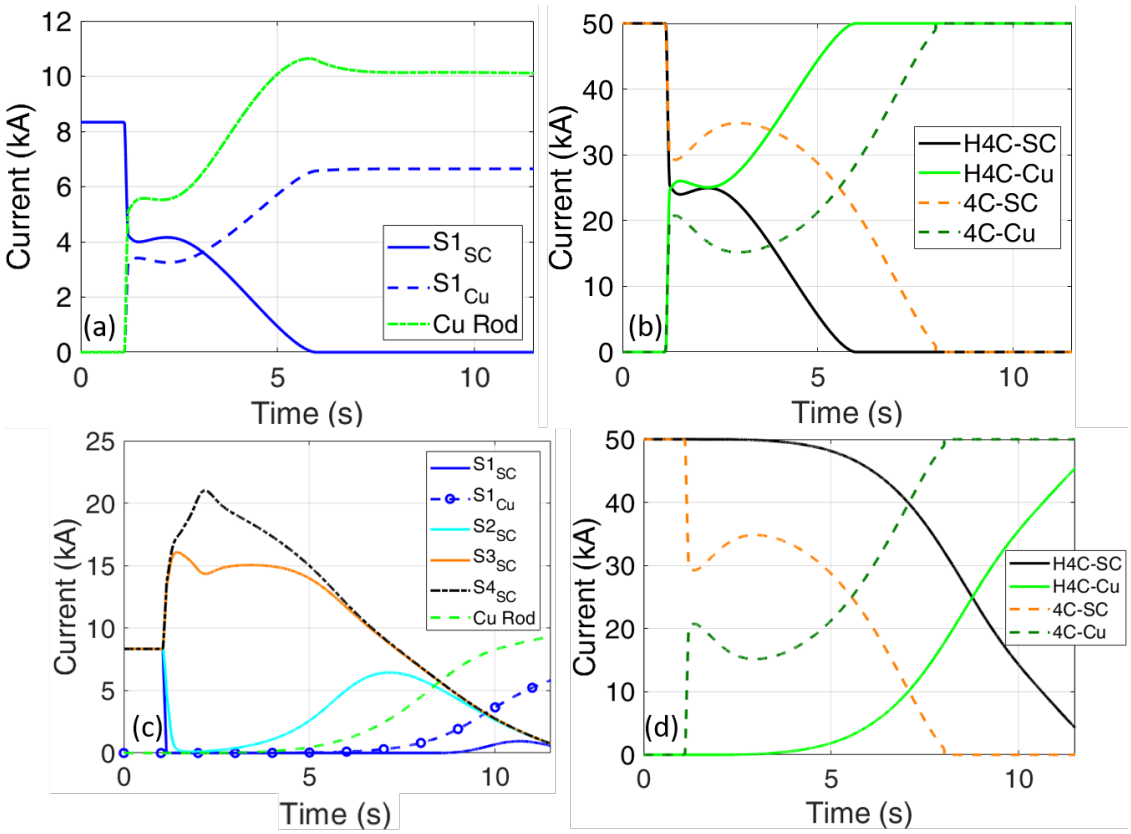

Figure 5.20: Current evolution in selected regions computed by H4C in case A (a) and case B (c). Comparison of the current evolution computed by H4C (summing all the contributions in the superconducting and copper regions) and 4C in case A (b) and case B (d). The values are taken at x = 5 m.

Temperature The temperature evolution in the middle of the heated region, i.e., at $x = 5\ m$, is shown in figure 5.21.

The temperature values computed in case A by 4C and H4C are very similar in the first few seconds of the transient, since the heat deposition is homogeneous on the cross-section. However, after $\sim 4s$, the temperature computed by H4C grow faster than that computed by 4C. This is caused by the current evolution discussed before in section 5.1.3.2. Indeed, the portion of the current flowing in the copper according to the H4C results is larger than that computed by 4C, thus the heat generation is larger, causing a faster rise of the temperature. This implies larger temperature difference as the transient evolves. Furthermore, 4C underestimates the temperature by tens of K for temperature values larger than 150 K, which is not a desirable feature in this kind of computation.

In case B, on the other hand, since the heat is deposited just in strand S1, its temperature spikes to more than 150 K and slowly decreases due to conduction with the other, colder, strands. On longer time scales, also the restoring of the He flow contributes to the decrease of the S1 temperature. The temperature of the strands surrounding S1 increases slowly and according to their location, i.e., S2 and S6 are heated first, then the central rod etc., see figure 5.21. Of course, the larger the number of the strands, the slower the heat transmission to the farther strands. This implies also that with a low number of strands, such as 3, as it is in the sub-sized samples, a simpler model with just one thermal region could be enough, since in case of localized heating of one strand as in this case, the others, being always in direct contact with it, will be heated up quite fast (reducing the temperature gradients), as shown in [9].

In this case of localized heating, a modelling approach as that typically used in LTS and implemented in 4C shows its limitations. Indeed, it fails in capturing the fast and large increase of the directly heated strands as well as the slow temperature increase of the other strands. Even the comparison of the average temperature computed by H4C with that computed by 4C shows a large discrepancy already after few seconds. This is caused by the current redistribution that is peculiar of this case: 4C does not capture the redistribution of the current from the directly heated strand to the - still superconducting - strands. Thus, it overestimates the heat generation and, in turn, the increase of the temperature.

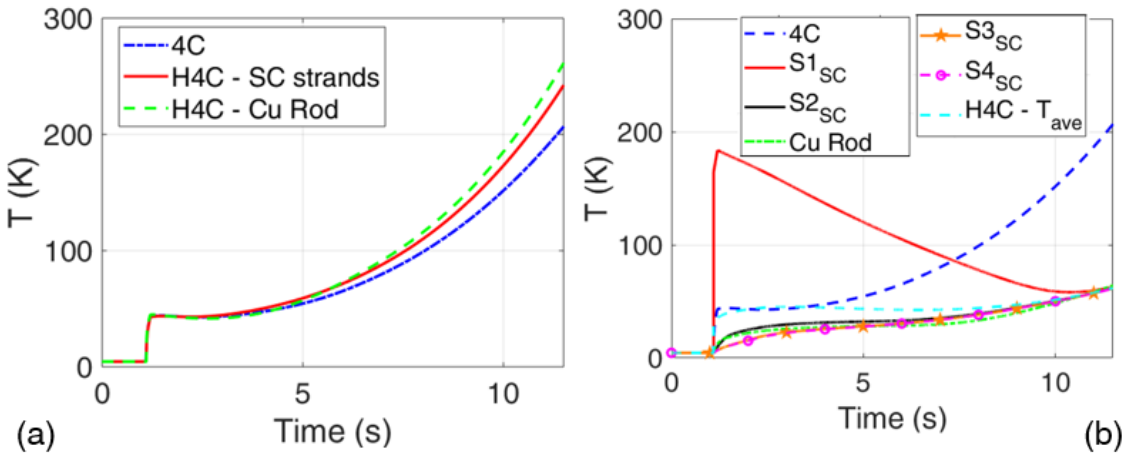

Figure 5.21: Temperature evolution computed at x = 5 m with H4C and 4C in case A (a) and case B (b).

Voltage The voltage evolution in the two cases is reported in figure 5.22.

In case A, the evolution of the voltage follows that of the temperature increase. Indeed, the voltage computed by 4C is similar to that computed by H4C in the first phase of the transient, while, after that, it increases faster according to the H4C results. This is because the higher the temperature - as discussed in section 5.1.3.2 -, the higher the copper resistivity, where most of the current flows after the heat pulse.

The voltage increase computed in case B by 4C is the same as the previous case. However, in this case the voltage computed by H4C increases much slower. This is caused by the initial redistribution in the superconducting strands which is captured by H4C rather than 4C. Thus, in the initial phase, i.e., the first 5 s, the current is still transported by the superconductor, leading to negligible voltage in H4C simulation.

A more quantitative comparison can be performed considering the same voltage, e.g., 100 mV (which is a typical voltage threshold for quench detection [58], and comparing the temperatures computed by the two models. In the case of uniform heating, the voltage and the temperature are close, as discussed before. In the case of non-uniform heating, in H4C simulation 100 mV are reached at 13.1 s, when the temperature reaches 80 K. Thus, 4C is overestimating the temperature in the cross-section while underestimating the local temperature increase of the directly heated strand. This implies that a more detailed model than 4C is needed to carefully investigate heating scenarios different from a uniform heating.

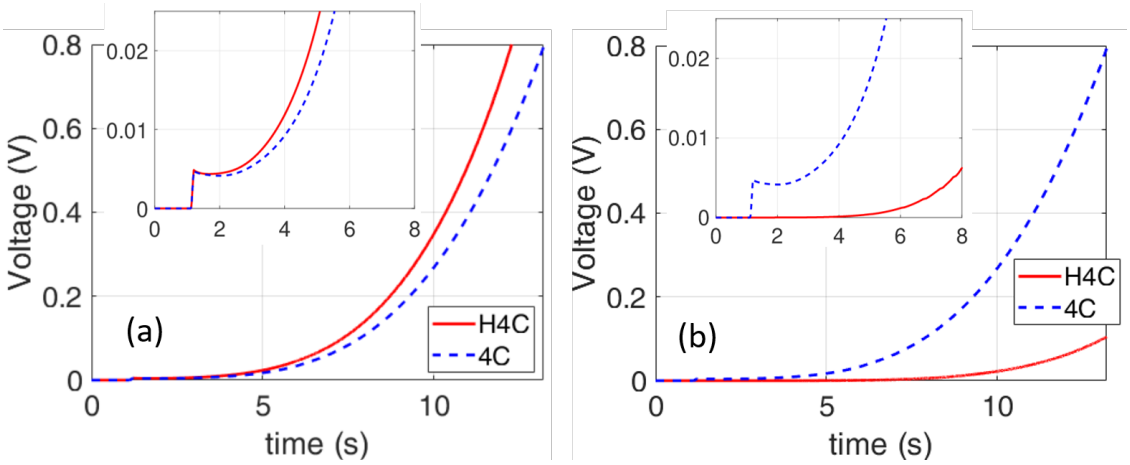

Figure 5.22: Voltage evolution computed by H4C and 4C in case A (a) and case B (b).

He speed Comprehensive considerations on the dynamic behavior of the He, in particular in terms of pressure, would require the model of self-consistent boundary conditions, e.g., due to the presence of the cryogenic circuit which supplies He to the conductor. However, even without the modelling of the circuit, it can be possible to compare the results of the two models in the region close to the heated zone and not far in time from the heat pulse.

The comparison of the velocity profiles is shown in figure 5.23. It can be seen that the expected qualitative behavior of the velocity is retrieved by the two models: the localized heating and the subsequent quench initiation leads to an acceleration towards the conductor outlet, an almost stagnant region where the heating took place and a deceleration (up to the inversion of the flow) towards the inlet of the conductor. In more quantitative terms, in case A, both the acceleration and deceleration in the H4C results are stronger than in those of 4C. This is caused by the different discretization of the He cross-section. In 4C, the entire He mass is lumped in one region, therefore the localized heating produces a less pronounced perturbation in the He flow than in the H4C results. Recall that, in H4C, each He sub-region is modelled independently, thus the smaller the He volume, the larger the perturbation in the He flow. The same is true and more evident for case B, in which the effect of the non-uniform heating is reflected in the He flow dynamics. The portion of the conductor which is heated is strongly perturbed, while the region in which the *thermal* wave is not arrived yet is basically unperturbed, see figure 5.23(b). This implies also a different (and non-uniform) degree of pressurization in the He sub-regions and can be seen only with a detailed model such that implemented in H4C. Moreover, it is worth noting that assuming the perfect segregation of the He sub-channels is conservative, since it is the worst situation for the pressurization, because the small volume region pressurizes more than the larger and they cannot relief their pressure in other (colder or larger) sub-regions.

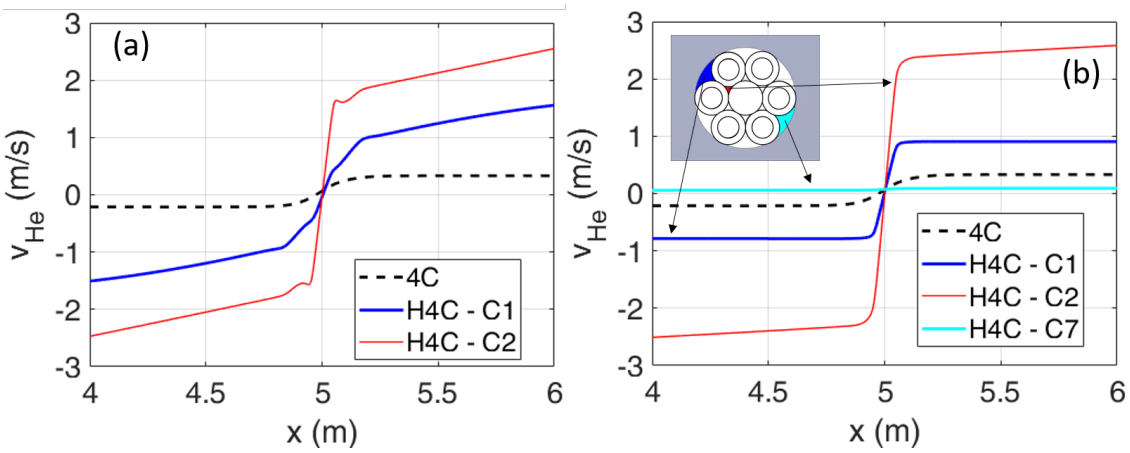

Figure 5.23: He speed profiles computed by H4C and 4C in case A (a) and case B (b). The profiles are taken 60 ms after the end of the heat pulse. The speed profiles in selected He sub-channels computed by H4C are reported.

5.2 Magnets

The H4C code, initially developed for the analysis of (fast) transients in HTS CICCs, was then upgraded to deal with the analysis of (fast) transients in HTS magnets.

The necessary upgrade was the implementation of the capability to take into account inter-conductor heat transfer. This feature is important when large temperature differences between adjacent turns, layers or pancakes arise, such as during quench propagation. This was already implemented in the 4C code and it was recently improved to more easily take into account any type (and any detail) of a magnet topology.

In addition to the capabilities already implemented in 4C, from the implementation point of view, an important improvement to decrease the computational cost of simulating magnets was implemented in H4C, see Appendix A.

5.2.1 The EU DEMO CS

The aim of the analysis is to study the impact of a very localized defect on the performance of the entire coil. This is motivated by the fact that the manufacturing process of HTS CICC is still not industrialized and it is known that HTS tapes are prone to develop localized defects since their production. The case study is here the hybrid EU DEMO CS coil, see [91]

5.2.1.1 Conductor cross-section discretization

The defect(s) are supposed to be in the first layer, which is the most critical (if we focus on the HTS layers), since it is exposed to the maximum magnetic field. Therefore, a finer discretization of the cross-section of the conductor in L1 has been implemented, see

figure 5.24. It has been used the same approach adopted for the KIT CICC, discretizing each superconducting stack and each copper tube with a separate region, leading to a total of $7 \cdot 2 = 14 + 1$ region for the central copper core and 1 region for the jacket = 16 electric and thermal regions. For the second layer made of HTS a coarser discretization has been adopted, since the thermal disturbance is way less strong than in L1. For L3, which is made by LTS, the typical discretization used for those type of cables has been implemented.

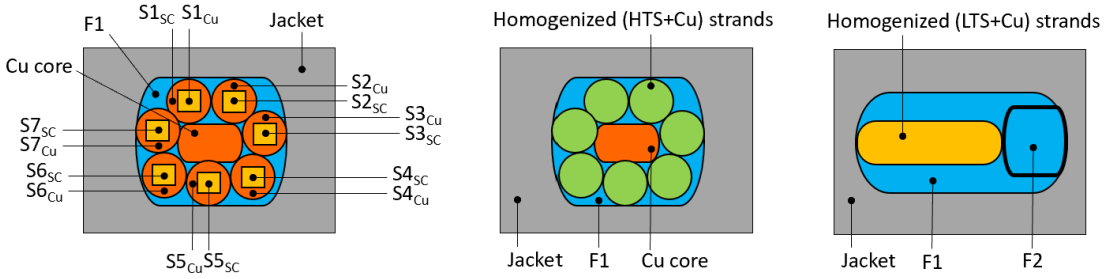

Figure 5.24: Discretization of the cross-section of the three layers (L1 to L3, from left to right) of the EU DEMO CS adopted in the H4C model.

5.2.1.2 Simulation setup

The simulation setup adopted is summarized below:

- Current evolution: it includes all the relevant instants of the plasma scenario, see figure 5.25. The breakdown (BD) is the most crucial part since it features a strong and fast reduction of the current (roughly 10% in less than 1 s), see figure 5.25(b), and consequently of the magnetic field, which is mainly self field, (with a ramp of about 1 T/s), inducing a large power deposition.

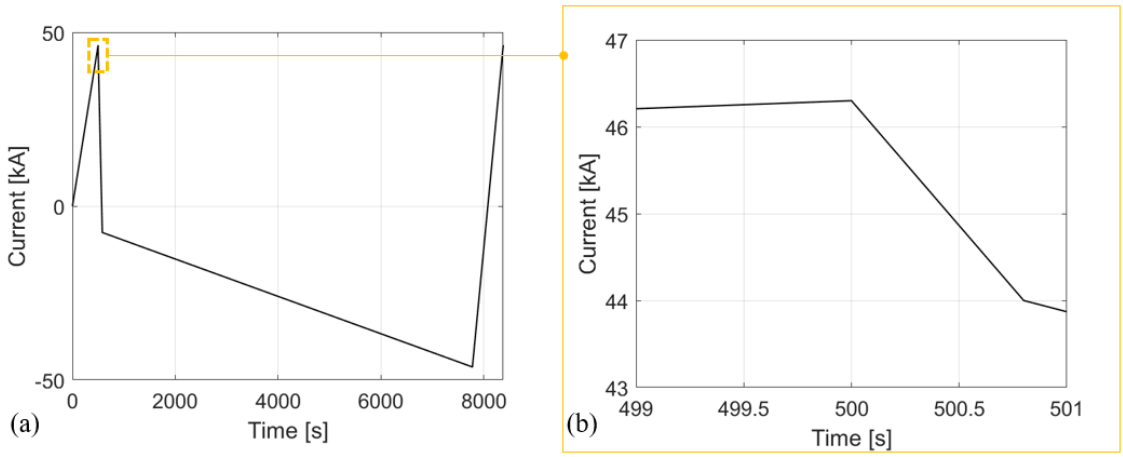

Figure 5.25: Evolution of the current in CS1 during a complete plasma scenario (a). Zoom on the breakdown phase (b).

- Magnetic field evolution: both its distribution and evolution is given by [92] and it is reported in figure 5.26(a). Note that the distribution of the field is rather uniform in each hydraulic channel, see figure 5.27(a).

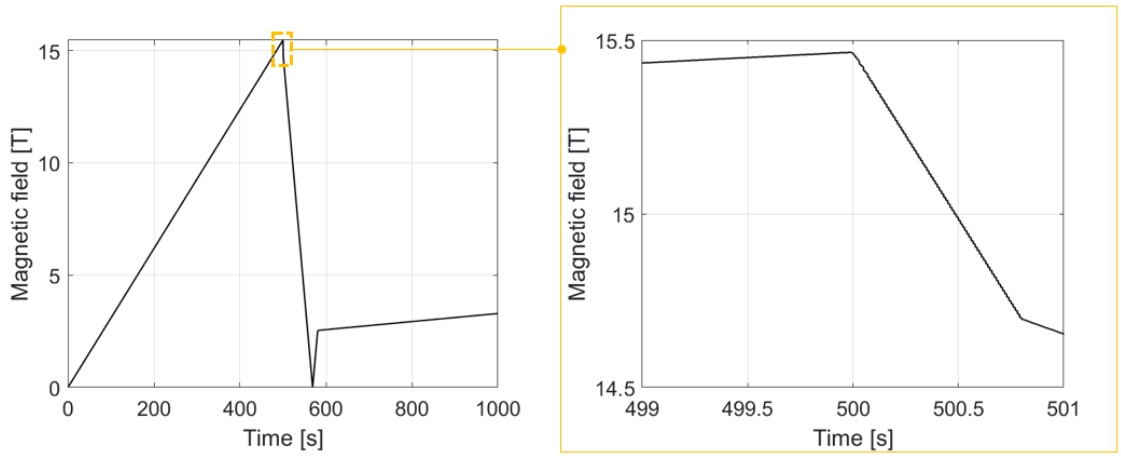

Figure 5.26: Evolution of the magnetic field amplitude in the first 1000 s of the scenario (a). Zoom on the magnetic field evolution during the breakdown (b).

- AC losses: so far, AC losses in HTS CICC are still under investigation both numerically and experimentally. Therefore, for the time being, some reference values are used which will need to be updated as soon as more realistic values are available. In these simulations, only the coupling losses are taken into account. They

have been computed according to:

$$P(x,t) = \frac{n\tau}{\mu_0} \cdot A_{stack} \cdot \left(\frac{dB(x,t)}{dt} \right)^2 \tag{5.9}$$

where $n\tau = 75ms$, $\mu_0 = 4\pi \cdot 10^{-7} H/m$, A_{stack} is the stack cross-section, $B(x,t)$ is the magnetic field. This leads to a heat deposition of roughly 27 W/m during the 0.8 s of duration of the breakdown. For comparison, the subsequent current (and field) ramp induces 1.4 W/m.

- Inlet and outlet pressure are set to 6 and 5 bar, respectively.
- Inlet temperature is set at 4.5 K.
- Defect: the presence of a defect is approximated considering a localized drop of the critical current, see figure 5.27(b). Different levels of defects have been investigated, including the case of no defects in order to have the reference of the nominal (expected) performance. The results of the nominal performance are in line with those presented in other analyses [93].
- Quench detection and current dump: in case of quench, the voltage threshold for the detection is set to 0.1 V and the (exponential) current discharge time constant is assumed to be 15 s.

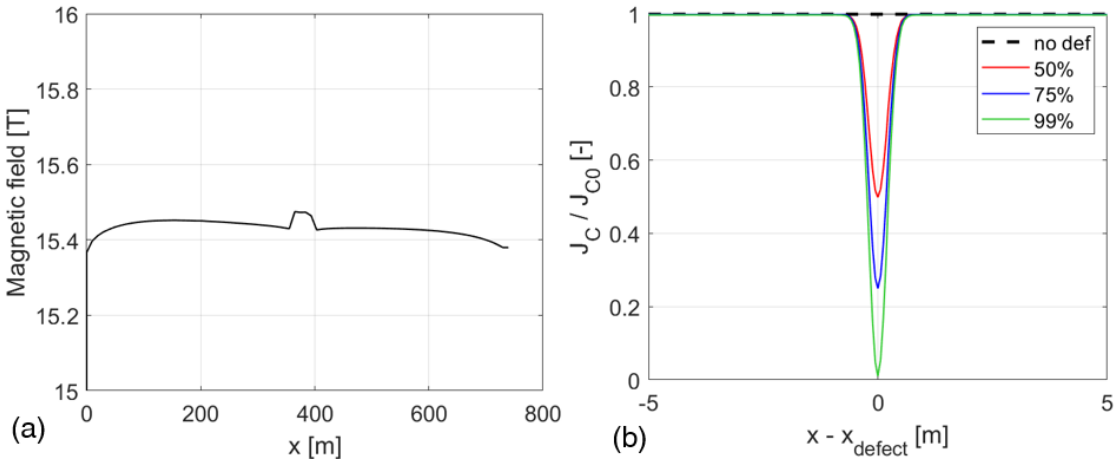

Figure 5.27: Distribution of the magnetic field along the hydraulic channel in L1 at t = 500 s (before the breakdown) (a). Distribution of the normalized critical current density around the defect for the different defects considered (b).

5.2.1.3 Results - Plasma burn

In this section, the impact of the defect on the nominal performance of the conductor is investigated.

Current evolution The evolution of the current in the location of the defect is reported in figure 5.28(a). It can be noticed that depending on the entity of the defect, the current redistributes accordingly during the current ramp up, reaching in the damaged strand a steady value that is compliant with the defect itself. Notice that the current reaches a plateau even if the total current is still ramping up.

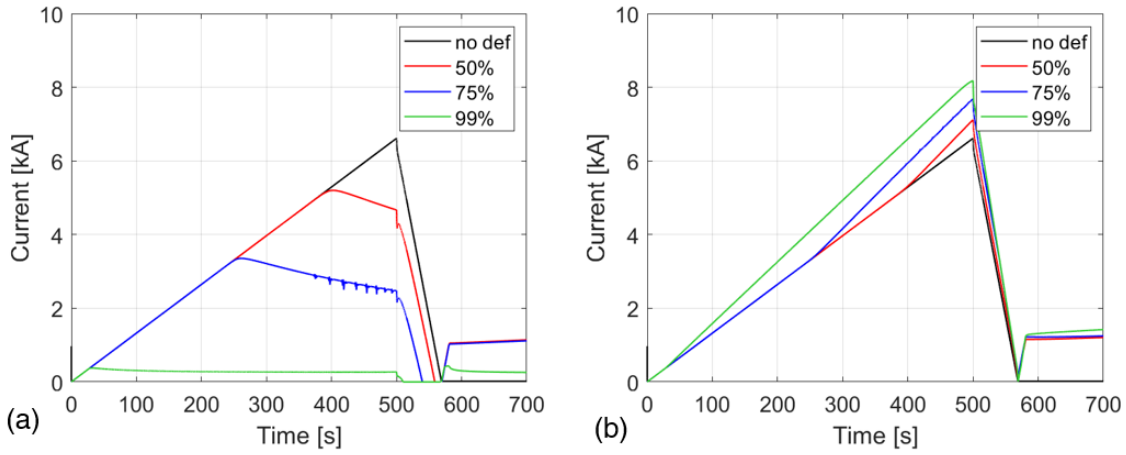

Figure 5.28: Evolution of the current in the damaged strand (a) and in the (undamaged) strand close to the damaged one (b) for the different levels of defect considered.

This hints that other strands are carrying more current with respect to what they do during normal operation. This is indeed represented in figure 5.28(b): the evolution of the current in the strand adjacent to that with the defect shows that the larger the defect, the higher the current carried by the adjacent strand. This has of course a direct impact on the (local) temperature margin of the single strands, see next section. It is worth noticing also that in the case of 99 % defect, the current in strand 2, i.e., the strand adjacent to that with the defect, approaches the critical current, which is 8.4 kA for each strand at 4.5 K and maximum field, i.e. just before the breakdown. Indeed, it reaches 8.2 kA showing a sort of saturation. This is because the conductor is warmer than 4.5 K, thus the critical current is lower than 8.4 kA, see the discussion on the temperature margin below.

Temperature margin In this section, the temperature margin evolution is discussed. The focus is on the breakdown, since the minimum margin is reached there. The temperature reached by the conductor during the BD is basically the same for all the cases investigated, i.e., the entity of the defect does not affect the temperature rise, see figure

5.29(a). This is expected, since the thermal properties as well as the power deposition does not depend on that, except the case in which the defect does not lead to a quench, see below.

In order to understand the evolution of the temperature margin, it is useful to analyze the evolution of the conductor temperature and of the current sharing temperature separately, see figure 5.29(b). Recall that at t = 500 s, the magnetic field and the current are at their maximum, thus leading to the minimum current sharing temperature. The BD lasts from t = 500 s to t = 500.8 s, during which a large power is deposited in the conductor, thus leading to a fast and large increase of the conductor temperature, see again figure 5.29(b). However, during the breakdown the current and the magnetic field in the conductor are decreasing, thus, while the conductor temperature increases, also the current sharing temperature increases. The minimum value of the temperature margin is then a trade off between the increase of the conductor temperature and the increase of the current sharing temperature.

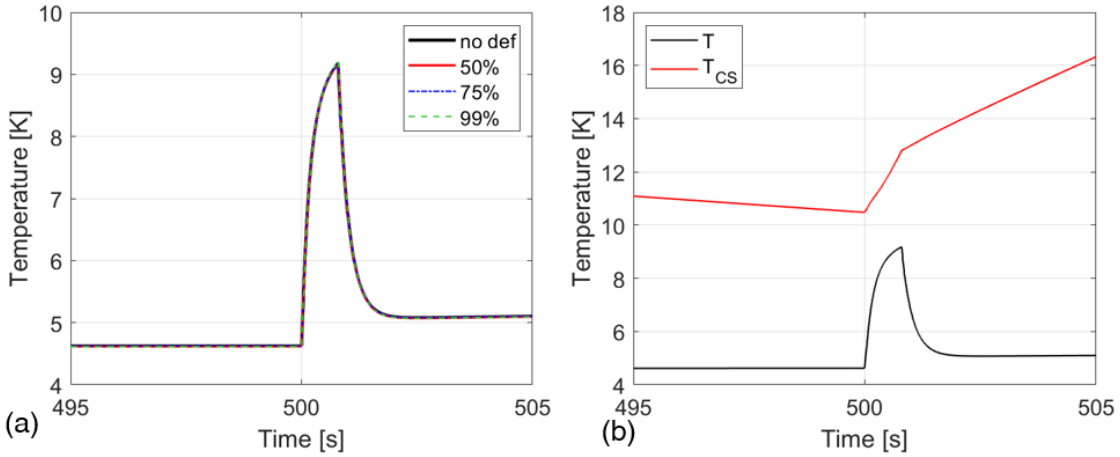

Figure 5.29: Evolution of the conductor temperature during the breakdown for different levels of defects (a). Evolution of the current sharing temperature and conductor temperature in the undamaged strand during the breakdown (b).

Furthermore, the temperature margin in the strands of L1 is strongly non-uniform, see figure 5.30. This is the direct consequence of the strong non-uniformity of the current distribution in the conductor cross-section. Indeed, since strand #1 carries less current, it has a larger temperature margin, even though its critical current is locally lower. The other strands, featuring all the same - nominal - critical current, have a temperature margin which depends on their position with respect to the damaged strand. Indeed, strands #2 and #7 are the closest, thus carrying more current than any other strand in that portion of the conductor. Consequently, their temperature margin is 1 K lower than the other non-damaged strands throughout the plasma burn. Therefore, in case of the presence of a defect, the minimum temperature margin is non-uniform

within the cable cross-section and it is reached in the strands closer to the damaged strand since they carry more current than all the others.

Note that by symmetry the behavior of SC2 equals that of SC7, SC3 that of SC6 and SC4 behaves as SC5. The temperature margin is the strands far from the damaged one is higher and very similar. The margin in SC3 (and SC6 for symmetry) is slightly lower than in SC4 and SC5 because they carry slightly more current.

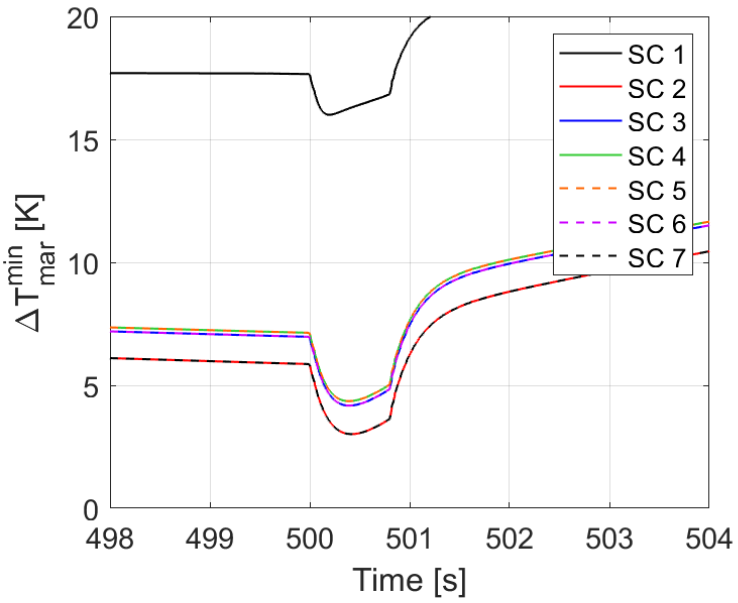

Figure 5.30: Evolution of the temperature margin during the breakdown in all the stacks in case of 50 % damage. The numbering follows that represented in figure 5.24.

The comparison of the temperature margin in the strands where the minimum margin is reached is plotted in figure 5.31. First, the minimum margin in case of no defects is reached at t = 500.4 s and it is equal to 5.4 K. This means that in the first part of the BD, the increase of the conductor temperature is stronger than the increase of the current sharing temperature, thus leading to the minimum temperature margin.

It can be noticed that the minimum margin is strongly affected by the presence of a defect: the margin decreases by 2.5 K going from a non-damaged strand to a case in which the damage leads to a decreases of 50 % of the critical current, by other 2.3 K for a 75 % damage and a further 1.7 K decrease in case of a completely damaged strand. In this last case, the temperature margin in SC2 (and for symmetry in SC7) is lower than 0, meaning that the current has reached the critical value and the conductor temperature is larger than the current sharing temperature. Nevertheless, the conductor manages to recover from the current sharing status since only two strands have a negative temperature margin and the current can effectively redistribute - on longer time scales - to the other strands. However, it is clear that the impact of a very localized defect (few

cm in one strand) deteriorates a lot the conductor performance and can quickly lead to current sharing even during nominal operation.

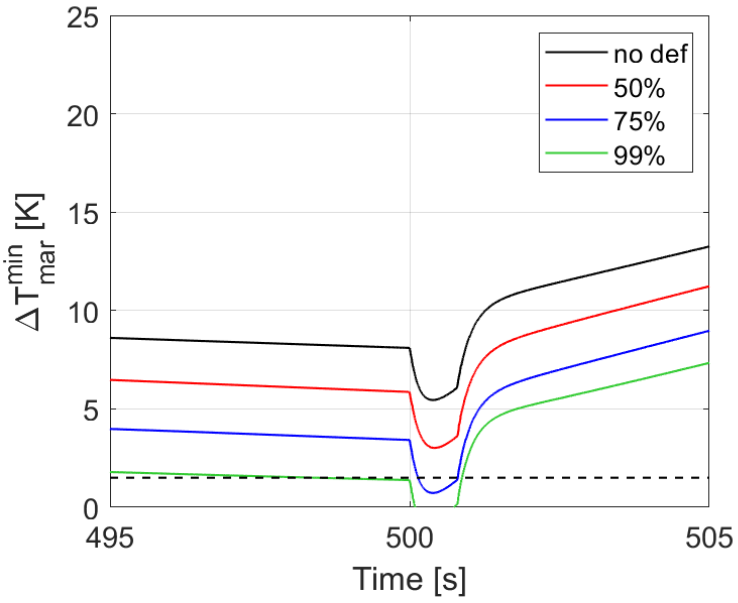

Figure 5.31: Evolution of the temperature margin during the breakdown in the undamaged strand (close to the damaged one, where the minimum margin is reached) for the different levels of defect considered in the analysis.

5.2.1.4 Results - Quench

In this section, the results of a quench propagation caused by the normal operation, but with two strands (S1 and S2) damaged to 75 % are presented. The evolution of all the quantities discussed below is taken at $x = x_{defect}$, where the maximum temperatures and strong current distribution take place.

Voltage and current From the evolution of the voltage in L1, see figure 5.32(a), the quench is detected at t = 502.8 s, that is after the breakdown and during the plasma current ramp up phase, see figure 5.33. Therefore, the breakdown phase causes the large energy deposition, as discussed above, and, since the current and magnetic field are still close to their maximum values, the quench starts even if the heat deposition has dropped to 1.4 W/m.

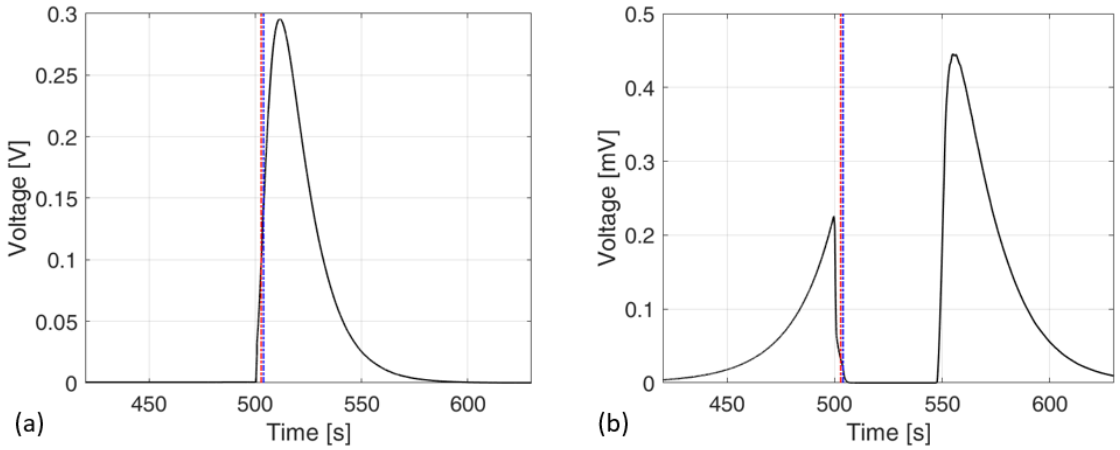

Figure 5.32: Evolution of the voltage across the layers L1 (a) and L3 (b). The times of quench detection and current discharge are represented by the vertical dashed-dotted red and blue lines, respectively.

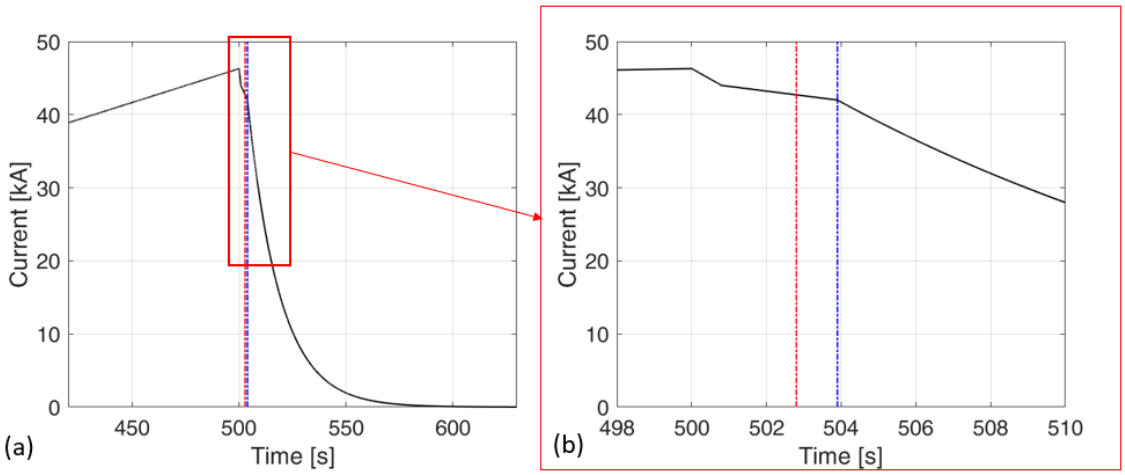

Figure 5.33: Evolution of the imposed total current (a) and zoom of the breakdown, beginning of the plasma current ramp up and current dump (b). The times of quench detection and current discharge are represented by the vertical dashed-dotted red and blue lines, respectively.

The current evolution in the different stacks of L1 is shown in figure 5.34. Note that, for symmetry, the behavior of S1 and S2 is the same, as well as that of S3-S7 and S4-S6, according to the numbering shown in figure 5.24. It can be noted that the damage of S1 (and S2) leads S3 (and S7) to operate close to their critical current once the total current is reaching its maximum value, i.e. at t = 500 s. Indeed, the increase of the current carried by S3 stops at $\sim 8.5kA$, but the total current is still increasing, thus the remaining part of the current, which is not carried by S3 and S7, starts to be carried by

S4 (and S6) and S5. This is visible in figure 5.34 where the increase of the current in those strands is no more linear after S3 and S7 saturate at their critical current.

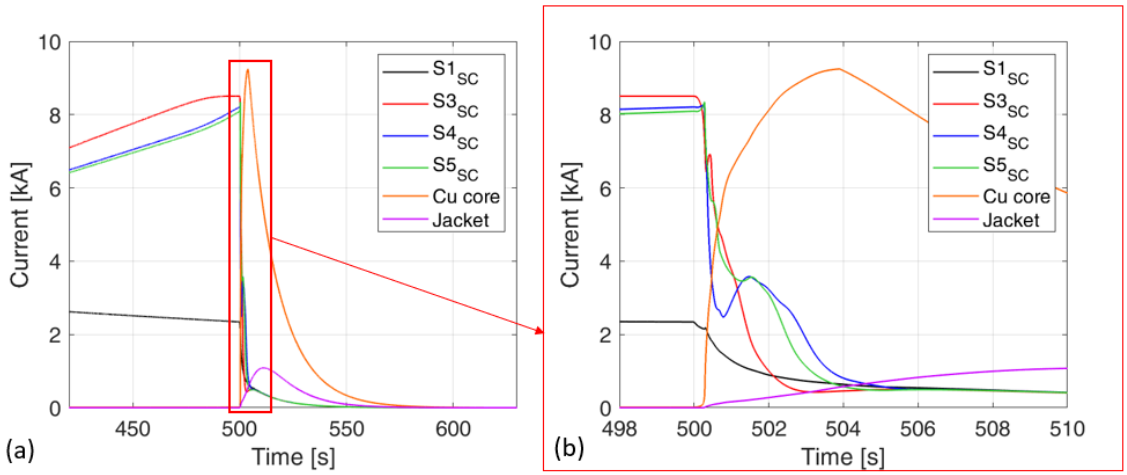

Figure 5.34: Evolution of the current in the HTS stacks of selected strands, in the copper core and in the jacket (a). Zoom on the interval around the quench detection and current dump (b).

Therefore, the margin distribution, in terms of current to critical current, at the beginning of the breakdown is critical, because 2 of the 7 (S3 and S7) strands are at their critical current, other 2 (S1 and S2) are damaged and they cannot carry more current than 2.3 kA, see the black curve in figure 5.34 and the remaining 3 (S4, S5 and S6) are carrying more current than their nominal value.

The consequence is that the heat deposition caused by the breakdown is too large with respect to the energy margin left in these conditions. Indeed, the current redistribution starts at t = 500.5, when the current carried by all the stacks decreases and the current in the respective stabilizer starts increasing, see figure 5.35 as well as in the central copper core, see the orange curve in figure 5.34(b). A portion of the current starts flowing also in the jacket, which is typical during quenches and it was also observed in LTS CICC quench simulations and experiments [71].

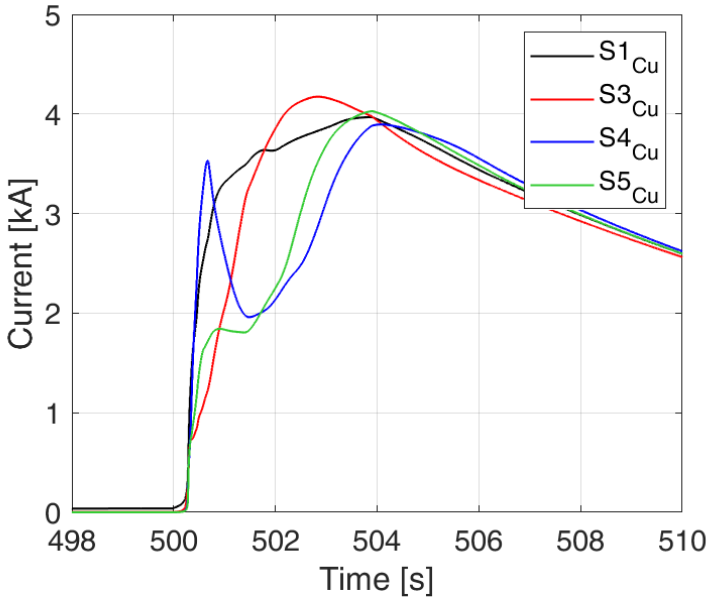

Figure 5.35: Evolution of the current in the copper profiles of selected strands in the interval around the quench detection and current dump.

Temperature The maximum temperature during the quench propagation is reached in the copper core, while in the stacks the temperature reaches $\sim 140K$, see figure 5.36(a), which could be acceptable, even though there is a strong uncertainty on the AC losses generated in these kind of conductors, thus it could also be underestimated, since during the current dump the power deposited by the AC losses is comparable to that deposited during the breakdown ($\sim 25W/m$ at the beginning of current dump and $\sim 27W/m$ during the breakdown).

It can be seen from figure 5.36(b) that the non-uniformities in the cross-section in terms of J_C, leads to a strongly non-uniform current distribution throughout the quench propagation, which in turn leads to a non-uniform temperature distribution in the cross-section. These non-uniformities, from the temperature point of view are large in the first seconds (up to around 30 K between adjacent strands, e.g., S4 and S3) and they tend to disappear after roughly 10 seconds from the onset of the quench. These behavior could lead to thermo-mechanical stresses, which could impact on the stack performance, as already highlighted in the quench simulations of the HTS ENEA CICC.

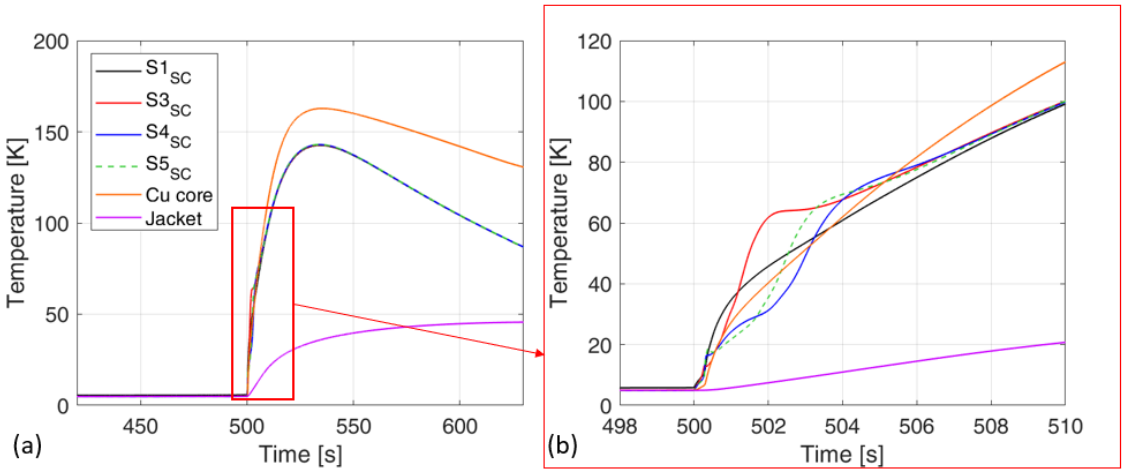

Figure 5.36: Evolution of the temperature of the HTS stacks of selected strands, of the copper core and of the jacket (a). Zoom on the interval around the quench detection and current dump (b).

The strong heating due to quench propagation in L1 leads to the heating, coming from the corresponding jackets, of L2 and then L3, see figure 5.37. This behavior is expected, since it happens also in LTS magnets. In this case, however, a quench in L1 could lead to a quench (at low current) in L3, which is wound with a "classical" Nb_3Sn conductor, thus featuring a much lower T_{CS} with respect to L1 and L2. This is indeed confirmed by the voltage traces reported in figure 5.32(b), where a voltage increase is present at t = 547 s, when the voltage in L1 is already monotonically dropping, but the total current is still 2.3 kA, thus possibly leading to quenches in the LTS layers.

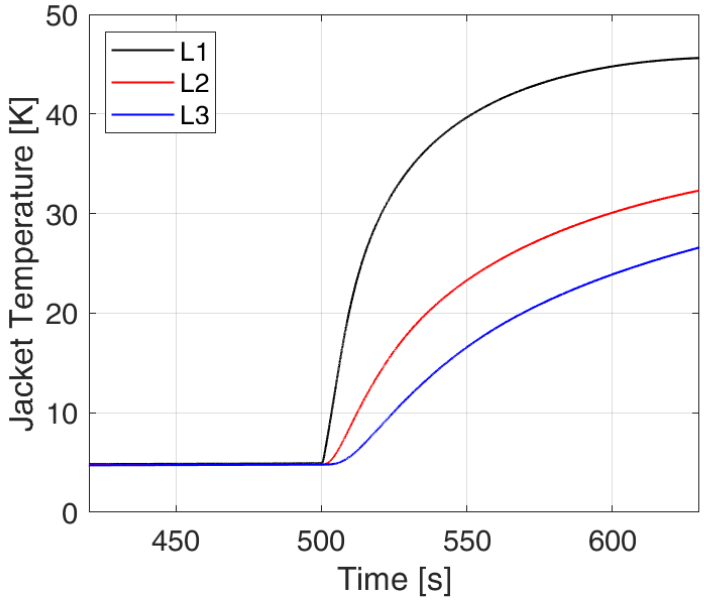

Figure 5.37: Evolution of the temperature of the jacket of layers L1, L2 and L3.

Chapter 6

Conclusions and perspective

The H4C code, devoted to the simulation of fast transients, such as quench, in High Temperature Superconducting (HTS) Cable-In-Conduit Conductors (CICCs), has been developed and applied to the most advanced conductor design and to the analysis of quench in an HTS magnet.

The development has been driven by the need for a more sophisticated modelling strategy in HTS than in Low Temperature Superconducting CICCs, which has been highlighted by both qualitative and quantitative assessments.

The qualitative assessment, based on dimensionless parameter analysis, comparing the typical LTS and HTS conductor time and space scales, showed that the underlying assumptions typical of LTS thermal-hydraulic (TH) and electric modelling tools are not suitable in case of fast transients in HTS conductors.

In order to find a suitable modelling strategy for HTS conductors, detailed electro-thermal models of the cross-sections of the two most successful HTS CICC designs, i.e., those based on slotted-core or on twisted-stacked tapes in round copper strands have been developed. These detailed models showed the need of a finer discretization of the cross-section than that typically adopted in LTS CICC TH modelling, i.e. the cross-section needs to be lumped in more than just two thermal and fluid regions and an electric model that takes into account transverse resistances is needed. Indeed, the different geometry and material properties of HTS with respect to LTS CICCs lead to a build up of temperature gradients and/or current non-uniformities in the conductor cross-section.

Following the results coming from the quantitative assessment, the 1D model developed in this thesis, named H4C, features the possibility to use an arbitrary number of thermal, fluid and electric 1D regions (along the axis of the conductor). The number of 1D regions is determined by the lumping strategy of the cross-section, which, in turn, depends on the conductor under analysis. This gives the flexibility needed for the modelling of HTS CICCs. Detailed models are however essential in order to find the best trade-off in the number of regions to be used in the model of a specific conductor.

In order to prove the reliability of the new conductor model, the standard verification and validation procedure has been followed. The code verification was successful and the preliminary validation performed on the quench experiments recently carried out in SULTAN showed encouraging results.

This allowed a wide range of applications of the new model. First, the quench analysis of the KIT CICC design proposal has been performed, comparing the results obtained simulating the quench using the LTS modelling approach against the new, more detailed approach. It was shown that the former was not able to catch the evolution of fundamental quantities, e.g., the voltage rise and the hotspot temperature, especially in case of localized heating. Then, the conductor model of the slotted-core concept proposed by ENEA was developed and the quench analysis of the HTS insert to be used in DTT has been performed, showing that the foreseen quench protection strategy, which is suitable for the LTS magnets, needs to be revised for the HTS insert. Also, a very detailed model of the sub-sized ENEA conductor sample has been developed, in order to support the design of the diagnostics foreseen in the upcoming quench tests in SULTAN. The model has been also used to understand the mechanism of current redistribution during the quench, in case it is induced by ramping up the coolant temperature, as planned in SULTAN.

Eventually, the conductor model has been upgraded in order to simulate an entire magnet, featuring both HTS and LTS layers, as foreseen in one option for the EU DEMO CS. In this case, the impact of a defect in one or more strands of the first (HTS) layer has been investigated. It was shown that, during normal operation, i.e., plasma burn, a smaller temperature margin is obtained as the damage becomes more severe, up to the point of inducing a quench. Thus, the quench simulation is carried out, showing that also in this case, for several seconds during the initial phase of quench propagation, large temperature differences and current non-uniformities are present in the conductor cross-section as a consequence of the localized defect. Also, it was shown that the quench of the first (HTS) layer can lead to a quench in the third layer at low current, which is in turn the first equipped with LTS.

In perspective, the validation of the conductor model will be improved and extended to the other conductors that have been tested, together with the conductors featuring different designs which will be tested soon.

The magnet model will be reliably used to assess the performance of the EU DEMO CS, as different (HTS) conductor concepts are being proposed for that magnet.

The magnet model will be also employed to explore different magnet protection strategies, as well as to investigate different scenarios in which a quench can initiate.

Appendix A

Code parallelization

The code parallelization was implemented through OpenMP [94]. This is just a first attempt to parallelize such calculation, thus the starting point was from a shared-memory approach.

The easiest starting point was to parallelize the calculation of transients in magnets. This is straightforward since the solution is computed independently for each hydraulic channel in each time step. This means that the solution of each time step in each channel can be performed by a given thread. In this way, ideally, the computational cost of the solution of a transient in a magnet featuring N hydraulic channels is the same of a single channel solved with the same strategy, e.g., same mesh and time step of those adopted for the simulation of an entire magnet.

The expectation is of course ideal, because there are anyway serial operations to be performed, such as the production of the output, which is proportionally larger for the simulation of a magnet than for a single conductor.

Figure A.1 shows the impact on the performance with and without the complete I/O of the code. The overhead introduced by the output to the disk is very large. Indeed, a clear assessment of the impact of the parallelization can be performed without the output. In this case, the speedup is even slightly better than ideal - most probably due to the oscillation on the CPU occupation during the simulation in serial. The evident impact of the parallelization almost disappears when the output is switched on. Therefore, it is fundamental to tune and reduce as much as possible the output production to gain the most from the parallelization.

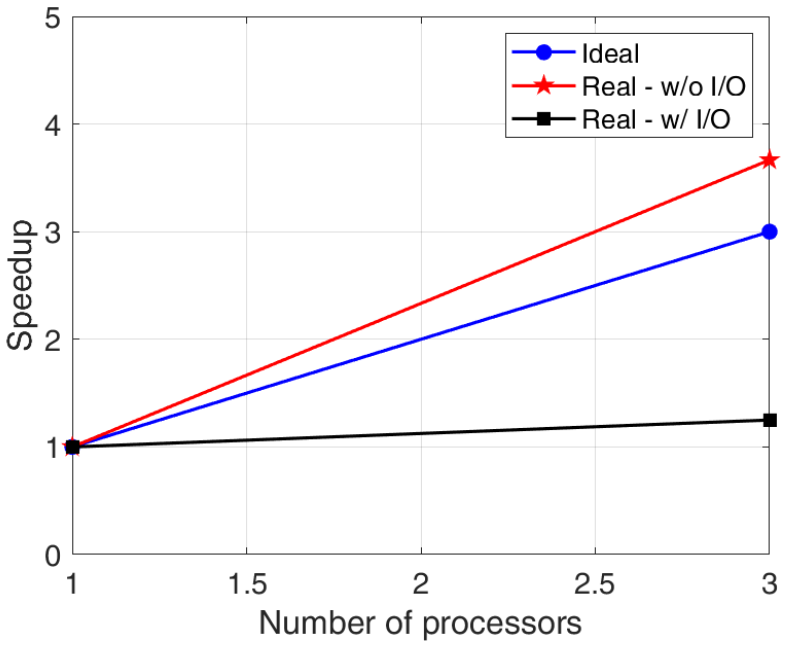

Figure A.1: Speedup of the simulations of the DEMO CS with and without I/O and varying the number of processors. The ideal speedup is also reported as reference.

Appendix B

Other activities carried out during the PhD

During my PhD I had the opportunity to contribute to other activities performed within the NEMO group (www.nemo.polito.it). Here I provide a brief summary of those activities.

B.1 CSM

I contributed to the predictive and interpretive thermal-hydraulic analyses, performed with the 4C code, of several transients (cooldown, current sharing temperature test, quench propagation following a current sharing temperature test, effect of AC losses) of interest for the tests of the ITER Central Solenoid Modules, see the co-authored papers on this topic [95], [96], [97].

B.2 DTT

I collaborated to the 4C analysis of several magnet sub-systems and transients of the Divertor Tokamak Test facility. Those analyses supported and are currently supporting the design of the DTT magnets. The papers I co-authored in this topic are the following: [98] and [99].

B.3 DEMO

I co-authored several works on the analysis of EU DEMO (LTS) magnets, using the 4C code, in both normal and off-normal operating conditions [100], [101], [102], [53].

B.4 CFD analyses

I contributed to the detailed 3D CFD analysis of high heat flux components [103], accidental scenarios in the vacuum vessel [104], possible optimization of the cooling of in-vessel components [105]. I also took part to benchmarks which are useful to strengthen the knowledge on CFD modelling [106].

B.5 HTS Current Leads

I contributed to the thermal-hydraulic modelling of HTS current leads and in particular to the validation of the computational tool employed at KIT for these devices [107], [108].

Bibliography

[1] V. Corato, T. Bagni, M. E. Biancolini, R. Bonifetto, P. Bruzzone, N. Bykovsky, D. Ciazynski, M. Coleman, A. della Corte, A. Dembkowska, A. Di Zenobio, M. Eisterer, W. H. Fietz, D. X. Fischer, E. Gaio, L. Giannini, F. Giorgetti, R. Heller, I. Ivashov, B. Lacroix, M. Lewandowska, A. Maistrello, L. Morici, L. Muzzi, A. Nijhuis, F. Nunio, A. Panin, X. Sarasola, L. Savoldi, K. Sedlak, B. Stepanov, G. Tomassetti, A. Torre, S. Turtù, D. Uglietti, R. Vallcorba, K. P. Weiss, R. Wesche, M. J. Wolf, K. Yagotintsev, L. Zani, and R. Zanino, "Progress in the design of the superconducting magnets for the EU DEMO," *Fusion Engineering and Design*, vol. 136, pp. 1597–1604, Nov. 2018, ISSN: 09203796. DOI: 10.1016/j.fusengdes.2018.05.065.

[2] R. Wesche, X. Sarasola, K. Sedlak, N. Bykovsky, B. Stepanov, D. Uglietti, and P. Bruzzone, "DEMO Central Solenoid Design Based on the Use of HTS Sections at Highest Magnetic Field," *IEEE Transactions on Applied Superconductivity*, vol. 28, no. 3, Apr. 2018, ISSN: 10518223. DOI: 10.1109/TASC.2018.2797955.

[3] B. N. Sorbom, J. Ball, T. R. Palmer, F. J. Mangiarotti, J. M. Sierchio, P. Bonoli, C. Kasten, D. A. Sutherland, H. S. Barnard, C. B. Haakonsen, J. Goh, C. Sung, and D. G. Whyte, "ARC: A compact, high-field, fusion nuclear science facility and demonstration power plant with demountable magnets," *Fusion Engineering and Design*, vol. 100, pp. 378–405, Nov. 2015, ISSN: 09203796. DOI: 10.1016/j.fusengdes.2015.07.008. arXiv: 1409.3540.

[4] W. Goldacker, A. Frank, R. Heller, S. I. Schlachter, B. Ringsdorf, K. P. Weiss, C. Schmidt, and S. Schuller, "ROEBEL Assembled Coated Conductors (RACC): Preparation, properties and progress," in *IEEE Transactions on Applied Superconductivity*, vol. 17, Jun. 2007, pp. 3398–3401. DOI: 10.1109/TASC.2007.899417.

[5] W. Goldacker, A. Frank, A. Kudymow, R. Heller, A. Kling, S. Terzieva, and C. Schmidt, "Status of high transport current ROEBEL assembled coated conductor cables," *Superconductor Science and Technology*, vol. 22, no. 3, p. 34 003, Jan. 2009, ISSN: 09532048. DOI: 10.1088/0953-2048/22/3/034003. [Online]. Available: https://iopscience.iop.org/article/10.1088/0953-

2048/22/3/034003%20https://iopscience.iop.org/article/10.1088/0953-2048/22/3/034003/meta.

[6] M. Takayasu, L. Chiesa, L. Bromberg, and J. V. Minervini, "Cabling Method for High Current Conductors Made of HTS Tapes," vol. 21, no. 3, pp. 2340–2344, 2011.

[7] D. Uglietti, R. Wesche, and P. Bruzzone, "Design and strand tests of a fusion cable composed of coated conductor tapes," *IEEE Transactions on Applied Superconductivity*, vol. 24, no. 3, 2014, ISSN: 10518223. DOI: 10.1109/TASC.2013.2281783.

[8] G. Celentano, G. De Marzi, F. Fabbri, L. Muzzi, G. Tomassetti, A. Anemona, S. Chiarelli, M. Seri, A. Bragagni, and A. Della Corte, "Design of an industrially feasible twisted-stack HTS cable-in-conduit conductor for fusion application," *IEEE Transactions on Applied Superconductivity*, vol. 24, no. 3, 2014, ISSN: 10518223. DOI: 10.1109/TASC.2013.2287910.

[9] M. J. Wolf, C. M. Bayer, W. H. Fietz, R. Heller, S. I. Schlachter, and K. P. Weiss, "Toward a High-Current Conductor Made of HTS CrossConductor Strands," *IEEE Transactions on Applied Superconductivity*, vol. 26, no. 4, Jun. 2016, ISSN: 10518223. DOI: 10.1109/TASC.2016.2525734.

[10] S. Ito, N. Yusa, N. Yanagi, H. Tamura, A. Sagara, and H. Hashizume, "Mechanical and Electrical Characteristics of a Bridge-Type Mechanical Lap Joint of HTS STARS Conductors," *IEEE Transactions on Applied Superconductivity*, vol. 26, no. 2, Mar. 2016, ISSN: 10518223. DOI: 10.1109/TASC.2016.2517197.

[11] Y. Wang, S. Baasansuren, C. Xue, and T. Hasegawa, "Development of a Quasi-Isotropic Strand Stacked by 2G Wires," *IEEE Transactions on Applied Superconductivity*, 2016, ISSN: 10518223. DOI: 10.1109/TASC.2016.2527042.

[12] T. Mulder, A. Dudarev, M. Mentink, H. Silva, D. Van Der Laan, M. Dhalle, and H. Ten Kate, "Design and Manufacturing of a 45 kA at 10 T REBCO-CORC Cable-in-Conduit Conductor for Large-Scale Magnets," *IEEE Transactions on Applied Superconductivity*, vol. 26, no. 4, Jun. 2016, ISSN: 10518223. DOI: 10.1109/TASC.2016.2527241.

[13] M. J. Wolf, W. H. Fietz, C. M. Bayer, S. I. Schlachter, R. Heller, and K. P. Weiss, "HTS CroCo: A stacked HTS conductor optimized for high currents and long-length production," *IEEE Transactions on Applied Superconductivity*, vol. 26, no. 2, pp. 2–7, 2016, ISSN: 10518223. DOI: 10.1109/TASC.2016.2521323.

[14] R. Zanino and L. Savoldi Richard, "A review of thermal-hydraulic issues in ITER cable-in-conduit conductors," *Cryogenics*, vol. 46, pp. 541–555, 7-8 Jul. 2006, ISSN: 00112275. DOI: 10.1016/j.cryogenics.2006.01.007.

[15] G. A. Levin, P. N. Barnes, J. P. Rodriguez, J. A. Connors, and J. S. Bulmer, "Stability and normal zone propagation speed in YBCO coated conductors with increased interfacial resistance," vol. 19, Jun. 2009, pp. 2504–2507. DOI: 10.1109/TASC.2009.2019604.

[16] V. Sokolovsky and V. Meerovich, "Normal zone propagation along superconducting films deposited on wide substrates," *Cryogenics*, vol. 48, pp. 397–405, 9-10 Sep. 2008, ISSN: 00112275. DOI: 10.1016/j.cryogenics.2008.03.020.

[17] W. K. Chan, P. J. Masson, C. A. Luongo, and J. Schwartz, "Influence of inter-layer contact resistances on quench propagation in YBa2Cu3Ox coated conductors," vol. 19, Jun. 2009, pp. 2490–2495. DOI: 10.1109/TASC.2009.2018514.

[18] M. Casali, M. Breschi, and P. L. Ribani, "Two-dimensional anisotropic model of YBCO coated conductors," *IEEE Transactions on Applied Superconductivity*, vol. 25, p. 6 600 112, 1 Feb. 2015, ISSN: 10518223. DOI: 10.1109/TASC.2014.2341180.

[19] C. Lacroix and F. Sirois, "Concept of a current flow diverter for accelerating the normal zone propagation velocity in 2G HTS coated conductors," *Superconductor Science and Technology*, vol. 27, no. 3, p. 035 003, Mar. 2014, ISSN: 09532048. DOI: 10.1088/0953-2048/27/3/035003. [Online]. Available: https://iopscience.iop.org/article/10.1088/0953-2048/27/3/035003%20https://iopscience.iop.org/article/10.1088/0953-2048/27/3/035003/meta.

[20] W. K. Chan, P. J. Masson, C. Luongo, and J. Schwartz, "Three-dimensional micrometer-scale modeling of quenching in high-aspect-ratio YBa2Cu3O7-delta; coated conductor tapes part I: Mdel development and validation," *IEEE Transactions on Applied Superconductivity*, vol. 20, pp. 2370–2380, 6 Dec. 2010, ISSN: 10518223. DOI: 10.1109/TASC.2010.2072956.

[21] L. Prigozhin and V. Sokolovsky, "Computing AC losses in stacks of high-temperature superconducting tapes," *Superconductor Science and Technology*, vol. 24, p. 075 012, 7 Jul. 2011, ISSN: 09532048. DOI: 10.1088/0953-2048/24/7/075012.

[22] V. M. Rodriguez-Zermeno, N. Mijatovic, C. Træholt, T. Zirngibl, E. Seiler, A. B. Abrahamsen, N. F. Pedersen, and M. P. Sørensen, "Towards faster FEM simulation of thin film superconductors: A multiscale approach," *IEEE Transactions on Applied Superconductivity*, vol. 21, pp. 3273–3276, 3 PART 3 Jun. 2011, ISSN: 10518223. DOI: 10.1109/TASC.2010.2091388.

[23] V. M. Zermeno, F. Grilli, and F. Sirois, "A full 3D time-dependent electromagnetic model for Roebel cables," *Superconductor Science and Technology*, vol. 26, p. 052 001, 5 May 2013, ISSN: 09532048. DOI: 10.1088/0953-2048/26/5/052001.

[24] W. Yuan, A. M. Campbell, and T. A. Coombs, "A model for calculating the AC losses of second-generation high temperature superconductor pancake coils," *Superconductor Science and Technology*, vol. 22, p. 075 028, 7 2009, ISSN: 09532048. DOI: 10.1088/0953-2048/22/7/075028.

[25] S. Hahn, Y. Kim, J. Ling, J. Voccio, D. K. Park, J. Bascunan, H. J. Shin, H. Lee, and Y. Iwasa, "No-insulation coil under time-varying condition: Magnetic coupling with external coil," *IEEE Transactions on Applied Superconductivity*, vol. 23, p. 4 601 705, 3 2013, ISSN: 10518223. DOI: 10.1109/TASC.2013.2240756.

[26] O. J. Kwon, K. L. Kim, Y. H. Choi, H. J. Shin, S. Hahn, Y. Iwasa, and H. G. Lee, "Effects of turn-to-turn compactness in the straight sections of HTS racetrack coils on thermal and electrical characteristics," *Superconductor Science and Technology*, vol. 26, p. 085 025, 8 Aug. 2013, ISSN: 09532048. DOI: 10.1088/0953-2048/26/8/085025.

[27] V. Zermeno, P. Krüger, M. Takayasu, and F. Grilli, "Modeling and simulation of termination resistances in superconducting cables," *Superconductor Science and Technology*, vol. 27, p. 124 013, 12 Dec. 2014, ISSN: 13616668. DOI: 10.1088/0953-2048/27/12/124013.

[28] W. K. Chan and J. Schwartz, "A hierarchical three-dimensional multiscale electro-magneto-thermal model of quenching in REBa 2Cu 3O 7?δ coated-conductor-based coils," *IEEE Transactions on Applied Superconductivity*, vol. 22, no. 5, 2012, ISSN: 10518223. DOI: 10.1109/TASC.2012.2198647.

[29] F. Liang, S. Venuturumilli, H. Zhang, M. Zhang, J. Kvitkovic, S. Pamidi, Y. Wang, and W. Yuan, "A finite element model for simulating second generation high temperature superconducting coils/stacks with large number of turns," *Journal of Applied Physics*, vol. 122, p. 043 903, 4 Jul. 2017, ISSN: 10897550. DOI: 10.1063/1.4995802.

[30] F. Grilli, R. Brambilla, F. Sirois, A. Stenvall, and S. Memiaghe, "Development of a three-dimensional finite-element model for high-temperature superconductors based on the H-formulation," vol. 53, Jan. 2013, pp. 142–147. DOI: 10.1016/j.cryogenics.2012.03.007.

[31] S. S. Fetisov, V. V. Zubko, S. Y. Zanegin, A. A. Nosov, and V. S. Vysotsky, "Numerical Simulation and Cold Test of a Compact 2G HTS Power Cable," *IEEE Transactions on Applied Superconductivity*, vol. 28, p. 5 400 905, 4 Jun. 2018, ISSN: 10518223. DOI: 10.1109/TASC.2018.2821708.

[32] F. Grilli, V. M. Zermeño, and M. Takayasu, "Numerical modeling of twisted stacked tape cables for magnet applications," *Physica C: Superconductivity and its Applications*, vol. 518, pp. 122–125, Mar. 2015, ISSN: 09214534. DOI: 10.1016/j.physc.2015.03.007.

[33] A. Stenvall, F. Grilli, and M. Lyly, "Current-penetration patterns in twisted superconductors in self-field," *IEEE Transactions on Applied Superconductivity*, vol. 23, p. 8 200 105, 3 2013, ISSN: 10518223. DOI: 10.1109/TASC.2012.2228733.

[34] M. Breschi, M. Casali, L. Cavallucci, G. D. Marzi, and G. Tomassetti, "Electrothermal analysis of a twisted stacked YBCO cable-in-conduit conductor," *IEEE Transactions on Applied Superconductivity*, vol. 25, p. 4 800 505, 3 Jun. 2015, ISSN: 10518223. DOI: 10.1109/TASC.2014.2361270.

[35] Y. Wang, M. Zhang, F. Grilli, Z. Zhu, and W. Yuan, "Study of the magnetization loss of CORC ® cables using a 3D T-A formulation," *Superconductor Science and Technology*, vol. 32, p. 025 003, 2 Feb. 2019, ISSN: 0953-2048. DOI: 10.1088/1361-6668/aaf011. [Online]. Available: https://iopscience.iop.org/article/10.1088/1361-6668/aaf011.

[36] T. Tsukamoto, T. Mifune, Y. Sogabe, Z. Jiang, T. Nakamura, and N. Amemiya, "Influence of geometrical configurations of HTS Roebel cables on their AC losses," *IEEE Transactions on Applied Superconductivity*, vol. 25, p. 4 802 005, 3 Jun. 2015, ISSN: 10518223. DOI: 10.1109/TASC.2014.2368056.

[37] M. Nii, N. Amemiya, and T. Nakamura, "Three-dimensional model for numerical electromagnetic field analyses of coated superconductors and its application to Roebel cables," *Superconductor Science and Technology*, vol. 25, p. 095 011, 9 Sep. 2012, ISSN: 09532048. DOI: 10.1088/0953-2048/25/9/095011.

[38] V. M. Zermeno, A. B. Abrahamsen, N. Mijatovic, B. B. Jensen, and M. P. Sørensen, "Calculation of alternating current losses in stacks and coils made of second generation high temperature superconducting tapes for large scale applications," *Journal of Applied Physics*, vol. 114, p. 173 901, 17 Nov. 2013, ISSN: 00218979. DOI: 10.1063/1.4827375.

[39] L. Quéval, V. M. Zermeño, and F. Grilli, "Numerical models for ac loss calculation in large-scale applications of HTS coated conductors," *Superconductor Science and Technology*, vol. 29, p. 024 007, 2 Jan. 2016, ISSN: 13616668. DOI: 10.1088/0953-2048/29/2/024007.

[40] L. Bottura, "Thermal, Hydraulic, and Electromagnetic Modeling of Superconducting Magnet Systems," *IEEE Transactions on Applied Superconductivity*, vol. 26, p. 7 437 426, 3 Apr. 2016, ISSN: 10518223. DOI: 10.1109/TASC.2016.2544253.

[41] Alphysica. (2019). "2019 Venecia Home," [Online]. Available: http://www.alphysica.com/venecia.php. (accessed: 01.06.2021).

[42] L. Bottura, C. Rosso, and M. Breschi, "A general model for thermal, hydraulic and electric analysis of superconducting cables," *Cryogenics*, 2000, ISSN: 00112275. DOI: 10.1016/s0011-2275(01)00019-4.

[43] L. Savoldi Richard, F. Casella, B. Fiori, and R. Zanino, "The 4C code for the cryogenic circuit conductor and coil modeling in ITER," *Cryogenics*, vol. 50, pp. 167–176, 3 Mar. 2010, ISSN: 00112275. DOI: 10.1016/j.cryogenics.2009.07.008.

[44] N. Bagrets, W. Goldacker, A. Jung, and K. Weiss, "Thermal Properties of ReBCO Copper Stabilized Superconducting Tapes," vol. 23, no. 3, pp. 2012–2014, 2013.

[45] A. Zappatore, W. H. Fietz, R. Heller, L. Savoldi, M. J. Wolf, and R. Zanino, "A critical assessment of thermal-hydraulic modeling of HTS twisted-stacked-tape cable conductors for fusion applications," *Superconductor Science and Technology*, vol. 32, no. 8, pp. 1–15, 2019, ISSN: 13616668. DOI: 10.1088/1361-6668/ab20a9.

[46] A. Zappatore, R. Heller, L. Savoldi, M. J. Wolf, and R. Zanino, "A new model for the analysis of quench in HTS cable-in-conduit conductors based on the twisted-stacked-tape cable concept for fusion applications," *Superconductor Science and Technology*, vol. 33, no. 6, 2020, ISSN: 13616668. DOI: 10.1088/1361-6668/ab895b.

[47] A. Zappatore and R. Bonifetto. (2021). "Analysis of experimental results – PoliTo, PoliTo, Feb. 2021," [Online]. Available: https://idm.euro-fusion.org/?uid=2PFBEK.

[48] A. Zappatore, A. Augieri, R. Bonifetto, G. Celentano, L. Savoldi, A. Vannozzi, and R. Zanino, "Modeling Quench Propagation in the ENEA HTS Cable-In-Conduit Conductor," *IEEE Transactions on Applied Superconductivity*, vol. 30, no. 8, Dec. 2020, ISSN: 15582515. DOI: 10.1109/TASC.2020.3001035.

[49] A. Zappatore, A. Augieri, R. Bonifetto, G. Celentano, M. Marchetti, A. Vannozzi, and R. Zanino, "Development of the H4C Model of Quench Propagation in the ENEA HTS Cable-In-Conduit Conductor," *IEEE Transactions on Applied Superconductivity*, vol. 31, 5 Aug. 2021, ISSN: 15582515. DOI: 10.1109/TASC.2021.3059608.

[50] A. Zappatore, R. Bonifetto, X. Sarasola, and R. Zanino, "Thermal-hydraulic analysis of quench propagation in the hybrid (HTS-LTS) Central Solenoid for the EU DEMO fusion reactor," presented at Symposium on Fusion Technology, Virtual edition, 2020.

[51] M. Lewandowska, A. Dembkowska, R. Heller, and M. Wolf, "Thermal-hydraulic analysis of an HTS DEMO TF coil," *Cryogenics*, 2018, ISSN: 00112275. DOI: 10.1016/j.cryogenics.2018.10.014.

[52] G. Federici, W. Biel, M. R. Gilbert, R. Kemp, N. Taylor, and R. Wenninger, "European DEMO design strategy and consequences for materials," *Nuclear Fusion*, vol. 57, p. 092 002, 9 Jun. 2017, ISSN: 17414326. DOI: 10.1088/1741-4326/57/9/092002.

[53] A. Zappatore, R. Bonifetto, P. Bruzzone, V. Corato, A. Di Zenobio, L. Savoldi, K. Sedlak, S. Turtu, and R. Zanino, "Performance Analysis of the NbTi PF Coils for the EU DEMO Fusion Reactor," *IEEE Transactions on Applied Superconductivity*, vol. 28, 4 Jun. 2018, ISSN: 10518223. DOI: 10.1109/TASC.2018.2793462.

[54] X. Wang, A. R. Caruso, M. Breschi, G. Zhang, U. P. Trociewitz, H. W. Weijers, and J. Schwartz, "Normal zone initiation and propagation in Y-Ba-Cu-O coated conductors with Cu stabilizer," vol. 15, Jun. 2005, pp. 2586–2589. DOI: 10.1109/TASC.2005.847661.

[55] H. Barrow, A. K. Hassan, and C. Avgerinos, "Peripheral temperature variation in the wall of a noncircular duct - An experimental investigation," *International Journal of Heat and Mass Transfer*, vol. 27, pp. 1031–1037, 7 1984, ISSN: 00179310. DOI: 10.1016/0017-9310(84)90119-4.

[56] N. I. of Standards and T. (U.S.), *NIST Monograph*, ser. NIST Monograph No. 177. U.S. Department of Commerce, National Institute of Standards and Technology, 1992. [Online]. Available: https://books.google.it/books?id=TxRWAAAAYAAJ.

[57] Siemens Digital Industries Software, *Simcenter STAR-CCM+*, version 2019.1.1 (14.02.012-R8), 2019. [Online]. Available: https://www.plm.automation.siemens.com/global/en/products/simcenter/STAR-CCM.html.

[58] R. Heller, P. V. Gade, W. H. Fietz, T. Vogel, and K. P. Weiss, "Conceptual Design Improvement of a Toroidal Field Coil for EU DEMO Using High-Temperature Superconductors," *IEEE Transactions on Applied Superconductivity*, vol. 26, no. 4, 2016, ISSN: 10518223. DOI: 10.1109/TASC.2016.2520662.

[59] S. K, *Common operating values for DEMO magnets design for 2016*, 2016.

[60] T. L. Bergman, A. S. Lavine, F. P. Incropera, and D. P. Dewitt, *Fundamentals of Heat and Mass Transfer. 7th Edition*. 2011, ISBN: 978-0470-50197-9.

[61] R. Zanino, R. Bonifetto, and L. Savoldi Richard, "Analysis of quench propagation in the ITER poloidal field conductor insert (PFCI)," vol. 20, Jun. 2010, pp. 491–494. DOI: 10.1109/TASC.2010.2041547.

[62] COMSOL AB, *COMSOL Multiphysics®*, version 5.4, 2019. [Online]. Available: www.comsol.com.

[63] M. Breschi, P. L. Ribani, X. Wang, and J. Schwartz, "Theoretical explanation of the non-equipotential quench behaviour in Y-Ba-Cu-O coated conductors," *Superconductor Science and Technology*, vol. 20, pp. L9–11, 4 Apr. 2007, ISSN: 09532048. DOI: 10.1088/0953-2048/20/4/L01.

[64] S. Inc. (2021). "Architecture of a standard SuperPower 2G HTS tape," [Online]. Available: https://superpower-inc.com/Technology.aspx.

[65] R. Zanino, S. De Palo, and L. Bottura, "A two-fluid code for the thermohydraulic transient analysis of CICC superconducting magnets," *Journal of Fusion Energy*, vol. 14, no. 1, pp. 25–40, Mar. 1995, ISSN: 01640313. DOI: 10.1007/BF02214031. [Online]. Available: https://link.springer.com/article/10.1007/BF02214031.

[66] M. Ciotti, A. Nijhuis, P. L. Ribani, L. Savoldi Richard, and R. Zanino, "THELMA code electromagnetic model of ITER superconducting cables and application to the ENEA stability experiment," *Superconductor Science and Technology*, vol. 19, no. 10, pp. 987–997, Oct. 2006, ISSN: 09532048. DOI: 10.1088/0953-2048/19/10/001. [Online]. Available: https://iopscience.iop.org/article/10.1088/0953-2048/19/10/001%20https://iopscience.iop.org/article/10.1088/0953-2048/19/10/001/meta.

[67] L. Savoldi and R. Zanino, "M & M: Multi-conductor Mithrandir code for the simulation of thermal-hydraulic transients in superconducting magnets," *Cryogenics*, vol. 40, no. 3, pp. 179–189, Mar. 2000, ISSN: 00112275. DOI: 10.1016/S0011-2275(00)00027-8.

[68] W. L. Oberkampf and C. J. Roy, *Verification and validation in scientific computing*. 2011, ISBN: 9780511760396. DOI: 10.1017/CBO9780511760396.

[69] K. Sedlak and O. Dicuonzo. (2021). "Report on the HTS quench sample manufacturing, SPC, 2020," [Online]. Available: https://idm.euro-fusion.org/?uid=2NMLMB.

[70] R. Zanino, R. Bonifetto, A. Brighenti, T. Isono, H. Ozeki, and L. Savoldi, "Prediction, experimental results and analysis of the ITER TF insert coil quench propagation tests, using the 4C code," *Superconductor Science and Technology*, vol. 31, no. 3, 2018, ISSN: 13616668. DOI: 10.1088/1361-6668/aa9e6c.

[71] R. Bonifetto, T. Isono, N. Martovetsky, L. Savoldi, and R. Zanino, "Analysis of quench propagation in the ITER central solenoid insert (CSI) Coil," *IEEE Transactions on Applied Superconductivity*, vol. 27, 4 Jun. 2017, ISSN: 10518223. DOI: 10.1109/TASC.2016.2634598.

[72] B. R. Munson, T. H. Okiishi, W. W. Huebsch, Rothmayer, and A. P, *Fundamentals of Fluid Mechanics Seventh Edition*. 2013, ISBN: 9781118116135.

[73] R. Kang, D. Uglietti, R. Wesche, K. Sedlak, P. Bruzzone, and Y. Song, "Quench Simulation of REBCO Cable-in-Conduit Conductor With Twisted Stacked-Tape Cable," *IEEE Transactions on Applied Superconductivity*, vol. 30, no. 1, pp. 1–7, Jan. 2020, ISSN: 1051-8223. DOI: 10.1109/TASC.2019.2926258. [Online]. Available: https://ieeexplore.ieee.org/document/8753588/.

[74] ENEA, "DTT: Divertor Tokamak Test Facility Interim Design Report," 2019.

[75] L. Cavallucci, M. Breschi, P. L. Ribani, and Y. Yang, "Electrothermal Modeling of Quench in REBCO Roebel Cables," vol. 28, no. 4, pp. 18–22, 2018.

[76] L. Savoldi, A. Augieri, R. Bonifetto, P. Bruzzone, S. Carli, G. Celentano, A. Della Corte, G. De Marzi, L. Muzzi, V. Piras, and R. Zanino, "Thermal-Hydraulic Modeling of a Novel HTS CICC for Nuclear Fusion Applications," *IEEE Transactions on Applied Superconductivity*, vol. 26, no. 3, pp. 1–7, 2016, ISSN: 10518223. DOI: 10.1109/TASC.2016.2528541.

[77] J. H. Ferziger, M. Peric, and A. Leonard, " Computational Methods for Fluid Dynamics," *Physics Today*, 1997, ISSN: 0031-9228. DOI: 10.1063/1.881751.

[78] Y. Cengel, R. Turner, and R. Smith, "Fundamentals of Thermal-Fluid Sciences," *Applied Mechanics Reviews*, 2001, ISSN: 00036900. DOI: 10.1115/1.1421126.

[79] R. Zanino, S. Giors, and R. Mondino, "CFD modeling of ITER cable-in-conduit superconductors. Part I: Friction in the central channel," in *AIP Conference Proceedings*, 2006, ISBN: 0735403171. DOI: 10.1063/1.2202514.

[80] P. Bruzzone, B. Stepanov, R. Wesche, M. Bagnasco, F. Cau, R. Herzog, M. Calvi, M. Vogel, M. Jenni, M. Holenstein, and H. Rajainmaki, "Status report of the SULTAN test facility," vol. 20, Jun. 2010, pp. 455–457. DOI: 10.1109/TASC.2010.2042583.

[81] A. Zappatore, R. Bonifetto, P. Bruzzone, V. Corato, A. D. Zenobio, L. Savoldi, K. Sedlak, S. Turtu, and R. Zanino, "Performance Analysis of the NbTi PF Coils for the EU DEMO Fusion Reactor," *IEEE Transactions on Applied Superconductivity*, vol. 28, p. 4 901 005, 4 Jun. 2018, ISSN: 10518223. DOI: 10.1109/TASC.2018.2793462.

[82] W. H. Fietz, N. Bagrets, R. Heller, L. Savoldi, K. P. Weiss, M. J. Wolf, R. Zanino, and A. Zappatore, "Determination of the thermal resistance between pressed copper-copper and copper-stainless steel interfaces for high current HTS CICC," presented at Magnet Technology conference, Vancouver, Canada, 2019.

[83] Z. Piątek, B. Baron, T. Szczegielniak, D. Kusiak, and A. Pasierbek, "Mutual inductance of two thin tapes with perpendicular widths," *Przegląd Elektrotechniczny*, 2013.

[84] L. Savoldi, R. Bonifetto, R. Zanino, and L. Muzzi, "Analyses of Low- and High-Margin Quench Propagation in the European DEMO TF Coil Winding Pack," *IEEE Transactions on Plasma Science*, vol. 44, pp. 1564–1570, 9 Sep. 2016, ISSN: 00933813. DOI: 10.1109/TPS.2016.2542920.

[85] R. Brambilla, F. Grilli, and L. Martini, "Development of an edge-element model for AC loss computation of high-temperature superconductors," *Superconductor Science and Technology*, vol. 20, no. 1, pp. 16–24, 2007, ISSN: 09532048. DOI: 10.1088/0953-2048/20/1/004.

[86] F. R. Menter, "Two-equation eddy-viscosity turbulence models for engineering applications," *AIAA Journal*, 1994, ISSN: 00011452. DOI: 10.2514/3.12149.

[87] Y. Iwasa, *Case studies in superconducting magnets: Design and operational issues: Second edition*. 2009, ISBN: 9780387097992. DOI: 10.1007/b112047.

[88] M. J. Wolf, R. Heller, W. H. Fietz, and K. P. Weiss, "Design and analysis of HTS subsize-conductors for quench investigations towards future HTS fusion magnets," *Cryogenics*, 2019, ISSN: 00112275. DOI: 10.1016/j.cryogenics.2019.102980.

[89] N. Bykovskiy, "HTS high current cable for fusion application," Ph.D. dissertation, École Polytechnique Fédérale de Lausanne, 2017.

[90] S. J. Sackett and S. J. -Sackett, "Calculation of electromagnetic fields and forces in coil systems of arbitrary geometry," Tech. Rep., Nov. 1975. [Online]. Available: https://digital.library.unt.edu/ark:/67531/metadc868510/.

[91] X. Sarasola, R. Wesche, I. Ivashov, K. Sedlak, D. Uglietti, and P. Bruzzone, "Progress in the Design of a Hybrid HTS-Nb_3Sn-NbTi Central Solenoid for the EU DEMO," *IEEE Transactions on Applied Superconductivity*, vol. 30, pp. 2–6, 4 2020, ISSN: 15582515. DOI: 10.1109/TASC.2020.2965066.

[92] X. Sarasola, private communication, Aug. 2020.

[93] A. Dembkowska, M. Lewandowska, and X. Sarasola, "Thermal-Hydraulic Analysis of the DEMO CS Coil," *IEEE Transactions on Applied Superconductivity*, vol. 28, 4 Jun. 2018, ISSN: 10518223. DOI: 10.1109/TASC.2018.2809425.

[94] OpenMP Architecture Review Board, *OpenMP Application Program Interface Version 3.0*, May 2008. [Online]. Available: http://www.openmp.org/mp-documents/spec30.pdf.

[95] N. Martovetsky, K. Freudenberg, D. Hatfield, G. Rossano, W. Reiersen, K. Khumthong, A. Langhorn, N. Norausky, E. Ortiz, Z. Piec, K. Schaubel, J. Sheeron, J. Smith, R. Bonifetto, R. Zanino, A. Zappatore, T. Schild, P. Libeyre, D. Bessette, F. Gauthier, C. Jong, Y. Ilyin, L. Myatt, K. Cochran, M. Breschi, and W. Feindt, "First ITER CS module test results," *Fusion Engineering and Design*, vol. 164, Mar. 2021, ISSN: 09203796. DOI: 10.1016/j.fusengdes.2020.112169.

[96] M. Breschi, L. Cavallucci, P. L. Ribani, R. Bonifetto, A. Zappatore, R. Zanino, F. Gauthier, P. Bauer, and N. Martovetsky, "AC Losses in the First ITER CS Module Tests: Experimental Results and Comparison to Analytical Models," *IEEE Transactions on Applied Superconductivity*, vol. 31, 5 Aug. 2021, ISSN: 15582515. DOI: 10.1109/TASC.2021.3061950.

[97] F. Gauthier, T. Schild, N. N. Martovetsky, K. Khumthong, K. M. Schaubel, J. Sheeron, A. R. Langhorn, R. Bonifetto, R. Zanino, and A. Zappatore, "Thermal Hydraulic Behavior of the First ITER CS Module," *IEEE Transactions on Applied Superconductivity*, vol. 31, 5 Aug. 2021, ISSN: 15582515. DOI: 10.1109/TASC.2021.3053505.

[98] A. Di Zenobio, R. Albanese, A. Anemona, M. E. Biancolini, R. Bonifetto, C. Brutti, V. Corato, F. Crisanti, A. della Corte, G. De Marzi, C. Fiamozzi Zignani, F. Giorgetti, G. Messina, L. Muzzi, L. Savoldi, G. Tomassetti, S. Turtù, F. Villone, and A. Zappatore, "DTT device: Conceptual design of the superconducting magnet system," *Fusion Engineering and Design*, vol. 122, pp. 299–312, Nov. 2017, ISSN: 09203796. DOI: 10.1016/j.fusengdes.2017.03.102.

[99] R. Bonifetto, A. D. Zenobio, L. Muzzi, S. Turtù, R. Zanino, and A. Zappatore, "Thermal-Hydraulic Analysis of the DTT Toroidal Field Magnets in DC Operation," *IEEE Transactions on Applied Superconductivity*, vol. 30, 4 Jun. 2020, ISSN: 15582515. DOI: 10.1109/TASC.2020.2964517.

[100] R. Bonifetto, P. Bruzzone, V. Corato, L. Muzzi, L. Savoldi, B. Stepanov, R. Zanino, and A. Zappatore, "Thermal-Hydraulic Test and Analysis of the ENEA TF Conductor Sample for the EU DEMO Fusion Reactor," *IEEE Transactions on Applied Superconductivity*, vol. 28, 4 Jun. 2018, ISSN: 10518223. DOI: 10.1109/TASC.2018.2821367.

[101] K. Sedlak, V. A. Anvar, N. Bagrets, M. E. Biancolini, R. Bonifetto, F. Bonne, D. Boso, A. Brighenti, P. Bruzzone, G. Celentano, A. Chiappa, V. D'Auria, M. Dan, P. Decool, A. Della Corte, A. Dembkowska, O. Dicuonzo, I. Duran, M. Eisterer, A. Ferro, C. Fiamozzi Zignani, W. H. Fietz, C. Frittitta, E. Gaio, L. Giannini, F. Giorgetti, F. Gömöry, X. Granados, R. Guarino, R. Heller, C. Hoa, I. Ivashov, G. Jiolat, M. Jirsa, B. Jose, R. Kembleton, M. Kumar, B. Lacroix, Q. Le Coz, M. Lewandowska, A. Maistrello, N. Misiara, L. Morici, L. Muzzi, S. Nicollet, A. Nijhuis, F. Nunio, C. Portafaix, G. Romanelli, X. Sarasola, L. Savoldi, B. Stepanov, I. Tiseanu, G. Tomassetti, A. Torre, S. Turtù, D. Uglietti, R. Vallcorba, L. Viererbl, M. Vojenciak, C. Vorpahl, K. P. Weiss, R. Wesche, M. J. Wolf, L. Zani, R. Zanino, A. Zappatore, and V. Corato, "Advance in the conceptual design of the European DEMO magnet system," *Superconductor Science and Technology*, vol. 33, no. 4, 2020, ISSN: 13616668. DOI: 10.1088/1361-6668/ab75a9.

[102] L. Savoldi, R. Bonifetto, A. Brighenti, V. Corato, L. Muzzi, S. Turtu, R. Zanino, and A. Zappatore, "Quench propagation in a TF coil of the EU DEMO," *Fusion Science and Technology*, vol. 72, pp. 439–448, 3 Oct. 2017, ISSN: 15361055. DOI: 10.1080/15361055.2017.1333866.

[103] A. Bertinetti, F. Albajar, F. Cau, A. Leggieri, F. Legrand, E. Perial, G. Ritz, L. Savoldi, R. Zanino, and A. Zappatore, "Design, Test and Analysis of a Gyrotron Cavity Mock-Up Cooled Using Mini Channels," *IEEE Transactions on Plasma Science*, vol. 46, pp. 2207–2215, 6 Jun. 2018, ISSN: 00933813. DOI: 10.1109/TPS.2018.2829600.

[104] A. Zappatore, A. Froio, G. A. Spagnuolo, and R. Zanino, "3D transient CFD simulation of an in-vessel loss-of-coolant accident in the EU DEMO fusion reactor,"

Nuclear Fusion, vol. 60, 12 Dec. 2020, ISSN: 17414326. DOI: 10.1088/1741-4326/abac6b.

[105] A. Zappatore, A. Froio, G. A. Spagnuolo, and R. Zanino, "CFD analysis of natural convection cooling of the in-vessel components during a shutdown of the EU DEMO fusion reactor," *Fusion Engineering and Design*, vol. 165, Apr. 2021, ISSN: 09203796. DOI: 10.1016/j.fusengdes.2021.112252.

[106] L. Eça, G. Vaz, M. Hoekstra, S. Pal, E. Muller, D. Pelletier, A. Bertinetti, R. Difonzo, L. Savoldi, R. Zanino, A. Zappatore, Y. Chen, K. J. Maki, H. Ye, J. Drofelnik, B. Moss, and A. D. Ronch, "Overview of the 2018 Workshop on Iterative Errors in Unsteady Flow Simulations," *Journal of Verification, Validation and Uncertainty Quantification*, vol. 5, 2 Jun. 2020, ISSN: 2377-2158. DOI: 10.1115/1.4047922.

[107] R. Heller, P. Bauer, L. Savoldi, R. Zanino, and A. Zappatore, "Predictive 1-D thermal-hydraulic analysis of the prototype HTS current leads for the ITER correction coils," *Cryogenics*, vol. 80, pp. 325–332, Dec. 2016, ISSN: 00112275. DOI: 10.1016/j.cryogenics.2016.05.002.

[108] A. Zappatore, R. Heller, L. Savoldi, and R. Zanino, "Assessment of the performance of a 20 kA REBCO current lead," *Cryogenics*, vol. 95, pp. 95–101, Oct. 2018, ISSN: 00112275. DOI: 10.1016/j.cryogenics.2018.09.003.

Candidate's papers

[45] A. Zappatore, W. H. Fietz, R. Heller, L. Savoldi, M. J. Wolf, and R. Zanino, "A critical assessment of thermal-hydraulic modeling of HTS twisted-stacked-tape cable conductors for fusion applications," *Superconductor Science and Technology*, vol. 32, no. 8, pp. 1–15, 2019, ISSN: 13616668. DOI: 10.1088/1361-6668/ab20a9.

[46] A. Zappatore, R. Heller, L. Savoldi, M. J. Wolf, and R. Zanino, "A new model for the analysis of quench in HTS cable-in-conduit conductors based on the twisted-stacked-tape cable concept for fusion applications," *Superconductor Science and Technology*, vol. 33, no. 6, 2020, ISSN: 13616668. DOI: 10.1088/1361-6668/ab895b.

[47] A. Zappatore and R. Bonifetto. (2021). "Analysis of experimental results – PoliTo, PoliTo, Feb. 2021," [Online]. Available: https://idm.euro-fusion.org/?uid=2PFBEK.

[48] A. Zappatore, A. Augieri, R. Bonifetto, G. Celentano, L. Savoldi, A. Vannozzi, and R. Zanino, "Modeling Quench Propagation in the ENEA HTS Cable-In-Conduit Conductor," *IEEE Transactions on Applied Superconductivity*, vol. 30, no. 8, Dec. 2020, ISSN: 15582515. DOI: 10.1109/TASC.2020.3001035.

[49] A. Zappatore, A. Augieri, R. Bonifetto, G. Celentano, M. Marchetti, A. Vannozzi, and R. Zanino, "Development of the H4C Model of Quench Propagation in the ENEA HTS Cable-In-Conduit Conductor," *IEEE Transactions on Applied Superconductivity*, vol. 31, 5 Aug. 2021, ISSN: 15582515. DOI: 10.1109/TASC.2021.3059608.

[50] A. Zappatore, R. Bonifetto, X. Sarasola, and R. Zanino, "Thermal-hydraulic analysis of quench propagation in the hybrid (HTS-LTS) Central Solenoid for the EU DEMO fusion reactor," presented at Symposium on Fusion Technology, Virtual edition, 2020.

[53] A. Zappatore, R. Bonifetto, P. Bruzzone, V. Corato, A. Di Zenobio, L. Savoldi, K. Sedlak, S. Turtu, and R. Zanino, "Performance Analysis of the NbTi PF Coils for the EU DEMO Fusion Reactor," *IEEE Transactions on Applied Superconductivity*, vol. 28, 4 Jun. 2018, ISSN: 10518223. DOI: 10.1109/TASC.2018.2793462.

[81] A. Zappatore, R. Bonifetto, P. Bruzzone, V. Corato, A. D. Zenobio, L. Savoldi, K. Sedlak, S. Turtu, and R. Zanino, "Performance Analysis of the NbTi PF Coils for the EU DEMO Fusion Reactor," *IEEE Transactions on Applied Superconductivity*, vol. 28, p. 4 901 005, 4 Jun. 2018, ISSN: 10518223. DOI: 10.1109/TASC.2018.2793462.

[82] W. H. Fietz, N. Bagrets, R. Heller, L. Savoldi, K. P. Weiss, M. J. Wolf, R. Zanino, and A. Zappatore, "Determination of the thermal resistance between pressed copper-copper and copper-stainless steel interfaces for high current HTS CICC," presented at Magnet Technology conference, Vancouver, Canada, 2019.

[95] N. Martovetsky, K. Freudenberg, D. Hatfield, G. Rossano, W. Reiersen, K. Khumthong, A. Langhorn, N. Norausky, E. Ortiz, Z. Piec, K. Schaubel, J. Sheeron, J. Smith, R. Bonifetto, R. Zanino, A. Zappatore, T. Schild, P. Libeyre, D. Bessette, F. Gauthier, C. Jong, Y. Ilyin, L. Myatt, K. Cochran, M. Breschi, and W. Feindt, "First ITER CS module test results," *Fusion Engineering and Design*, vol. 164, Mar. 2021, ISSN: 09203796. DOI: 10.1016/j.fusengdes.2020.112169.

[96] M. Breschi, L. Cavallucci, P. L. Ribani, R. Bonifetto, A. Zappatore, R. Zanino, F. Gauthier, P. Bauer, and N. Martovetsky, "AC Losses in the First ITER CS Module Tests: Experimental Results and Comparison to Analytical Models," *IEEE Transactions on Applied Superconductivity*, vol. 31, 5 Aug. 2021, ISSN: 15582515. DOI: 10.1109/TASC.2021.3061950.

[97] F. Gauthier, T. Schild, N. N. Martovetsky, K. Khumthong, K. M. Schaubel, J. Sheeron, A. R. Langhorn, R. Bonifetto, R. Zanino, and A. Zappatore, "Thermal Hydraulic Behavior of the First ITER CS Module," *IEEE Transactions on Applied Superconductivity*, vol. 31, 5 Aug. 2021, ISSN: 15582515. DOI: 10.1109/TASC.2021.3053505.

[98] A. Di Zenobio, R. Albanese, A. Anemona, M. E. Biancolini, R. Bonifetto, C. Brutti, V. Corato, F. Crisanti, A. della Corte, G. De Marzi, C. Fiamozzi Zignani, F. Giorgetti, G. Messina, L. Muzzi, L. Savoldi, G. Tomassetti, S. Turtù, F. Villone, and A. Zappatore, "DTT device: Conceptual design of the superconducting magnet system," *Fusion Engineering and Design*, vol. 122, pp. 299–312, Nov. 2017, ISSN: 09203796. DOI: 10.1016/j.fusengdes.2017.03.102.

[99] R. Bonifetto, A. D. Zenobio, L. Muzzi, S. Turtù, R. Zanino, and A. Zappatore, "Thermal-Hydraulic Analysis of the DTT Toroidal Field Magnets in DC Operation," *IEEE Transactions on Applied Superconductivity*, vol. 30, 4 Jun. 2020, ISSN: 15582515. DOI: 10.1109/TASC.2020.2964517.

[100] R. Bonifetto, P. Bruzzone, V. Corato, L. Muzzi, L. Savoldi, B. Stepanov, R. Zanino, and A. Zappatore, "Thermal-Hydraulic Test and Analysis of the ENEA TF Conductor Sample for the EU DEMO Fusion Reactor," *IEEE Transactions on Applied Superconductivity*, vol. 28, 4 Jun. 2018, ISSN: 10518223. DOI: 10.1109/TASC.2018.2821367.

[102] L. Savoldi, R. Bonifetto, A. Brighenti, V. Corato, L. Muzzi, S. Turtu, R. Zanino, and A. Zappatore, "Quench propagation in a TF coil of the EU DEMO," *Fusion Science and Technology*, vol. 72, pp. 439–448, 3 Oct. 2017, ISSN: 15361055. DOI: 10.1080/15361055.2017.1333866.

[103] A. Bertinetti, F. Albajar, F. Cau, A. Leggieri, F. Legrand, E. Perial, G. Ritz, L. Savoldi, R. Zanino, and A. Zappatore, "Design, Test and Analysis of a Gyrotron Cavity Mock-Up Cooled Using Mini Channels," *IEEE Transactions on Plasma Science*, vol. 46, pp. 2207–2215, 6 Jun. 2018, ISSN: 00933813. DOI: 10.1109/TPS.2018.2829600.

[104] A. Zappatore, A. Froio, G. A. Spagnuolo, and R. Zanino, "3D transient CFD simulation of an in-vessel loss-of-coolant accident in the EU DEMO fusion reactor," *Nuclear Fusion*, vol. 60, 12 Dec. 2020, ISSN: 17414326. DOI: 10.1088/1741-4326/abac6b.

[105] A. Zappatore, A. Froio, G. A. Spagnuolo, and R. Zanino, "CFD analysis of natural convection cooling of the in-vessel components during a shutdown of the EU DEMO fusion reactor," *Fusion Engineering and Design*, vol. 165, Apr. 2021, ISSN: 09203796. DOI: 10.1016/j.fusengdes.2021.112252.

[106] L. Eça, G. Vaz, M. Hoekstra, S. Pal, E. Muller, D. Pelletier, A. Bertinetti, R. Difonzo, L. Savoldi, R. Zanino, A. Zappatore, Y. Chen, K. J. Maki, H. Ye, J. Drofelnik, B. Moss, and A. D. Ronch, "Overview of the 2018 Workshop on Iterative Errors in Unsteady Flow Simulations," *Journal of Verification, Validation and Uncertainty Quantification*, vol. 5, 2 Jun. 2020, ISSN: 2377-2158. DOI: 10.1115/1.4047922.

[107] R. Heller, P. Bauer, L. Savoldi, R. Zanino, and A. Zappatore, "Predictive 1-D thermal-hydraulic analysis of the prototype HTS current leads for the ITER correction coils," *Cryogenics*, vol. 80, pp. 325–332, Dec. 2016, ISSN: 00112275. DOI: 10.1016/j.cryogenics.2016.05.002.

[108] A. Zappatore, R. Heller, L. Savoldi, and R. Zanino, "Assessment of the performance of a 20 kA REBCO current lead," *Cryogenics*, vol. 95, pp. 95–101, Oct. 2018, ISSN: 00112275. DOI: 10.1016/j.cryogenics.2018.09.003.

This Ph.D. thesis has been typeset by means of the TEX-system facilities. The typesetting engine was LuaLATEX. The document class was `toptesi`, by Claudio Beccari, with option `tipotesi=scudo`. This class is available in every up-to-date and complete TEX-system installation.